Francisco Miguel Bastos Pereira

Computational Fluid Dynamics for Synthetic Data Generation

A Case Study on the Propulsion System of the SABUVIS II

Dissertation submitted in partial fulfillment of the requirements for the Master's degree on Marine Military Sciences, specialisation on Naval Engineering, Field of Mechanics

Orientation of: PROF CAT José Barata
Co-orientation of: PROF AUX Ricardo Moura

Alfeite
2025

ESCOLA NAVAL

Francisco Miguel Bastos Pereira

Computational Fluid Dynamics for Synthetic Data Generation
A Case Study on the Propulsion System of the SABUVIS II

Dissertation submitted in partial fulfillment of the requirements for the Master's degree on Marine Military Sciences, specialisation on Naval Engineering, Field of Mechanics

Orientation of: PROF CAT José Barata
Co-orientation of: PROF AUX Ricardo Moura

The Master Student, | *The Supervisor,*

Francisco Pereira | José Barata

Alfeite
2025

"O mundo não é isto, o mundo é bué cenas"

- Bruno Nogueira

I dedicate this work to my grandmother.

Acknowledgement

This work marks the conclusion of my journey at the Naval Academy, a demanding path that has shaped me both personally and professionally. I would like to express my gratitude to all those who, in one way or another, contributed to this stage of my life.

To my supervisor, Professor José Barata, I acknowledge the guidance provided during the course of this project. To my co-supervisor, Professor Ricardo Moura, I also note the suggestions and input shared along the way, especially through the inconveniences.

I wish, however, to extend particular thanks to Professor Hugo Policarpo, whose consistent availability, and practical advice made a decisive difference in the realisation of this work.

To my family, I am deeply thankful for the constant encouragement and support you have always given me, especially at such an important stage of my life.

To my mother, father and sister, a special note of gratitude. Without your example, values, and encouragement, none of this would have been possible. Thank you for being the foundation on which I stand today.

To my friends, the ones that have been there throughout the years of my life, for your steady friendship and for the good times we have shared throughout these years. Thank you, above all, for never keeping me grounded and always believing in me.

To Beatriz, thank you for being by my side, for your patience, your encouragement, and for bringing lightness and joy along the way.

To my colleagues from the Fernão de Magalhães course, for the friendship and camaraderie along the way, with a particular word to the “engineers” during this final stage.

To all of you, my sincere thanks.

Abstract

This dissertation explores the use of computational fluid dynamics (CFD) for generating synthetic data in the context of biomimetic propulsion. It contributes directly to the SABUVIS II project, which involves a swarm of autonomous underwater vehicles designed for military and scientific applications. The study focuses on designing, simulating and evaluating bio-inspired fin propulsion systems with the aim of producing synthetic datasets for future Digital Twin integration.

The objectives of this work are to develop a parametrized fin profile that can be easily and quickly modified in terms of both shape and movement, whether its amplitude, frequency of oscillation or the type of movement, in order to create a model for simulations and data generation. This model should be capable of running different simulations to generate a diverse set of results.

The methodology followed three stages. First, a bibliographic review mapped the state of research in biomimetic propulsion, synthetic data, and digital twins. Second, a CFD workflow modelled fin-driven propulsion, including fin profiling, mesh independence, domain setup, solver configuration, and UDFs for sinusoidal and turtle-inspired motions. Third, parametric simulations assessed flow velocity, thrust, hydrodynamic forces, energy use, and propulsion efficiency under controlled conditions.

Results show both movement types generate biologically consistent thrust and flow. Sinusoidal motion produced smoother velocity fields and steadier thrust, while turtle-inspired motion yielded localized peaks suited for rapid manoeuvring. Efficiency depended on fin length, frequency, and amplitude, with a 50 cm fin at 2 Hz giving the best thrust-to-energy ratio. The datasets also support synthetic data repositories and future digital twin development of the SABUVIS propulsion subsystem.

Keywords: Biomimetic UUV, Computational Fluid Dynamics (CFD), Simulation, SABUVIS, Synthetic Data

Resumo

Esta dissertação explora o uso da dinâmica de fluidos computacional (CFD) para gerar dados sintéticos no contexto da propulsão biomimética, contribuindo diretamente para o projeto SABUVIS II, que envolve um enxame de veículos subaquáticos autónomos. O estudo concentra-se no projeto, simulação e avaliação de sistemas de propulsão com barbatanas biomiméticas, com o objetivo de produzir conjuntos de dados sintéticos para futura integração com o Digital Twin.

Os objetivos deste trabalho são desenvolver um perfil de barbatanas parametrizado que possa ser fácil e rapidamente modificado em termos de forma e movimento, seja a sua amplitude, frequência de oscilação ou tipo de movimento, a fim de criar um modelo para simulações e geração de dados. Este modelo deve ser capaz de executar diferentes simulações para gerar um conjunto diversificado de resultados.

A metodologia seguiu três etapas. Primeiro, uma revisão bibliográfica mapeou o estado da pesquisa em propulsão biomimética, dados sintéticos e gémeos digitais. Em segundo lugar, um fluxo de trabalho CFD modelou a propulsão impulsionada por barbatanas, incluindo o seu perfil, independência da malha, configuração do domínio, configuração do *solver* e UDFs para diferentes movimentos. Em terceiro lugar, simulações avaliaram a velocidade do fluxo, o impulso, as forças hidrodinâmicas, o uso de energia e a eficiência da propulsão em condições controladas.

Os resultados mostram que ambos os tipos de movimento geram impulso e fluxo biologicamente consistentes. O movimento sinusoidal produziu campos de velocidade mais suaves e impulso mais estável, enquanto o movimento inspirado nas tartarugas produziu picos localizados adequados para manobras. A eficiência dependia do comprimento, frequência e amplitude da barbatana, com uma barbatana de 50 cm a 2 Hz proporcionando a melhor relação impulso/energia. Os conjuntos de dados também suportam repositórios de dados sintéticos e o futuro desenvolvimento de gémeos digitais do subsistema de propulsão para o projeto SABUVIS II.

Palavras-chave: UUV Biomiméticos, Dinâmica de Fluidos Computacional (CFD), Simulação, SABUVIS, Dados Sintéticos

Declaration

I declare that I used generative artificial intelligence tools to correct the spelling and semantics of the text.

Contents

List of Figures

List of Tables

List of Abbreviations

ATM	**A**lternative **T**urtle **M**ovement
AUV	**A**utonomous **U**nderwater **V**ehicle
BUV	**B**iomimetic **U**nderwater **V**ehicle
CAD	**C**omputer **A**ided **D**esign
CFD	**C**omputational **F**luid **D**ynamics
CSM	**C**lassical **S**inusoidal **M**ovement
DT	**D**igital **T**win
MUV	**M**anned **U**nderwater **V**ehicle
OSUG	**O**cean **S**cience **U**nderwater **G**lider
ROV	**R**emotely **O**perated **V**ehicle
SABUVIS	**S**warm of **B**iomimetic **U**nderwater **VIS** (vehicles)
SAR	**S**earch **a**nd **R**escue
UDF	**U**ser **D**efined **F**unction
UNav-Sim	**U**nderwater **Nav**igation **Sim**ulator
UUV	**U**nmanned **U**nderwater **V**ehicle

List of Symbols

c	chord (fin chord)	m
C_D	drag coefficient	–
C_L	lift coefficient	–
Co	Courant number	–
C_x	force coefficient in x	–
C_y	force coefficient in y	–
Δt	time-step size	s
η	efficiency	–
f	oscillation frequency	Hz
F_T	thrust force	N
F_x	instantaneous force in x (drag)	N
F_y	instantaneous force in y (lift)	N
L	characteristic length (fin chord)	m
μ	dynamic viscosity	Pa s
ν	kinematic viscosity	$m^2\,s^{-1}$
ω	specific dissipation rate (turbulence k–ω)	s^{-1}
P_L	average power loss	W
Re	Reynolds number	–
ρ	fluid density	$kg\,m^{-3}$
s	span of the flapping foil	m

τ_{wall}	wall shear stress	Pa
θ	instantaneous pitch angle (fin angle)	$^\circ$
$\theta_{\max}$	pitch amplitude	$^\circ$
U	characteristic velocity	$\mathrm{m\,s^{-1}}$
$\overline{u}$	area-weighted average velocity	$\mathrm{m\,s^{-1}}$
U_{fric}	friction (wall) velocity	$\mathrm{m\,s^{-1}}$
U_{∞}	freestream velocity	$\mathrm{m\,s^{-1}}$
y^{+}	dimensionless wall distance	–

Chapter 1

Introduction

Deep-sea exploration remains a significant challenge due to the hazardous and unstructured nature of the underwater environment. In response, the rapid development of Unmanned Underwater Vehicles (UUVs) has enabled researchers and engineers to overcome complex scientific and technical obstacles. UUVs are now widely used in a variety of marine operations, including seafloor mapping, ship hull inspection, oil and gas exploration, mine countermeasures, search and rescue and scientific data collection (Akçakaya et al., 2009; António, 2022; Zhu & Sun, 2013). The adaptability of this vehicles has led to the development of smaller, low-cost UUVs suitable for a wider range of applications (Bellingham et al., 1994; Wang et al., 2008).

Alongside conventional UUVs, advances in biomimetic robotics have introduced a new class of underwater systems known as Biomimetic Underwater Vehicles (BUVs), inspired by the morphology and locomotion of aquatic animals such as fish and marine mammals. These vehicles use undulating propulsion mechanisms instead of conventional propellers and its design provides improved manoeuvrability and energy efficiency, making BUVs well suited for tasks such as internal pipe inspection, oil spill monitoring, wildlife observation and coastal surveillance (Blidberg, 2001). In addition, their ability to operate in coordinated groups further enhances their operational effectiveness across a wide range of missions (António, 2022).

1.1 Motivation

In 1970, during the Apollo 13 mission, an explosion in the oxygen tank jeopardised the mission and the lives of all astronauts. In response to this crisis, the engineers from NASA had to devise an improvised solution without direct access to the source of the problem. The solution was to conduct a series of tests and simulations in real time, on an equal system from the Lunar Module. This entire process was executed within a span of less than four days (Uri, 2020). With this vision, the Digital Twin (DT) concept gained its basic fundament. The mission feasibility was only guaranteed because of the vast amount of data and knowledge.

Concurrently, the defence sector is confronted with mounting strategic and operational demands. The increasing complexity of maritime theatres – from contested littoral zones to deep-sea surveillance – is driving an urgent need for novel, adaptive, and stealth-oriented technologies (Dalaklis et al., 2024). Military forces are seeking platforms that can operate with greater autonomy, remain undetected for extended periods, adapt dynamically to mission variables, and be produced or modified rapidly in response to evolving threats. In this context, biomimetic underwater vehicles offer a pathway to quieter propulsion, improved manoeuvrability, and operational profiles that are difficult to achieve with traditional designs (Scipanov & Totir, 2023).

Modern component development typically combines theoretical design and experimental trials. Simulation technology brings a crucial mid step by generating synthetic data that yields deeper insight into predicted behaviour. Within the case of unmanned vehicles, this approach is significantly cheaper and accelerates the development cycle.

In such cases, Computational Fluid Dynamics (CFD) becomes a critical enabler. CFD facilitates the replication, prediction and optimisation of several fluid-structure, simple or complex, interactions in virtual environments, thereby eliminating many of the constraints associated with full-scale prototyping and open-water testing. It helps to explore the vast design space — encompassing varying fin geometries, movement patterns, and material properties — under simulated operational conditions, including those that would be hazardous, costly, or impossible to recreate physically. This has been demonstrated to accelerate innovation cycles, reduce material waste, and ensure that promising concepts can be validated and refined long before physical deployment (Versteeg & Malalasekera, 2007b).

1.2 Swarm of Biomimetic Underwater Vehicles (SABUVIS)

1.2.1 SABUVIS I

The SABUVIS project started in 2015 and ended its inaugural developmental phase, designated SABUVIS I, in 2019. This phase yielded the creation of three biomimetic vehicles, drawing inspiration from various living organisms with the goal of acting together forming a swarm (António, 2022; Araújo, 2020; Tukasiewicz, 2025).

The objectives of the project were the following:

1. Develop technology and technical expertise that enables a Portuguese company to expand its offering of underwater vehicles to include biomimetic vehicles.
2. Develop reinforcement learning techniques for controlling autonomous underwater vehicles.
3. Create a biomimetic UUV simulator and a development environment to facilitate the implementation of reinforcement learning techniques.
4. Conduct tests and develop operational concepts for biomimetic vehicles.
5. Provide the Armed Forces with a prototype of a biomimetic UUV that can be used operationally.
6. Identify the operational advantages of these systems and define directions for future developments.

Knowing that underwater vehicles are especially looking out for noises produced by the shafts and propellers of ships and other vehicles, another advantage highlighted for defence was the quieter system, making it harder to detect (Moore, 2019). Taking into account this information, different studies were developed, in an attempt to achieve a vehicle with these characteristics.

The BUV 1, developed by the Polish Naval Academy, is a BUV inspired by a seal with two tail fins and two smaller pectoral fins that simulate breaststroke swimming, as seen in Figure 1.1 ("Prezentacja finalna pojazdów SABUVIS", 2018).

FIGURE 1.1: BUV 1 - Developed by the Polish Naval Academy ("Prezentacja finalna pojazdów SABUVIS", 2018)

The BUV 2 was developed by the Krakow University of Technology, with the purpose of replicating a fish in its entirety with a single caudal fin and two pectoral fins, as seen in Figure 1.2 (Koh, 2019).

FIGURE 1.2: BUV 2 - Developed by the Krakow University of Technology (Koh, 2019).

Finally, the BUV 3 has a similar shape to the previous models, but it allows the tail module to be changed, alternating between a seal or fish type of tail. The latter was developed in Portugal, with *OceanScan* responsible for its mechanical construction, and the Laboratório de Sistemas e Tecnologia Subaquática (LSTS) - Faculdade de Engenharia da Universidade do Porto (FEUP) for its programming, in collaboration with the Escola Naval (EN). FEUP was responsible for the development of the vehicle's instrumentation and sensors, while the EN was responsible for programming the low-level controllers and artificial intelligence (AI) for the vehicle (António, 2022; Araújo, 2020).

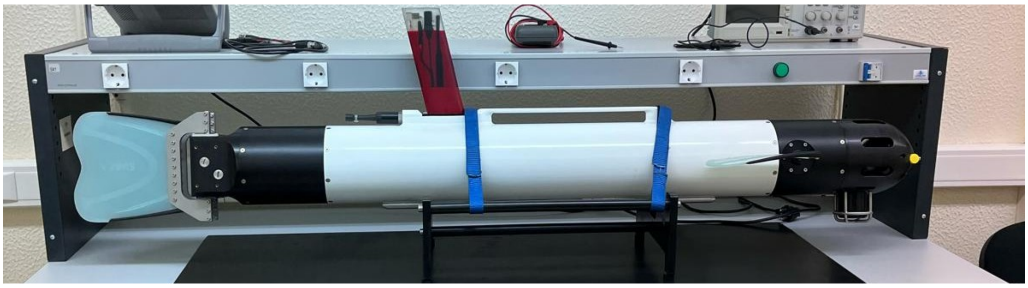

FIGURE 1.3: BUV 3 - Developed by EN/FEUP/OceanScan from Portugal

1.2.2 SABUVIS II

Upon completion of the initial phase of the project, a new challenge emerged: SABUVIS II. The primary objective of this stage is to develop technology for the cooperative control of a swarm of biomimetic UUV.

These vehicles will be divided into two groups: the leaders or controlling units (Swarm Leader Biomimetic Autonomous Underwater Vehicles (L-BAUV)), and the remaining members of the swarm, the executing units (Swarm Member Biomimetic Autonomous Underwater Vehicles (M-BAUV)). The control units will be equipped with more robust navigation and communications systems, transmitting information and tasks to the remaining executing units. In turn, these executing units will be equipped with less sophisticated and low-cost systems, whose function is to receive information about the mission and perform the necessary tasks. This division between leading and led vehicles facilitates the execution of various tasks, wherein, upon the directive of the controlling unit, the swarm can, for instance, divide to assess potential hazards across a broader area, subsequently returning to the initial formation, reporting the gathered information, and resuming navigation as a collective. The units undertaking the task, which are the least costly, are designated to confront potential risks (António, 2022). The requirements for an executing unit at this stage of the project are not particularly demanding (de Paiva, 2020). The requirements for the vehicle are as follows:

- Must be watertight;
- Capable of navigating to a maximum depth of 10 metres;
- Able to navigate autonomously or in a controlled manner through a pre-defined route;
- Cruising speed of 1 metre per second;
- Capable to hydrostatically vary the vehicle's immersion;
- An autonomy of two hours;
- Reduced cost.

Based on these requirements, the project was divided into several work areas, one of which focused on propulsion. The propulsion effort was further divided into sub-areas including tail/fin geometry (size and shape), material selection, actuation strategy, oscillation frequency and amplitude, and related kinematic parameters, among others.

1.3 Objectives

The primary objective of this dissertation is to contribute to the SABUVIS II project through the study, design, and simulation of biomimetic propulsion systems, with a particular focus on their hydrodynamic performance. The work is founded on the environmental, operational, and technological drivers outlined in the motivation, and aims to address three core goals:

1. **Comprehensive Review of Biomimetic Propulsion**
   A comprehensive bibliographic review of research and developments in the field of biomimetic underwater propulsion is to be conducted, with a view to identifying key parameters such as fin geometry, oscillation frequency, amplitude and motion profiles. This review establishes the scientific foundation for the simulations and contextualises the work within the broader effort to design low-noise, energy-efficient, and ecologically responsible marine propulsion systems.

2. **CFD-Based Parametric Study of Propulsion Configurations**
   The development and implementation of a computational workflow, utilising high-fidelity CFD tools, is imperative for the simulation of the performance of multiple fin configurations. The creation of a reusable pre-set model for SABUVIS II propulsion studies is a prerequisite for the incorporation of variations in fin length, oscillation frequency, and movement type. The simulations are designed to provide quantitative metrics, including expected thrust, efficiency, and energy consumption, under controlled virtual simulated conditions. These conditions reflect realistic mission profiles and hydrodynamic constraints.

3. **Generation of Synthetic Data for Digital Twin Integration**
   The generation of a structured synthetic dataset from the CFD results is imperative, as it will serve as the foundation for future SABUVIS projects. This dataset encapsulates propulsion performance across a range of operational parameters, thereby enabling predictive modelling, optimisation, and potential real-time decision-support, obviating the necessity for repeated, costly, and potentially disruptive field trials (Jones et al., 2022). These synthetic data and models may establish the calibration and validation basis for a high-fidelity DT of the SABUVIS propulsion subsystem.

In achieving these objectives, the work delivers both scientific insights, into how biomimetic propulsion characteristics influence performance and practical outputs, including validated simulation templates and datasets that can be directly integrated into future SABUVIS II development stages. Ultimately, this aligns with the broader strategic aim of delivering a propulsion solution that meets modern military performance requirements while minimising environmental impact, complying with the environmental responsibility, military technological ambition, and advanced simulation capabilities.

1.4 Thesis Structure

This dissertation is organised into five chapters and a conclusion to summarize key findings, supported by appendices that contain supplementary material and implementation details. Chapter 1 introduces the context and motivation for the research, linking the growing environmental pressures, the military demand for advanced underwater technologies, and the enabling role of CFD analysis. It presents the SABUVIS project, outlines its first and second phases, and defines the objectives and scope of the present work.

Chapter 2 presents a State-of-the Art on the subjects relevant to this study. It includes an overview of UUVs and their subtypes, an analysis of synthetic data generation techniques and their applications, an introduction to the DT concept with particular emphasis on military uses, and an introduction to CFD applications, with particular focus on biomimetic propulsion research.

Chapter 3 details the computational and theoretical basis for the CFD simulations performed, covering the governing equations of fluid flow, turbulence modelling approaches, geometry preparation, mesh generation, solver configuration, and post-processing methods. The rationale behind the selected simulation parameters and movement profiles is also explained.

Chapter 4 describes the implementation of the chosen CFD workflow methodology, including fin profile design, mesh independence studies, computational domain setup, and solver execution. It presents and analyses the simulation results in terms of velocity fields, hydrodynamic forces, energy consumption, and propulsion efficiency for various configurations and movement patterns.

Chapter 5 presents the results from the study and a concise discussion on the data revealed from it. This chapter is divided in three sections, the velocity analysis, with a comparison between the different types of movement, the forces and energy produced by the fin, and the expected efficiency. The present study investigates the dynamics of fluid flow velocity in relation to the movement of a fin.

Finally, Chapter 6, the conclusion and future works, summarises the key findings of the research, discusses their implications for the SABUVIS II project, and proposes directions for future work, including the integration of the generated synthetic data into a DT framework. The appendices provide supporting calculations, additional simulation scripts in the form of User Defined Functions (UDFs), and extended technical details, ensuring reproducibility and facilitating further development based on this work.

Chapter 2

State-of-the-Art

In order to understand this dissertation, this chapter focusses on the current State-of-the-Art on UUV, Synthetic Data applications, Digital Twin, considering it is the big picture of this work, and an introduction for CFD, with particular focus on water simulations.

2.1 Unmanned Underwater Vehicles (UUV)

The development of fully submerged vehicles began in the 18th century, initially for deep-sea exploration. However, the military potential quickly became evident, driving rapid advancements. A key milestone was the *Turtle* (Figure 2.1), designed by David Bushnell during the American War of Independence, recognized as the first military submersible (Stevens & Westcott, 1920).

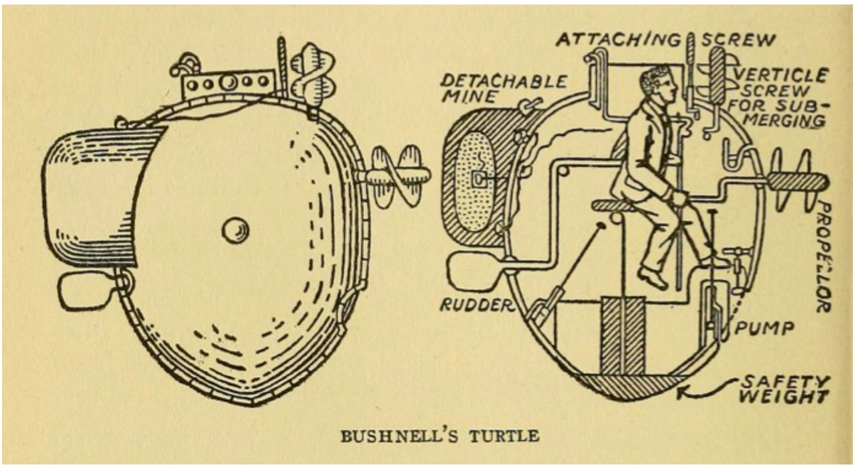

FIGURE 2.1: *Turtle* from David Bushnell (Stevens & Westcott, 1920)

Subsequent technological advancements have enabled the categorisation of these vehicles into two distinct classifications. The Manned Underwater Vehicle

(MUV) such as the submarines, made popular during the World War II, while the UUV is a form of drone. One definition of UUV is (Navy, 2004):

> "Self-propelled submersible whose operation is either fully autonomous (preprogrammed or real-time adaptive mission control) or under minimal supervisory control and is untethered except, possibly, for data links such as a fiber-optic cable."

This category can be further subdivided into two additional subcategories: the Remotely Operated Vehicle (ROV) and the Autonomous Underwater Vehicle (AUV) (Blidberg, 2001; Masmitja et al., 2018; Watts, 2009).

2.1.1 Remotely Operated Vehicles (ROV)

In the context of this thesis, ROV are UUV controlled through an umbilical cord connected either to land or to a ship nearby. Figure 2.2 shows different types of configurations for these vehicles.

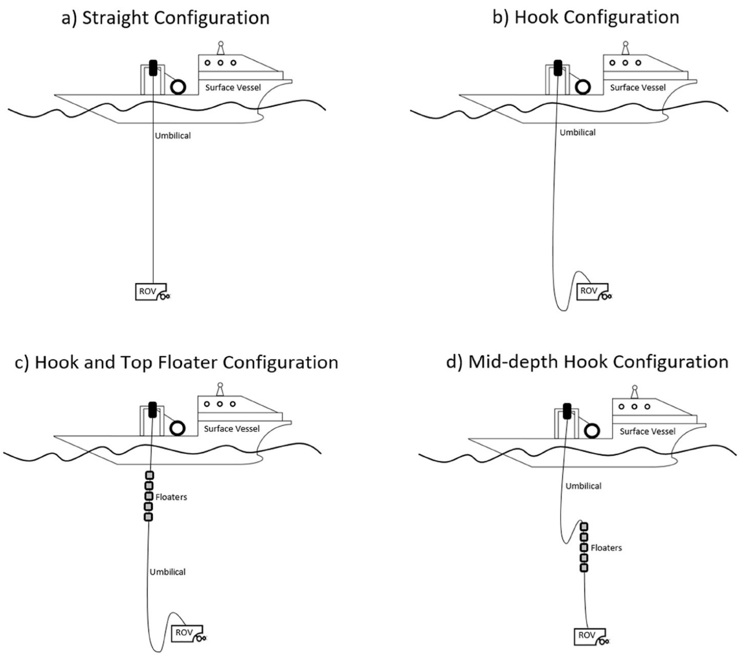

FIGURE 2.2: Different types of ROV configurations (Lubis et al., 2021)

RoboPike

Also developed by MIT, is an 82 cm long biomimetic vehicle inspired by the northern pike (Esox lucius), known for its fast turning and acceleration. Unlike the RoboTuna, it has only three tail joints, as seen in Figure 2.3, making it more compact

(Mazlan & Naddi, 2015; M. S. Triantafyllou et al., 2000). A key improvement is its ability to swim freely without being tethered to a test tank. However, it is still remotely controlled and not fully autonomous.

FIGURE 2.3: RoboPike, from the website of MIT

Source: http://robosapiens.mit.edu/wanda.htm

2.1.2 Autonomous Underwater Vehicles

A literature review on current AUV, with their functionalities and limitations, was performed (António, 2022). The following sections provide a brief overview, along with additional insights on recent developments.

Underwater Gliders

Underwater gliders use variations in buoyancy for propulsion. By adjusting the ballast using battery-powered pumps, these vehicles control their vertical movement: filling the ballast tanks increases weight, causing descent (negative buoyancy), while emptying them reduces weight, allowing ascent (positive buoyancy). This vertical movement, combined with the hydrodynamic effect of lateral rudders (or wings), generates lift and drag forces that ease horizontal movement. The propulsion mechanism relies on cyclical ballast adjustments and varying wing angles to produce a characteristic glide path.

Although gliders operate at lower speeds than other AUVs, their energy-efficient buoyancy control significantly extends the duration of operation. This extended autonomy makes them well suited for long-term missions, including oceanographic research and surveillance. Equipped with sensors, they collect data on temperature, salinity and oxygen levels over large areas and depths.

Three glider examples presented previously (António, 2022) are:

Slocum - This modular vehicle (seen in Figure 2.4) is approximately 1.5m long, weighs 55-70kg depending on configuration, has a range of 13,000km and can operate at depths of up to 1,000m for up to 18 months.

FIGURE 2.4: Slocum Glider

Liberdade XRAY - One of the largest in its class, as seen in Figure 2.6, with a wingspan of 6.1m, highly efficient in terms of hydrodynamics. It can reach speeds of 1-3 knots, a maximum range of 1,500km, an autonomy of around 6 months and can dive to depths of up to 365m. The XRay is designed to be extremely quiet, making it difficult to detect. Its primary mission is to locate submarines operating in its waters using its sensors and systems.

FIGURE 2.5: Liberdade Glider

The Open-Source Underwater Glider - Released in 2017, with a longer body and slimmer wings (see Figure 2.6), allows low cost production and has a versatile utilization on data collection either in deep sea or shallow water (Hackaday, 2017).

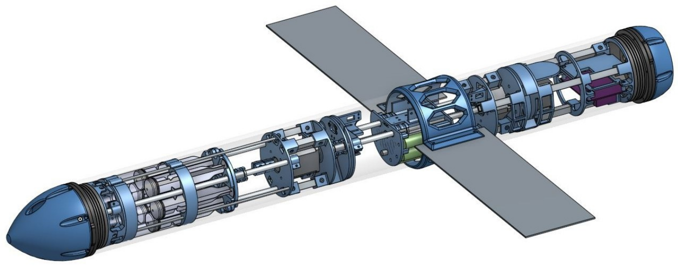

FIGURE 2.6: OSUG

Transitioning into a connection between UUV and DT, a DT of a blended-wing-body UUV glider (seen in Figure 2.7) was developed, by building a platform (water tank) for simulations using DT technology, through the software Gazebo, with the sensor data integrated in the proportional–integral–derivative (PID) control algorithm, combined with a robot operating system (ROS) for control (Hu et al., 2023).

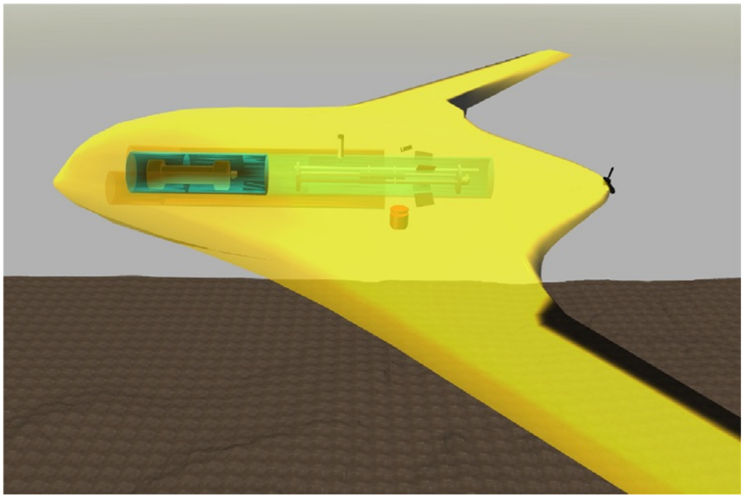

FIGURE 2.7: DT of blended-wing-body glider (Hu et al., 2023)

The project began with the identification of the characteristics of effective gliders through research and testing, incorporating considerations of hydrodynamics, weight distribution, and wing shape. Initial studies utilised sketches and Computer Aided Deseign (CAD) software to formulate design concepts, which were subsequently evaluated and refined based on feedback and testing outcomes. The manufacturing process involved precise cutting, assembly with adhesives, and the addition of features such as tail fins for stability. Subsequent test dives were conducted to assess the performance of the gliders, and the designs were iteratively refined based on the feedback obtained.

Conventional Propulsion UUV

This category consists of UUVs that are powered by conventional means, i.e. through propellers. The propulsion and maneuverability of these AUVs is influenced by the number of propellers and rudders along the body of the vehicle, as well as its orientation and relative position (Masmitja et al., 2018). These factors influence the direction in which external forces act, making it possible to control the vertical and horizontal movements of the device and have shown to exhibit both high speed and reasonable manoeuvrability at the cost of higher energy consumption, reducing its autonomy. This is the most common propulsion configuration, with different adaptations to achieve their purpose. The following section presents some examples of propeller-driven AUVs that had been developed up to 2022 (António, 2022):

Remus

The company manufacturing this AUV has 4 different models. The Remus 100, 300, 620 and 6000, all allusive to the depths they reach. The REMUS 100 vehicle for example (Figure 2.8), was designed for both scientific and military missions, including mine-clearing and search and recovery. Used by the US Navy in 2003, the vehicle measures 1.6 meters and weighs 37 kg. It operates at depths of up to 100 meters and has a top speed of 5 knots. Depending on speed, it can run for 8 to 22 hours. The military version, seen in Figure 2.8, uses sonar and software to detect mines along a pre-programmed route of up to 60 miles.

FIGURE 2.8: Remus 100 (Huntington Ingalls Industries (HII), 2021)

MEDUSA

The MEDUSA DEEP SEA vehicle was developed by CEiiA and the Institute of Systems and Robotics for deep-sea scientific missions. It can operate at depths of up to 3000 metres, with a 10-hour autonomy and a range of 50km.

The vehicle, see Figure 2.9) has a dual-torpedo-shaped vertical body, weighs around 300kg, and is 2.8 metres long. It uses four thrusters — two vertical and two horizontal — for manoeuvring. This setup allows it to reach speeds of up to 3m/s and handle similarly to the MARES AUV.

FIGURE 2.9: MEDUSA (Instituto Superior Técnico, 2017)

MARES

The MARES AUV, seen in Figure 2.10, was developed by the University of Porto to perform a variety of tasks, including pollution monitoring, scientific data collection, sonar mapping, video capture, and mine countermeasures. The vehicle is distinguished by its modular design, which helps the integration of diverse sensors and systems, allowing for customised configurations to suit the specific requirements of each mission.

Common features from the MARES AUV, across all configurations, include a length of 1.5 metres, a weight of approximately 32 kilograms, a depth capability of 100 metres, an autonomy of 10 hours, and a range of 40 kilometres. The vehicle is equipped with four thrusters, two of which are positioned horizontally to provoke forward movement, while the remaining two are arranged vertically to enable diving and surfacing capabilities.

This propulsion configuration facilitates precise manoeuvring in confined spaces making it ideal for tighter spaces (Cruz & Matos, 2008).

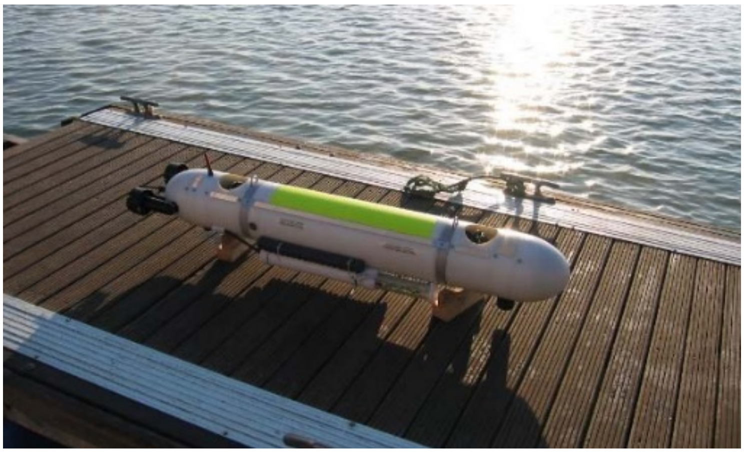

FIGURE 2.10: MARES (Cruz & Matos, 2008)

Biomimetic Propulsion UUV

Taking inspiration from living organisms and applying their principles of motion to robotics - particularly in AUVs - can offer significant advantages over conventional propulsion systems. Traditional AUVs often rely on multiple propellers to achieve manoeuvrability, which can lead to high energy consumption. To overcome these limitations, a new category of vehicles has emerged: biomimetic UUVs. Known as BUVs, these vehicles are designed to mimic the swimming behaviour of fish in order to improve propulsion efficiency and underwater manoeuvrability (Mazlan & Naddi, 2015).

Fish locomotion is generally divided into two main types: Body and/or Caudal Fin (BCF) propulsion and Median and/or Paired Fin (MPF) propulsion. In the BCF (Figure 2.11a), the fish flexes its body and tail to generate thrust, allowing for powerful propulsion, high speeds and rapid acceleration. In contrast, MPF (Figure 2.11b) relies on the movement of the pectoral, dorsal or pelvic fins, resulting in lower swimming speeds, but providing finer control and more precise manoeuvring. These biological movement patterns can be further classified as undulatory - where the body or fins produce wave-like movements - or oscillatory, where the fins oscillate around a fixed point. By mimicking these natural mechanisms, BUVs can perform more efficiently and adapt better to complex underwater environments (Sfakiotakis et al., 1999).

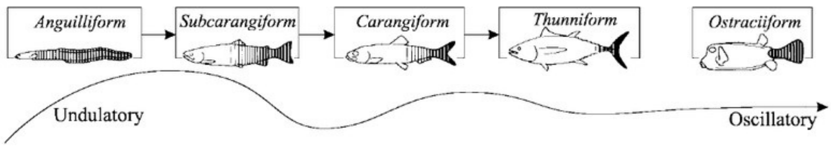

(A) Body and/or Caudal Fin

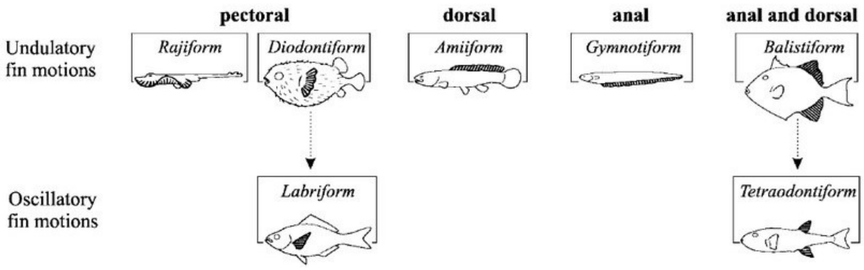

(B) Median and/or Paired Fin

FIGURE 2.11: Different fish motion, with shaded areas indicating moving parts (Sfakiotakis et al., 1999)

A review on some of the biomimetic propulsion AUV previously performed shows the following examples (António, 2022):

RoboTuna

The RoboTuna, developed in 1994 by MIT (Liu & Hu, 2004), is recognised as the first biomimetic underwater vehicle, inspired by the movement of a tuna as seen in Figure 2.12. Measuring around 1.25 metres, it features a tail with eight linked joints and a lunate fin, allowing it to mimic natural fish motion. The joints are driven externally by six servomotors using pulleys and cables to replicate muscle action. Its body is covered in foam and Lycra to reduce water turbulence. Equipped with sensors along its body, RoboTuna was used to study and optimise swimming mechanics, laying the groundwork for future biomimetic designs (Mazlan & Naddi, 2015; Techet et al., 2003; M. S. Triantafyllou & Triantafyllou, 1995).

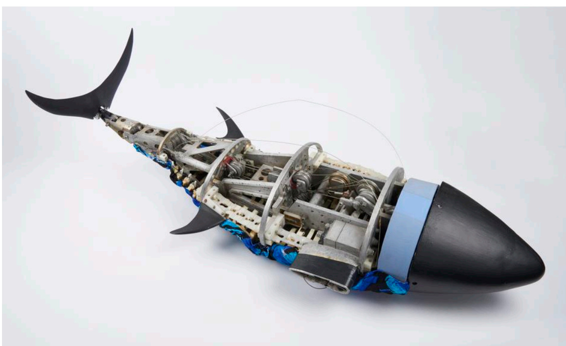

FIGURE 2.12: RoboTuna (Group, 1995)

VCUUV

Developed by Draper Laboratories and inspired by the RoboTuna, the Vorticity Control Unmanned Underwater Vehicle (VCUUV) mimics the yellowfin tuna (Thunnus albacares).

It measures approximately 2.4 metres, weighs approximately 173 kg and can reach speeds of 1.25 m/s with a yaw rate of 75°/s (see Figure 2.13). Its large size allows it to carry a variety of sensors and equipment. The vehicle's motion is provided by a flexible tail made up of four independently operated segments controlled by hydraulic cylinders. This arrangement enables precise, autonomous manoeuvring based on compass feedback (J. M. Anderson & Chhabra, 2002; Mazlan & Naddi, 2015).

FIGURE 2.13: VCUUV (J. M. Anderson & Chhabra, 2002)

RoboSalmon

The RoboSalmon is a low-cost biomimetic vehicle developed by the University of Glasgow and inspired by the Atlantic salmon, seen in Figure 2.14. It has been designed to test the effectiveness of biomimetic propulsion systems.

Measuring approximately 0.85 metres, it consists of a main body containing sensors and batteries, and a tail with ten articulated joints, the last of which is connected to a caudal fin. These joints are flexed using a servo motor and cable system to mimic the movement of salmon. Tests have shown that it can reach a maximum speed of 0.2 m/s with a tail oscillation frequency of 0.6 Hz and an amplitude of 0.15 m (Mazlan & Naddi, 2015; Watts, 2009).

FIGURE 2.14: RobotSalmon (Watts, 2009)

ABPP2

The ABPP2 is a vehicle designed and built in Poland as part of the Śledzik project, which ran from 2013 to 2017. Led by the Polish Naval Academy in collaboration with the University of Krakow, PIAP and Forkos Company, the project aimed to develop torpedo-shaped BUVs with undulating propulsion, mimicking the movement of fish, seen in Figure 2.15. The vehicle has a cylindrical body, 1.7 metres long and 0.2 metres in diameter, with a trapezoidal tail fin at the rear. Its propulsion system consists of a single articulated segment, with the caudal fin oscillating at different frequencies, and two pectoral fins for additional thrust and depth control. The vehicle is equipped with modular systems including video, sonar, communications, navigation sensors, batteries and electronics (Szymak, 2016; Szymak & Przybylski, 2018).

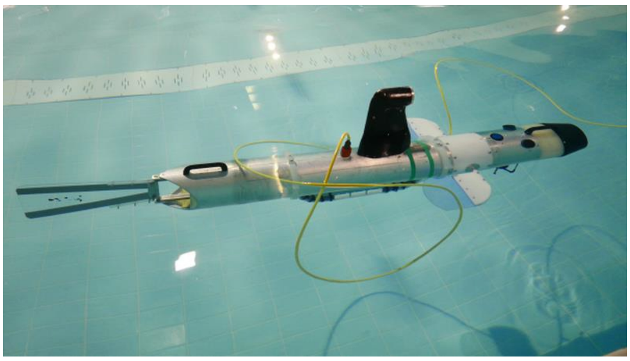

FIGURE 2.15: ABPP2 (Szymak, 2016)

2.2 Synthetic Data

Synthetic data refers to artificially generated datasets that replicate the statistical and structural properties of real-world information. It is increasingly used to train machine learning models, validate digital twins, and simulate environments where real data are scarce, costly, or sensitive. Applications span healthcare (D. F. Bauer et al., 2021), finance, robotics, and defence, offering safe, scalable, and controlled testing conditions (Raghunathan, 2021).

In engineering, physics-based simulations such as CFD provide reliable synthetic datasets without the need for extensive physical trials. These advantages make synthetic data particularly valuable in the development and optimisation of UUVs (F. Lee et al., 2025; J. Lee et al., 2023, 2024).

Training UUVs to operate autonomously is a complex procedure. The environment they encounter is often unknown, so it is not as straightforward a process as it is for ground or air robotic systems. The amount of data necessary to teach these vehicles is hard to obtain. Several variables come into play, such as propulsion (speed and energy), the environment (current, waves, temperature and density), and other factors. While environmental variables can be obtained through historical datasets, propulsion data for these kinds of vehicles is insufficient due to their different characteristics (Raghunathan, 2021).

Instead of being collected via physical experiments or field tests, synthetic data is produced by algorithms – for example by computer simulations – so that they "stand in" for real observations. Physics-based simulators (e.g. computational fluid dynamics or robotics simulators) can compute the outcomes of known models under varied conditions and generative models (such as Generative Adversarial Networks or diffusion models) can create realistic images or sensor readings by learning from limited examples, while data augmentation can take existing real data and change it slightly by adding noise, geometric distortions or varying parameters to create new, labelled instances.

In all cases, the goal is to replicate key features of the true data distribution, without measuring every situation in reality. It was noted that synthetic data "offer a multitude of compelling advantages" by streamlining training, testing and deployment of AI systems (A. Bauer et al., 2024).

2.2.1 Techniques for Generating Synthetic Data

Physics-Based Simulation

A widely used approach to synthetic data generation in marine engineering involves physics-based simulations. These utilise high-fidelity models, such as CFD or robotic simulators (e.g., Gazebo, Stonefish, UNav-Sim), to calculate vehicle responses under varying control inputs and environmental conditions. Figure 2.16 shows a simulation in UNav-Sim that allows researchers to develop and test algorithms for underwater environments efficiently. For UUV propulsion systems, this enables the generation of labelled data that represent vehicle motions, forces, and thruster performance without physical testing (Amer et al., 2023).

FIGURE 2.16: UNav-Sim example simulation. The bottom right displays the feed from a front-facing RGB camera, while the bottom left shows a corresponding depth image (Amer et al., 2023)

Data-Driven Generative Models

Generative models, such as Generative Adversarial Networks (GANs) and diffusion models, can synthesise realistic sensor or control data based on a learned distribution from limited real examples. These models are particularly beneficial for producing sonar readings, image data, or force profiles that reflect operational variability (D. F. Bauer et al., 2021). Their utility lies in their flexibility, though they may lack the physical grounding of physics-based simulators.

Data Augmentation

The data augmentation process involves the application of systematic transformations to existing real data with the objective of generating novel examples. In the field of propulsion modelling, this may encompass modifications to fin-motion sequences or the introduction of noise into sensor readings. Although augmentation is less complex than generative models, it maintains fidelity with real measurements and is frequently employed in conjunction with simulations in “simulated-to-real” workflows (Jain et al., 2022).

2.2.2 Advantages and Limitations of Synthetic Data

A major advantage of this system is its cost efficiency and the swiftness in its operating method. The generation of synthetic datasets by algorithmic means allows rapid iteration, removing some of the financial and logistical challenges typically associated with physical testing. Simulations have been shown to be capable of being executed orders of magnitude faster than real-world trials (F. Lee et al., 2025). This acceleration in the design and evaluation process is a significant benefit. A further salient benefit is that of safety and accessibility. The undertaking of experiments in underwater environments is inherently hazardous, often entailing considerable logistical challenges. Such challenges may include deployment at depth, adverse conditions, and the retrieval of equipment. Synthetic testing, in contrast, completely bypasses physical hazards and facilitates experimentation in scenarios that would otherwise be impractical or impossible to access (Amer et al., 2023).

It is evident that synthetic data offers unparalleled diversity and scalability. As the data are artificially generated, it is possible to produce an infinite quantity of data, complete with accurate and consistent ground-truth annotations (A. Bauer et al., 2024).

Notwithstanding the numerous advantages of synthetic data, it is imperative to exercise caution and give due consideration to the limitations inherent in this technology. A significant challenge is the reality gap, which refers to the discrepancy between simulated environments and the complexities of the real world. The issue of simulated-to-real transfer can be traced back to the inherent limitations of simulations, which may encompass simplifications or modelling errors, thus hindering their capacity to accurately replicate the intricacies of physical systems and environmental dynamics. Furthermore, the use of high-fidelity simulations, whilst being imperative in the pursuit of more precise representations, engenders a substantial computational burden.

The high resource demands of these simulations can impose constraints on the number of scenarios that researchers can explore within the confines of practical time and hardware limitations (A. Bauer et al., 2024).Another concern is the risk of over fitting to synthetic biases. Should the generation of data be based upon flawed or overly narrow assumptions, the resulting synthetic dataset may be found to misrepresent real-world variability. This may result in trained models that are brittle or biased when deployed. Finally, it is important to acknowledge the persistent significance of validation requirements within the development pipeline. It is demanded that models trained exclusively on synthetic data are evaluated against real-world measurements to ascertain their reliability and generalisability (Amer et al., 2023; D. F. Bauer et al., 2021).

2.2.3 Synthetic Data Applications

As explained previously, high-fidelity simulators are used to generate synthetic sensor inputs and vehicle responses, enabling researchers to model scenarios that are costly or dangerous to replicate in the field (Amer et al., 2023). A multi-purpose, photo-realistic synthetic dataset, with ground truth for stereo, segmentation, and depth, for underwater navigation and inspection named MIMIR-UW was also developed (Álvarez-Tuñón et al., 2023). This dataset helps "bridge the gap between theory and application in underwater environments", displayed in Figure 2.17.

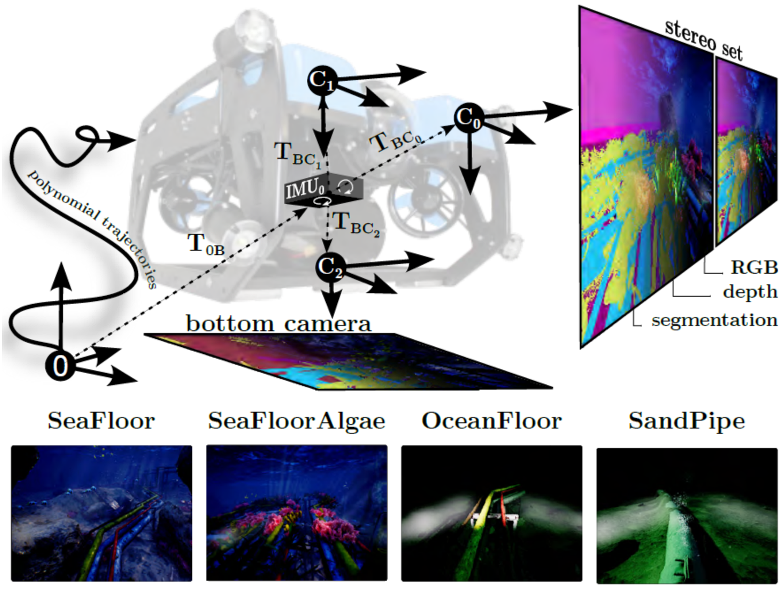

FIGURE 2.17: MIMIR-UW dataset gathering pipeline: a camera rig consisting of a stereo set and a downward-looking camera recording RGB, depth, and segmentation in four underwater environments. The robot follows polynomial trajectories with varying speeds and accelerations (Álvarez-Tuñón et al., 2023).

This illustrates the MIMIR-UW dataset structure and components: a simulated underwater robot follows a polynomial trajectory (left), collecting data with a bottom-facing stereo camera and Inertial Measurement Unit (IMU). The 3D layout includes transformations between the robot base, IMU, and camera frames. On the right, the stereo pair produces RGB images, depth maps, and semantic segmentations. At the bottom, four example environments are shown: *SeaFloor*, *SeaFloorAlgae*, *OceanFloor*, and *SandPipe* — demonstrating the diversity and realism of the synthetic dataset.

A different study focused on leveraging synthetic data to efficiently train collaborative robots within a virtual environment before deployment in the physical world (Kim et al., 2024). The approach begins by generating synthetic point cloud data that simulates real-world object interactions, creating a DT environment where the robot can learn safely and at scale.

This data is used to train 3D object classification models, enabling the robot to recognise and differentiate between various items in its surroundings, as seen in Figure 2.18.

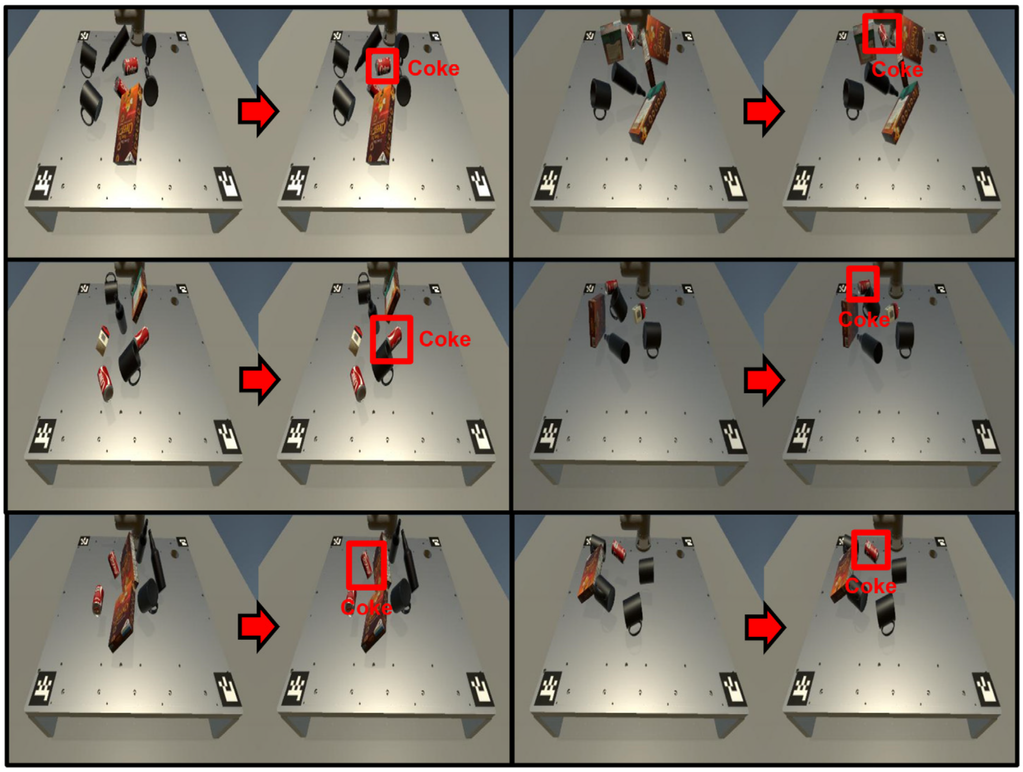

FIGURE 2.18: Synthetic data-based object detection training scene (Kim et al., 2024)

Once training is complete, the learned policies and models are transferred back into the real robot, enabling it to operate autonomously and safely in real environments with minimal manual programming. This synthetic-data-driven pipeline significantly reduces development time, increases adaptability to new tasks, and enhances the safety and efficiency of collaborative robots in dynamic industrial applications. Synthetic data are frequently used to train surrogate models that map inputs (e.g., actuator signals) to outputs (e.g., thrust, power consumption). For instance, in flapping-fin propulsion, a study showed a trained inverse controller using synthetic thrust sequences, bypassing the need for real-world data during early development (J. Lee et al., 2023, 2024).

Controllers designed for UUV propulsion can be tested across diverse virtual environments, including varied flow conditions, disturbances, and failure modes, without physical risk (Amer et al., 2023). Synthetic datasets allow rapid evaluation of multiple fin geometries or propeller designs. Once trained, a surrogate model can predict performance metrics across large parameter spaces in real time (Zhou et al., 2024).

By including adverse scenarios (e.g., actuator failure, sensor noise), synthetic data facilitates the training of robust models capable of handling rare or unexpected conditions. The generation of synthetic data assists in the creation of realistic, diverse datasets, particularly in scenarios where real-world data is limited, sensitive, or costly to acquire. In the context of this dissertation, the synthetic data in question is to serve as the foundational element for the development of a DT.

2.3 Digital Twin

Even though the Digital Twin (DT) application can be traced as far as the NASA in land simulation, the concept as it is now known dates only to 2002, in the University of Michigan, on a presentation for Product Lifecycle Management (PLM)(Grieves & Vickers, 2016). Being a top trend from 2017 to 2019 (Gartner, 2019), many studies and attempts have been made to find a universal definition for a DT.

The exponential curve associated with the number of publications directly related to DT, since 2005 up to 2022, especially related to engineering, computer science, math, physics and energy problems (Emmert-Streib et al., 2023), is shown in figure 2.19:

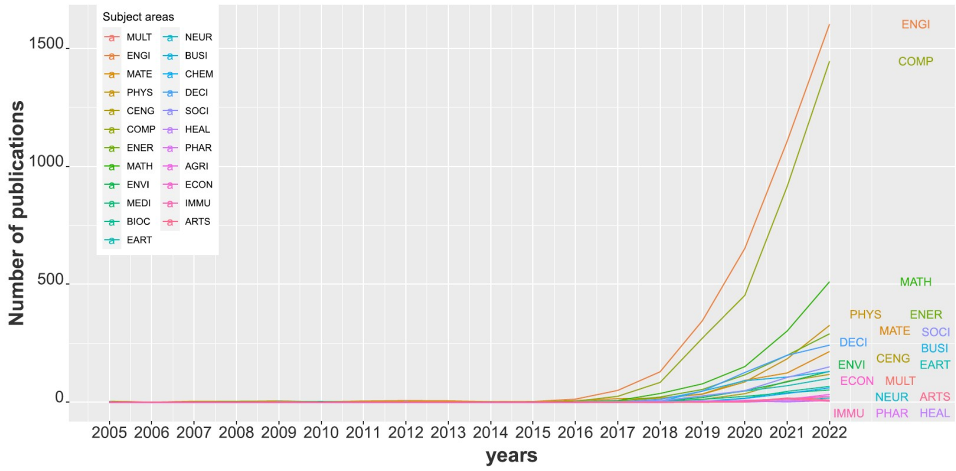

FIGURE 2.19: Evolution of the number of publications on DT over time (Emmert-Streib et al., 2023)

The possible applications of the technology can expand to smart cities, construction, manufacturing, agriculture and most industries with some logistical or mechanical process evolved (Tao et al., 2019). A DT needs only three elements (Grieves & Vickers, 2016): real space, virtual space and a link for data between them (Figure 2.20) and it is defined as a full virtual description of physical manufactured product, from atomic level to macro-geometrical level. In a perfect scenario, anything found on the physical model would also be found in it's digital representation.

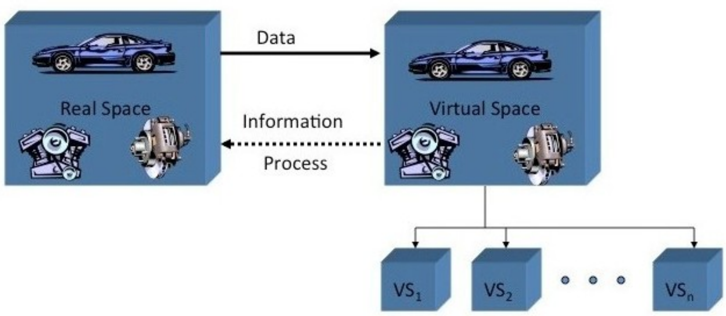

FIGURE 2.20: Conceptual Idea for PLM (Grieves & Vickers, 2016).

The DT is not a stationary model since it changes with the product, it can begin as a virtual model, from the create phase, while the physical form develops in production phase (Grieves & Vickers, 2016).

On the other hand, with the DT being used for simulation purposes, defining a DT as a "complex description at the functional and physical layer of a system, product or component, that integrates useful data, which can be of interest for all phases of the on-going and and subsequent life cycles” is a different possibility (Boschert & Rosen, 2016). In Figure 2.21 it is possible to see how the PLM and the link to the DT connect with one another, demonstrating its continuous evolvement with the product.

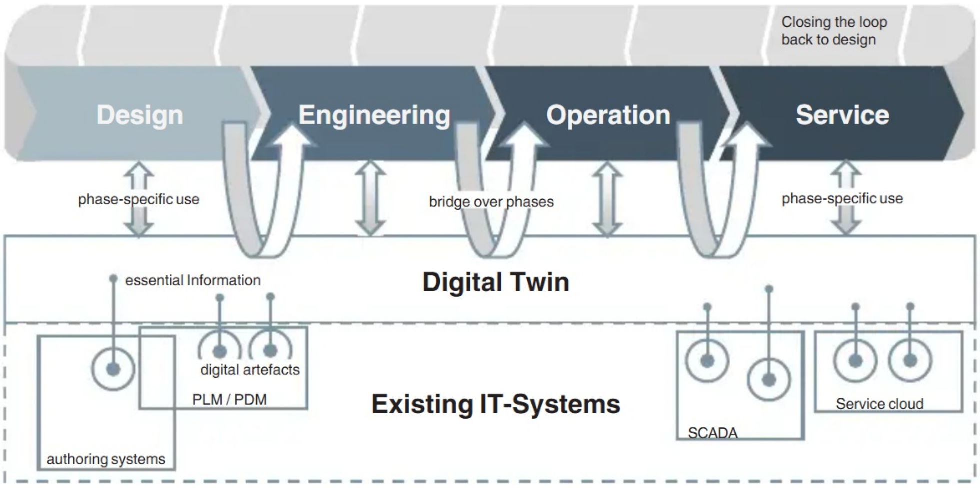

FIGURE 2.21: DT uses essential information from different IT systems (Boschert & Rosen, 2016).

Later in 2017, Elisa Negri presented a definition of DT for Industry 4.0 manufacturing, introducing the Cyber-Physical Systems (CPS) concept, related with DT, for real-time monitoring and synchronization of the real world, starting with medicine and maintenance, and later for mirroring the life of the physical entity (Negri et al., 2017):

> The Digital Twin is a production system virtual representation which can be executed on various simulation environments, through the synchronization between the real and virtual system, using mathematical models, appropriate information. connected intelligent devices and mathematical models.

In 2018, Negri presented a simplified definition, which states that "DT is the cyber part of a cyber-physical system (CPS)" (Autiosalo, 2018).

At last, Tao published a project of a Shop-Floor, an attempt at smart manufacturing, to achieve smart interconnection and interoperability between physical and virtual space and how DT can assist in product design, manufacturing and service with big data, by overcoming data fragmentation, isolation and stagnation due to the lack of convergence (Tao et al., 2017).

In contrast to the three dimensions proposed by Grieves, Tao proposes a five-dimensional model that incorporates the physical, virtual, connection, data, and service aspects (Tao et al., 2019). Through the evolution of the product, a virtual space emerges, as illustrated in Figure 2.22:

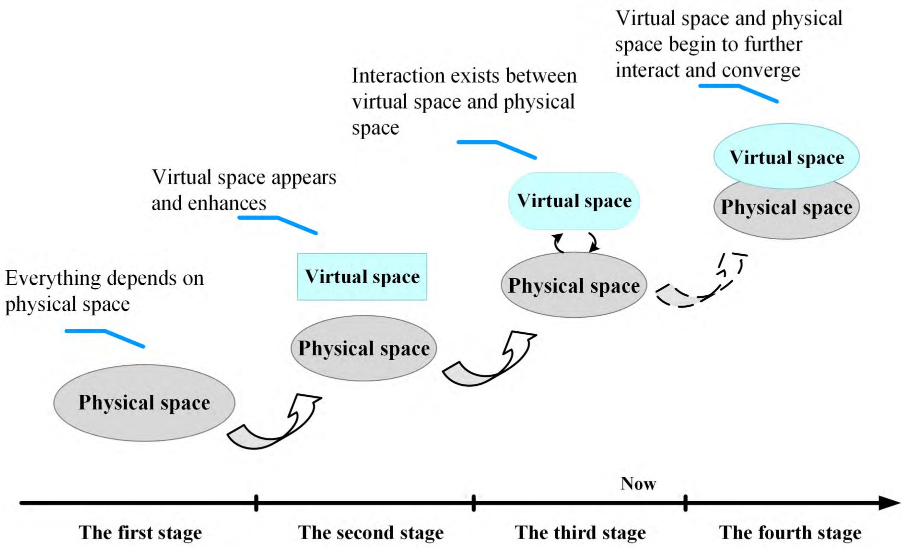

FIGURE 2.22: Evolution of a product process (Tao et al., 2019).

2.3.1 Digital Twin Military Applications

So far, no DT applications in the Portuguese Navy were set in motion. However, there have been published articles, thesis or conference proceedings on DT in the military worldwide.

Individual Combat Quadrotor

Later on, Ji developed a model of an individual combat quadrotor UAV, based of the Wang paper, considering the DT as a subset of the system, with all the right geometry, physics, behaviour and rules (Ji et al., 2021). The proposed architecture contains a Service Layer, the Twin Data Layer, Virtual Entity and Physical Entity.

The geometric model was built accurately using Solidworks and the physical model was adjusted to comply with the aerodynamics principles. The behaviour was controlled using a double closed loop cascade PID. Finally, the flight controller PX4 and its ground control station, ROS and its simulation simulator (Gazebo) were used to conduct joint experiment. The results are displayed in 2.23, and it is possible to see how accurate they were.

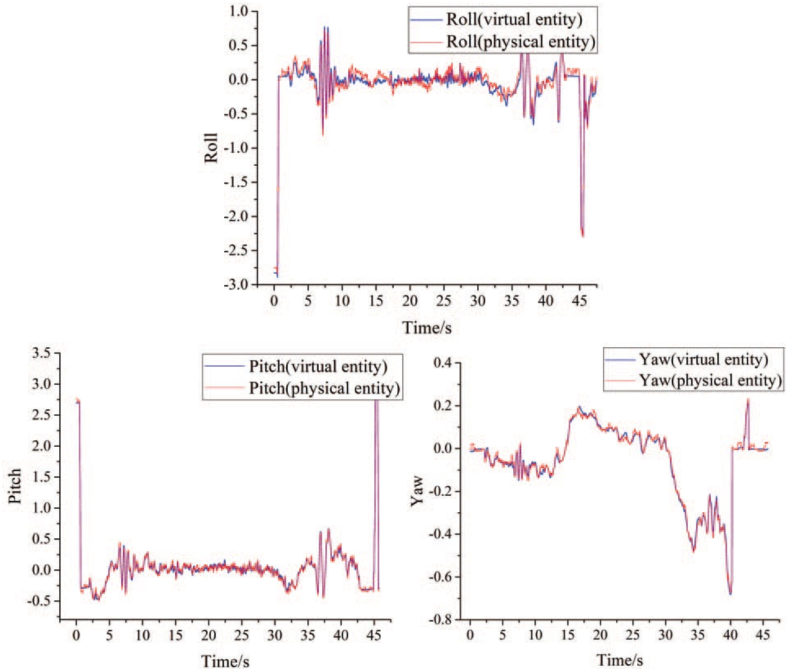

FIGURE 2.23: Quadrotor DT comparison of roll, pitch and yaw with physical entity (Ji et al., 2021).

Intelligent Maritime Scene Frame Prediction DT

A project for Search and Rescue (SAR) aimed to develop an intelligent maritime scene frame prediction, by creating a DT based scene of all the conditions such as wind, ocean currents and drift trajectories as well as the means available (Guo et al., 2021). The figure 2.24 displays a scenario with the DT architecture based on a new environmental encoder graph-attention network (Env-GAT). Compared to the GAT (without the encoder) the average displacement error was 13,3% lower as well as 9,5% on the final displacement error.

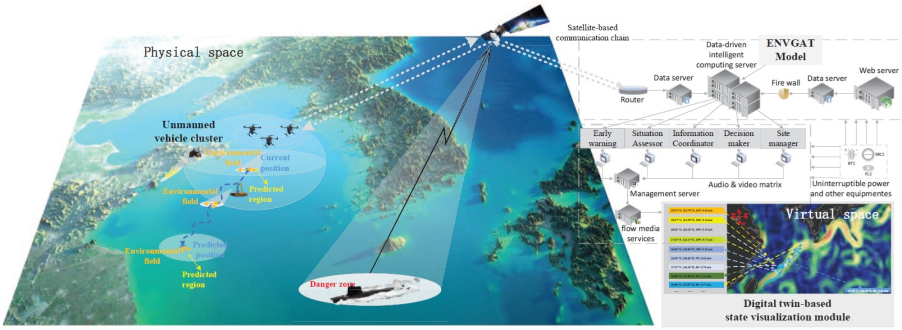

FIGURE 2.24: Physical and DT interaction and communication (Guo et al., 2021).

UAV landing DT

In the UAV theme, Uddin describes how DT can help with precision landing of the vehicles, using sensor data (from GPS, IMU and vision-based), error calculation and an optimization algorithm for better motion planning (Uddin et al., 2023). In that model, the DT could also analyse the effects of the wind, payload and other factors as well as the drone's status and performance in real time while presenting suggestions in case something goes wrong.

The drone was equipped with a Raspberry Pi, a camera, a pixhawk (controller), a GPS module and telemetry. For safety precautions, a manual controller was used to stop automation processes in case harmful anomalies. Figure 2.25 shows the difference of the before and after the implementation of the DT, with less turbulence, improving stability of the flight.

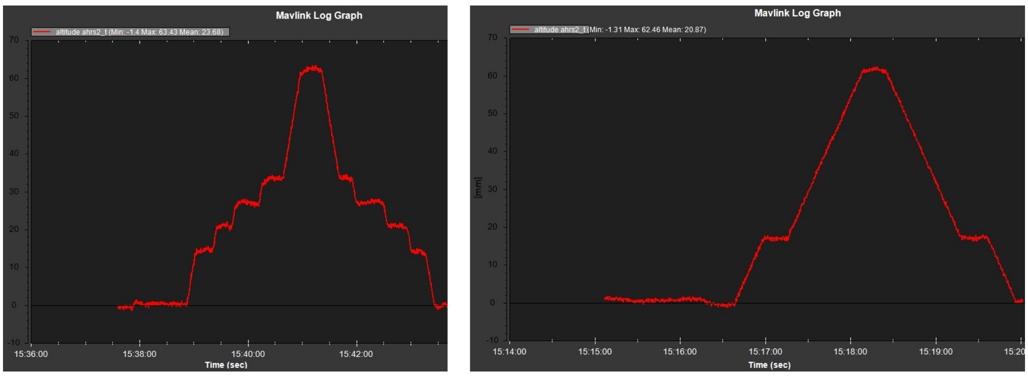

FIGURE 2.25: Analyses of altitude, before (left) and after (right) (Uddin et al., 2023)

The first flight check was made just 60 mm from the ground. After this, a bigger flight with 6 meters vertically and 10 meters horizontally.

Ground Vehicle

A DT for a military vehicle was developed, to enhance design processes and predictive maintenance strategies for PLM, to achieve onboard diagnosis (Eddy, 2024). Eddy developed a 14-degree-of-freedom virtual vehicle model using MATLAB/ Simulink/Simscape and its functionalities, with components like body dynamics, engine performance, wheel kinematics, driveline systems, and suspension characteristics. By collecting real-time data of the vehicle, a comparison with the virtual counterpart was made in order to increase reliability of the model. Lastly, Eddy ran several simulations of imputed faults, to understand the consequences and to study the model's response to said faults.

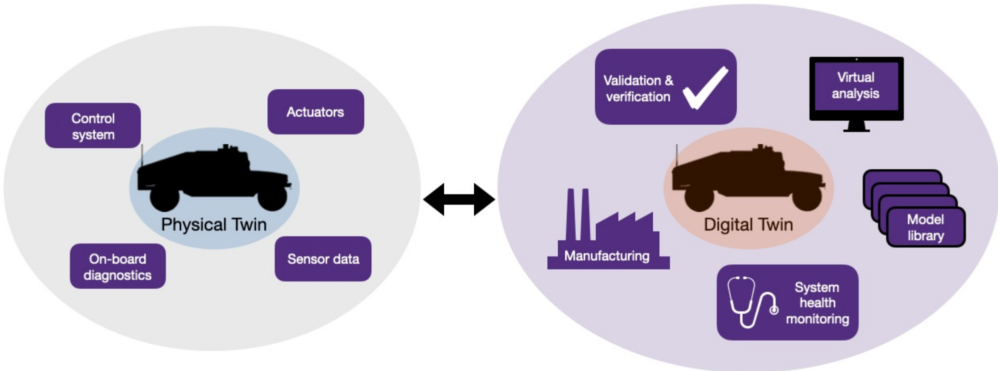

FIGURE 2.26: Physical and DT interaction and communication. (Eddy, 2024)

The DT model from Figure 2.26 aided in tradespace analysis, in cooperation with the Clemson University VIPR-GS Center, along side with machine learning for the predictive maintenance by creating 6 anomalies and leveraging statistical algorithms based on neural networks. The project achieved an 85% validation accuracy.

In other applications, talks of DT for defence operations in various combat domains, including Space, Maritime, Air, Land, and Cybersecurity keep growing.

2.4 Introduction to CFD

Computational Fluid Dynamics (CFD) is the term given to the numerical simulation of fluid flow, heat transfer, and related physical phenomena, including chemical reactions. These phenomena are modelled using computer-based systems. The primary objective of advancements in CFD is to establish a predictive capability that is commensurate with other computer-aided engineering (CAE) tools.

The increasing accessibility of high-performance computing and the development of intuitive user interfaces have significantly expanded the industrial adoption of CFD, particularly since the 1990s (Versteeg & Malalasekera, 2007b).

In contrast to experimental approaches, where the cost typically increases with the number of test cases and measurement points, CFD offers the ability to generate large datasets with minimal additional computational expense. This makes it especially effective for parametric analyses and performance optimisation tasks in the domain of engineering design.

2.4.1 Biomimetic Studies

Relationships between the fish body and caudal fin

By employing two-dimensional CFD simulations to investigate the impact of the structural relationship between a fish body and its caudal fin on swimming performance, a simplified tuna-like model was developed, with the fish body undergoing undulating motion and the caudal fin performing combined heave and pitch, a comparison of single-fin (SF), disconnected-fin (DF) and connected-fin (CF) configurations with the findings of the present study that demonstrate that a disconnected structure significantly improves thrust and efficiency. Furthermore, simulations were conducted to explore the influence of distance between body and fin on performance.

A critical finding is that improper spacing at high Strouhal (St) numbers causes vortex-induced flow separation, reducing efficiency ass seen in Figure 2.27. The study validates its CFD model against established experimental data. It has been demonstrated that flow field analysis is a valuable tool for understanding the interactions between vortex bodies and fins. Notwithstanding the constraints imposed by two-dimensional (2D) imaging, the research the research highlights key mechanisms behind efficient fish locomotion (Zhao & Dou, 2019).

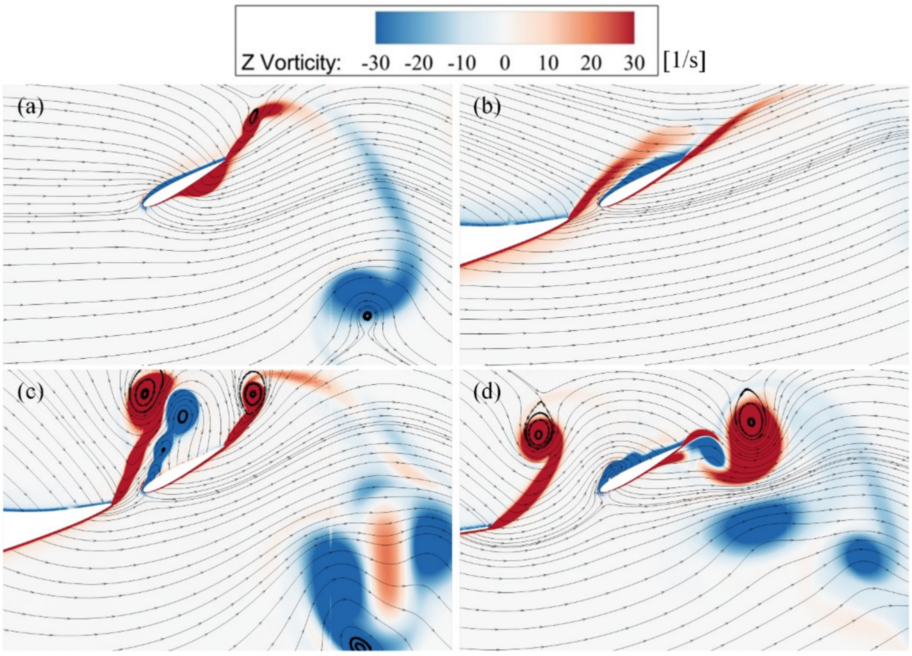

FIGURE 2.27: Instantaneous vorticity field superimposed with streamlines of the motion stage. (a) SF configuration ($St = 0{,}68$). (b) DF configuration ($St = 0{,}25$). (c) DF configuration ($St = 0{,}68$). (d) Case $d = 1{,}2c$ ($St = 0{,}68$), (Zhao & Dou, 2019).

Energy Extraction Performance Improvement of a Flapping Foil by the Use of Combined Foil

A study conducted a numerical investigation into the enhancement of the energy extraction performance of a flapping foil system through the introduction of a novel combined foil shape. The new design integrates the thick leading edge of a NACA0012 profile with the thin trailing edge of a NACA0006 (Figure 2.28), thereby creating a stepped geometry that influences flow behaviour.

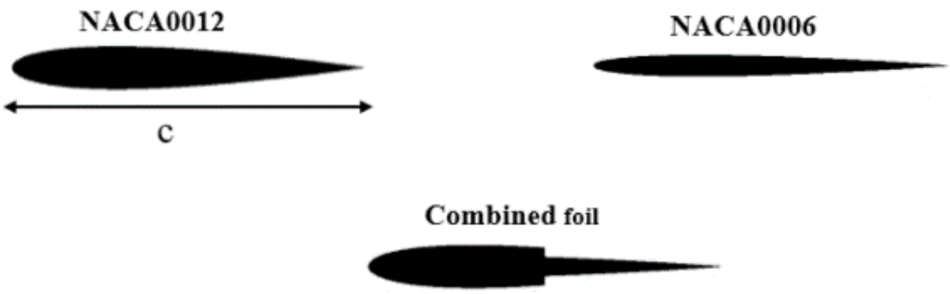

FIGURE 2.28: Fin profile geometry (Boudis et al., 2018).

CFD simulations were conducted utilising ANSYS Fluent 16 to address the unsteady, incompressible Navier-Stokes equations within a two-dimensional, dynamically meshed domain. A grid and time-step sensitivity study, has been conducted in order to confirm the reliability of the simulations, the results are shown in figure 2.29.

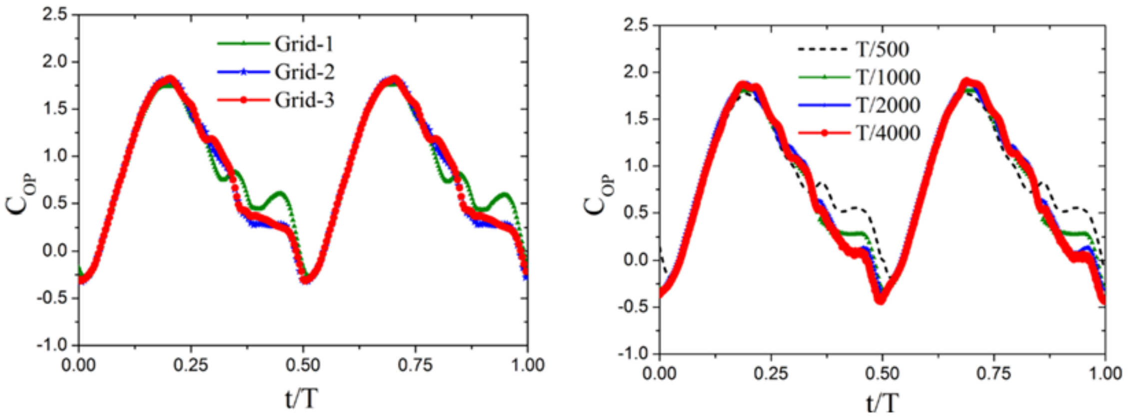

(A)

(B)

FIGURE 2.29: Instantaneous power coefficient over one flapping cycle computed using (A) different grids and (B) different time steps versus time over the flapping period (T) (Boudis et al., 2018).

The foil undergoes prescribed sinusoidal heaving and pitching motions, controlled by a UDF. The findings indicate that the combined foil exhibits superior performance in comparison to both baseline profiles, demonstrating a maximum efficiency enhancement of 30.6% in contrast to NACA0006 as seen in Figure 2.30.

The energy gain is primarily attributable to the heaving motion, with the pitching motion contributing negatively to the overall energy balance . The optimal performance is achieved when the step is placed at mid-chord, and at moderate Strouhal numbers and effective angles of attack.

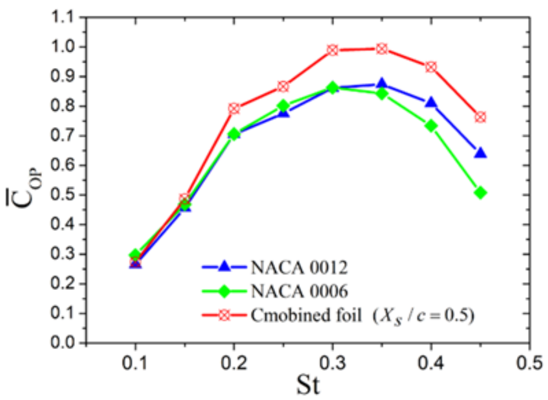

(A)

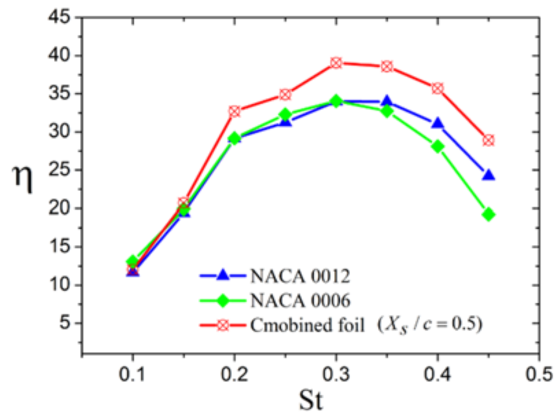

(B)

FIGURE 2.30: Comparison of (A) mean power extraction coefficient ($\overline{C}_{\mathrm{OP}}$) and (B) energy extraction efficiency (η) versus St at $\alpha = 30°$ (Boudis et al., 2018).

Oscillating foils of high propulsive efficiency

In this study, the propulsive performance of oscillating foils is investigated by experimentally varying three key parameters: the nondimensional heave amplitude ratio (h_o/c), the pitch amplitude (denoted either as α_o or $\alpha_{\max}$ depending on the motion type), and the phase offset (ψ) between the heaving and pitching motions. These variations allow for the assessment of their effects on the thrust coefficient (c_T) and provide insights into optimal kinematic configurations for efficient propulsion.

The different cases are presented in Table 2.1.

Case	h_o/c	α	ψ (deg)
1	0.75	$\alpha_{\max} = 21°$	75
2	0.75	$\alpha_{\max} = 17°$	105
3	0.25	$\alpha_o = 15°$	90
4	0.75	$\alpha_o = 5°$	90
5	0.75	$\alpha_o = 25°$	90
6	0.75	$\alpha_o = 20°$	90
7	0.75	$\alpha_o = 10°$	90
8	0.75	$\alpha_o = 30°$	90

TABLE 2.1: Experimentally measured parameters for each case. Adapted from J. M. Anderson et al., 1997.

The results presented in Figure 2.31 are analogous to those previously reported for screw-propeller data, where the advance coefficient – approximately the inverse of the Strouhal number – is varied, and the pitch-to-diameter ratio serves as a parameter to organise the data, without the need to impose additional constraints.

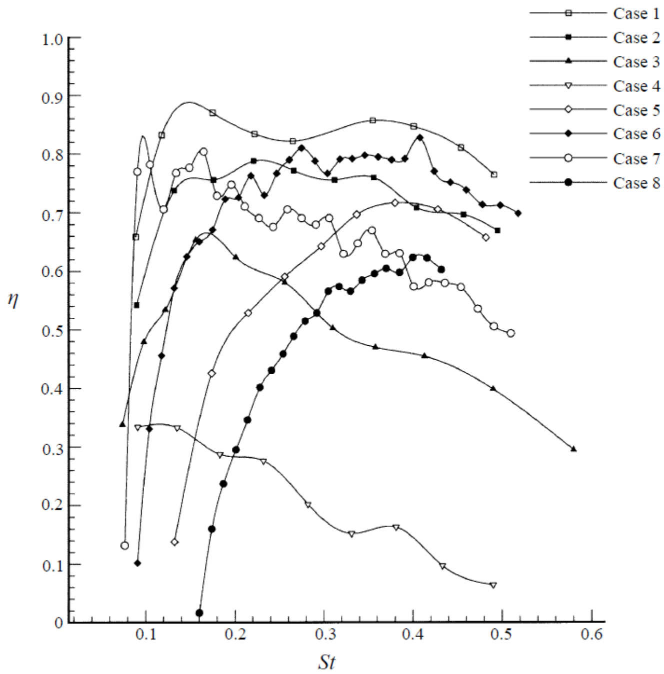

FIGURE 2.31: Experimentally measured efficiency as function of the Strouhal number (J. M. Anderson et al., 1997).

Hydrodynamic Performance of Swing-Type Flapping Hydrofoil

A two-dimensional unsteady CFD model was developed using ANSYS Fluent 2020. The Reynolds-Averaged Navier–Stokes (RANS) equations were solved with a realizable k–ε turbulence model. The study employed overlapping (Chimera) grids to ensure smooth domain interaction and fine resolution near the flapping hydrofoil and a grid convergence was established using five mesh densities (88,000 to 324,000 cells), and a timestep independence study confirmed accuracy at $\Delta t = 0.01$ s.

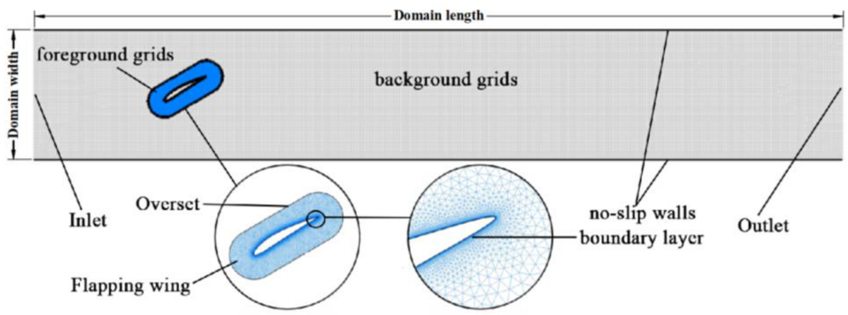

FIGURE 2.32: Fluid domain and mesh (Sun et al., 2024).

Model validation was conducted using benchmark experimental data for a NACA0012 foil undergoing sinusoidal plunging and pitching. The numerical results agreed within 5% of experimental thrust coefficients. Five NACA foil profiles with identical thickness (12% chord) but varying camber (0% to 8%) were simulated under frequencies ranging from 0.1 to 5 Hz.

At a frequency of 1 Hz, the NACA6412 foil with a 6% camber showed a 31.25% increase in peak instantaneous thrust coefficient compared to the symmetric NACA0012. Pumping efficiency reached its maximum at 8% camber for frequencies up to 2.5 Hz, while for frequencies above 2.5 Hz, the 6% camber configuration offered the highest gains, with improvements reaching 12.8%. Flow field visualizations revealed that cambered foils generated stronger and more asymmetric reverse Kármán vortex streets, contributing to enhanced thrust and sustained momentum in the wake. The velocity contours indicated that foils with greater curvature produced more coherent and extended high-speed jets, reducing vortex dissipation during downstream propagation and improving overall flow rate and energy transfer (Sun et al., 2024)..

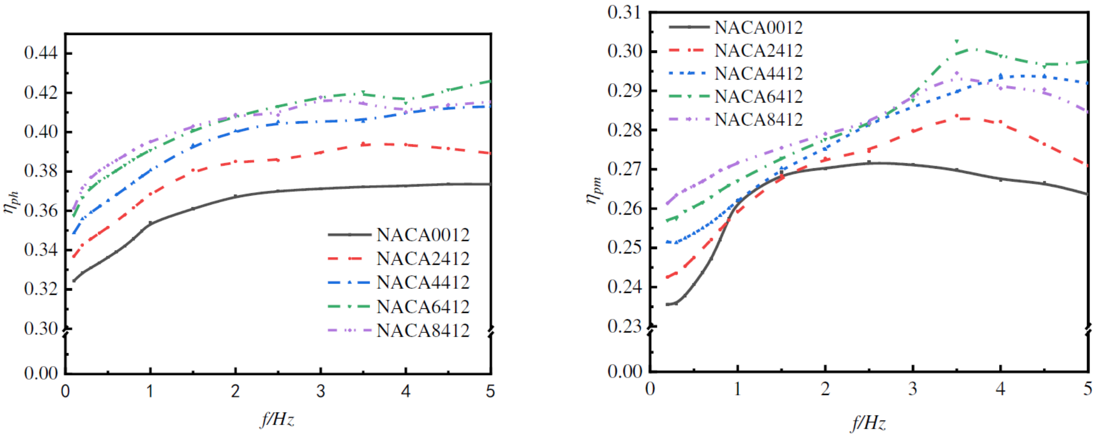

(A) (B)

FIGURE 2.33: Computational domain mesh and grid division (Sun et al., 2024).

Chapter 3

CFD Theoretical Framework

The study of the propulsion for the SABUVIS project was set through the development of a synthetic dataset, generated through CFD. This chapter aims to explain the fundaments of this technology for better understanding of its possibilities.

3.1 Computational Fluid Dynamics

The fundamental basis of this system are the numerical algorithms that have been developed to address the complex challenges posed by fluid flow. The following sub-chapter aims to explain the physics behind CFD, as well as the important equations it solves.

3.1.1 Governing equations of fluid flow and heat transfer

The CFD is rooted in the fundamental governing equations of fluid motion, namely the continuity, momentum, and energy equations. The aforementioned equations express the fundamental physical principles of fluid dynamics in mathematical form. Specifically, these principles represent the conservation of mass, the conservation of momentum (Newton's second law), and the conservation of energy – three universal laws that underlie all fluid behaviour. Therefore, CFD is the discipline that deals with finding numerical solutions to the governing equations. This involves replacing integral or differential terms with discrete algebraic approximations. These algebraic equations are then solved to obtain the numerical values of the flow field variables at specific points in space and/or time (J. D. Anderson, 1995), assuming a continuum description of fluid flow.

1. **Conservation of mass** (Continuity equation):

The following equation represents the unsteady, three-dimensional mass conservation or continuity equation at a point in a compressible fluid (Versteeg & Malalasekera, 2007b):

$$\frac{\partial \rho}{\partial t} + \nabla \cdot (\rho \cdot \mathbf{U}) = 0. \tag{3.1}$$

Here, ρ is the fluid density, ∇ the divergence operator and $\mathbf{U} = (u, v, w)$ is the velocity vector [m/s].

2. **Newton's Second Law of Motion** (Momentum equation):

Traditionally stated as:

$$\mathbf{F} = m \times \mathbf{a} \tag{3.2}$$

where $\mathbf{F}$ is force, m is mass, and $\mathbf{a}$ is acceleration. The momentum equation assumes a Newtonian fluid, where stress is linearly proportional to the rate of strain. For a continuous medium like a fluid, this becomes a force *per unit volume* formulation $\sum \mathbf{F} = \rho \frac{D\mathbf{U}}{Dt}$, where $\frac{D}{Dt}$ is the material derivative,

$$\frac{D}{Dt} = \frac{\partial}{\partial t} + \mathbf{U} \cdot \nabla,$$

which accounts for both local ($\frac{\partial}{\partial t}$) and convective ($\mathbf{U} \cdot \nabla$) changes following a fluid particle. The forces acting on a fluid element include surface forces, due to pressure and viscous stresses such as pressure: $-\nabla p$, ∇ being the gradient operator, and viscous stresses: $\nabla \cdot \boldsymbol{\tau}$, where $\boldsymbol{\tau}$ is the viscous stress tensor, and body forces, such as gravity, expressed as $\rho \mathbf{f}$. Thus, the momentum becomes:

$$\rho \frac{D\mathbf{U}}{Dt} = -\nabla p + \nabla \cdot \boldsymbol{\tau} + \rho \mathbf{f} \tag{3.3}$$

as the vector form of the Navier-Stokes momentum equation (Fox et al., 2011), which when converted to Cartesian coordinates, results in the expansion into three scalar components:

$$\begin{cases} \rho \frac{Du}{Dt} = \frac{\partial}{\partial x}(-p + \tau_{xx}) + \frac{\partial \tau_{yx}}{\partial y} + \frac{\partial \tau_{zx}}{\partial z} + S_{Mx} \\ \rho \frac{Dv}{Dt} = \frac{\partial \tau_{xy}}{\partial x} + \frac{\partial}{\partial y}(-p + \tau_{yy}) + \frac{\partial \tau_{zy}}{\partial z} + S_{My} \\ \rho \frac{Dw}{Dt} = \frac{\partial \tau_{xz}}{\partial x} + \frac{\partial \tau_{yz}}{\partial y} + \frac{\partial}{\partial z}(-p + \tau_{zz}) + S_{Mz} \end{cases} \tag{3.4}$$

Here, u, v, w are the velocity components in the x-, y-, and z-directions, respectively. Here, p is the pressure [Pa], τ_{ij} are the components of the viscous stress tensor with $\tau_{xx}, \tau_{yy}, \tau_{zz}$ as normal stresses and $\tau_{xy}, \tau_{yx}, \tau_{yz}, \tau_{zy}, \tau_{zx}, \tau_{xz}$ as shear stresses. S_{Mx}, S_{My}, S_{Mz} are source terms representing external body forces (e.g., gravity).

3. **Conservation of energy** (Thermal energy equation):

   Often expressed as the First Law of Thermodynamics: energy cannot be created or destroyed, only transformed (J. D. Anderson, 1995):

$$\frac{\partial(\rho E)}{\partial t} + \nabla \cdot [(\rho E + p)\mathbf{U}] = \nabla \cdot (k \nabla T) + \nabla \cdot (\mathbf{U} \cdot \boldsymbol{\tau}) + \rho \dot{q} + \rho \mathbf{f} \cdot \mathbf{U} \tag{3.5}$$

   Here, E is the total specific energy given by:

$$E = e + \frac{1}{2}|\mathbf{U}|^2$$

   where e is the internal energy per unit mass, and $\frac{1}{2}|\mathbf{U}|^2$ is the kinetic energy. The term $k\nabla T$, represents thermal conduction, ∇T being the temperature gradient and k the thermal conductivity. The term $\nabla \cdot (\boldsymbol{\tau} \cdot \mathbf{U})$ represents the rate of viscous work done on a fluid element and accounts for the conversion of kinetic energy into internal energy due to viscous dissipation, $\rho \dot{q}$ is the volumetric heat source term, and $\rho \mathbf{f} \cdot \mathbf{U}$ accounts for work done by body forces.

Derivation of the General Transport Equation

The general transport equation is a fundamental mathematical representation used in fluid dynamics to describe the conservation of scalar quantities such as mass, momentum, energy and other variables. It provides a framework for analysing how a scalar property changes within a control volume due to various physical processes, including convection, diffusion, and source terms.

The transport equation is derived from the principle of conservation, which states that the total change of within a control volume must be equal to the sum of its rate of change due to different physical processes. The integral form of the transport equation can be expressed as (Versteeg & Malalasekera, 2007a):

$$\frac{\partial}{\partial t} \int_V \rho \phi, dV + \oint_A \rho \phi \mathbf{U} \cdot d\mathbf{A} = \oint_A \Gamma_\phi \nabla \phi \cdot d\mathbf{A} + \int_V S_\phi, dV, \tag{3.6}$$

where:

- ϕ is the transported quantity (e.g., temperature, velocity, species concentration),
- $d\mathbf{A}$ is the outward-oriented surface element of the control volume,
- Γ_ϕ is the diffusion coefficient,
- $\nabla\phi$ is the gradient of the transported quantity,
- S_ϕ is the source term accounting for generation or consumption of ϕ inside the volume V.

Explanation of Terms

- Unsteady (Transient) Term

$$\frac{\partial}{\partial t}\int_V \rho\phi, dV \tag{3.7}$$

This term represents the rate of change of within the control volume over time. If the property is not changing with time, this term vanishes (steady-state condition).

- Convective Term:

$$\oint_A \rho\phi\mathbf{U}\cdot d\mathbf{A} \tag{3.8}$$

This term accounts for the net flux of due to advection (transport by fluid motion) across the control surface. It represents the inflow and outflow of due to bulk movement of the fluid.

- Diffusive Term

$$\oint_A \Gamma_\phi\nabla\phi\cdot d\mathbf{A} \tag{3.9}$$

This term represents the diffusive transport of due to molecular or turbulent diffusion. The coefficient characterizes the diffusivity of the property in the medium.

- Source Term

$$\int_V S_\phi, dV \tag{3.10}$$

This term represents the volumetric sources or sinks of within the control volume. It accounts for any internal generation (e.g., heat generation, chemical reactions) or consumption of the transported quantity (e.g., energy, species, momentum).

Differential Form of the Transport Equation

Applying the divergence theorem to convert surface integrals into volume integrals and assuming the control volume is arbitrarily small, we obtain the differential form:

$$\frac{\partial}{\partial t}(\rho\phi) + \nabla \cdot (\rho\phi\mathbf{U}) = \nabla \cdot (\Gamma_\phi \nabla\phi) + S_\phi. \tag{3.11}$$

This equation states that the local rate of change plus its convective transport equals its diffusive transport and sources.

Reynolds Number

The Reynolds number (Re) is a dimensionless quantity employed to predict flow patterns in various fluid flow situations. It is defined as the ratio of inertial forces to viscous forces, and its determination is of crucial importance in ascertaining whether a flow will be laminar or turbulent.

The Reynolds number is given by the formula:

$$Re = \frac{\rho U L}{\mu} = \frac{U L}{\nu} \tag{3.12}$$

where:

- U is the characteristic velocity of the flow [m/s],
- L is the characteristic length [m],
- μ is the dynamic viscosity [$\mathrm{Pa \cdot s}$],
- ν is the kinematic viscosity [$\mathrm{m^2/s}$] of the fluid:

$$\nu = \frac{\mu}{\rho} \tag{3.13}$$

For values of $Re < 2000$, the flow is generally laminar, characterized by smooth, orderly motion with minimal mixing between adjacent fluid layers. When the Reynolds number falls within the range $2000 < Re < 4000$, the flow enters a transitional regime, where it becomes increasingly sensitive to perturbations and may exhibit intermittent behaviour between laminar and turbulent states. For $Re > 4000$, the flow is considered turbulent, displaying chaotic fluctuations, high mixing, and complex velocity profiles.

In CFD simulations, the Reynolds number plays a crucial role in determining the appropriate turbulence modelling strategy. As discussed in Chapter 4, models such as k-ϵ, k-ω, Large Eddy Simulation (LES), and Direct Numerical Simulation (DNS) are employed depending on the expected flow characteristics. The choice of turbulence model directly affects mesh resolution and time-stepping requirements, as well as the ability to accurately capture boundary layer behaviour, flow separation, and reattachment. Consequently, the Reynolds number informs both the formulation of the simulation and the validation of its underlying assumptions.

Based on the maximum expected flow conditions—namely, a velocity of 2 m/s, a characteristic length (fin chord) of 0.5 m, a saltwater density of 1025 kg/m^3, and a dynamic viscosity of 1.08×10^{-3} Pa $\cdot$ s—the Reynolds number can be estimated using the standard relation for external flow (Equation 3.12). Substituting these values into the equation yields a maximum expected Reynolds number of approximately 9.59×10^5. This high value places the flow well within the turbulent regime, reinforcing the need for appropriate turbulence modelling in subsequent computational simulations.

Courant Number

The Courant number (Co) is also a dimensionless quantity, that arises from the Courant–Friedrichs–Lewy (CFL) condition, which is essential for ensuring the stability of numerical schemes in time-dependent CFD simulations. It is defined as:

$$Co = \frac{U\Delta t}{\Delta x} \tag{3.14}$$

where:

- Δt is the time step size [s],
- Δx is the characteristic cell length (grid spacing) [m].

The Courant number plays a critical role in governing the numerical stability of a simulation. In the case of explicit solvers, where the solution at the next time step depends solely on known values from the current time step, the Courant number typically must satisfy the condition $Co \leq 1$ to ensure stability. In contrast, implicit solvers—where the next time step depends on values that are themselves being solved for—can often tolerate higher Courant numbers. However, excessively large values, even in implicit schemes, may still compromise the accuracy of the solution. Therefore, the Courant number directly influences the selection of the time step Δt, which must be chosen in relation to the mesh resolution and the expected velocity field to maintain both stability and solution fidelity.

For a saltwater flow over a fin, and considering an implicit solver:

- Velocity: $U = 2\,\mathrm{m/s}$
- Cell size (approximately): $\Delta x = 0.00025\,\mathrm{m}$ (0.25 mm)
- Courant number target: $Co = 200$

Solving for the maximum stable time step:

$$\Delta t = \frac{Co \cdot \Delta x}{U} = \frac{0.5 \cdot 0.005}{2} = 2.5 \times 10^{-2}\,\mathrm{s} \tag{3.15}$$

Thus, for stability with an implicit solver and a 0.25 mm mesh resolution, the time step should not exceed 25 ms.

y^+ Definition and Physical Meaning

The dimensionless wall distance, denoted as y^+, is a key parameter in the simulation of turbulent boundary layers in CFD. It is defined as:

$$y^+ = \frac{U_{\text{fric}} \cdot y}{\nu} \tag{3.16}$$

where:

- y is the distance from the wall to the center of the first computational cell [m],
- U_{fric} is the friction velocity:
$$U_{\text{fric}} = \sqrt{\frac{\tau_{\text{wall}}}{\rho}} \tag{3.17}$$
  with:
  - τ_{wall} as the wall shear stress [Pa],

Region	Approximate y^+	Flow Characteristics
Viscous sublayer	$y^+ < 5$	Linear velocity profile, laminar-like
Buffer layer	$5 < y^+ < 30$	Transitional behavior
Log-law region	$y^+ > 30$	Fully turbulent, logarithmic profile

The value of y^+ effectively describes the location of the first mesh cell relative to the structure of the turbulent boundary layer in non-dimensional viscous units.

The boundary layer near a wall is typically divided into several regions, each governed by different physics. The recommended y^+ values for placing the first mesh cell depend on the turbulence model and wall treatment method:

The calculations for the y^+ can be seen in Appendix A. To achieve $y^+ \approx 1$, the first cell adjacent to the wall must be approximately $12.32\,\mu$m high.

Once this values are set, it is time to move on to the CFD component. In order to reach public accessibility of this computational possibilities, contemporary commercial CFD packages have been equipped with advanced graphical interfaces for the definition of input parameters and the visualisation of output data. The system comprises three distinct components: firstly, a pre-processor, responsible for geometry creation and mesh generation; secondly, a solver, which performs the numerical computations; and thirdly, a post-processor, used for interpreting and analysing the simulation results.

3.1.2 Pre-Processor

Geometry Creation

To define a geometry to be analysed, several initial studies were developed to simulate the behaviour of a 2 dimensional (2D) fin. The requirements were for the fin to not exceed the length of the model as a whole, and to allow the possibility of two fins in line, for the study of a 4 propulsion system, similar to the leatherback sea turtle (*dermochelys coriacea*). A capability of achieving average speeds of 3.2 km/h, corresponding to 0,88(9) m/s with peaks of approximately 1,61 m/s in different legs of the studied journey was studied previously (Hughes et al., 1998). However, the majority of the study focuses on a single caudal fin.

Like in many other solutions science has found, nature has been the answer. Looking at the profile from the fin of a turtle, dolfin or other large fish like a tuna, as seen in figure 3.1, where it is possible to observe the similarity between the caudal fin and the profile from NACA airfoils.

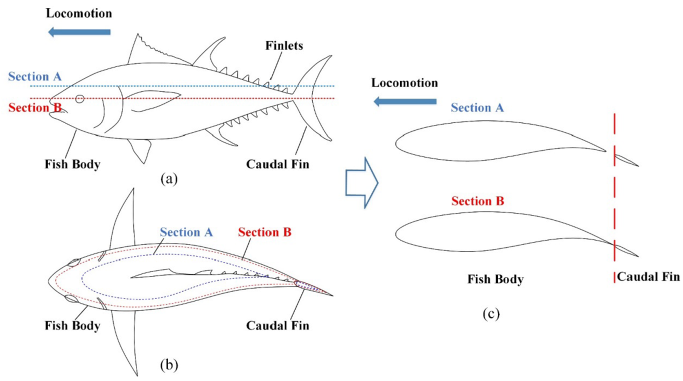

FIGURE 3.1: Schematic of a tuna model: (a) side view; (b) top view; (c) the 2D simplified fish models (Zhao & Dou, 2019).

Mesh Generation

The arrangement of discrete points throughout the computational domain is termed the *grid*. The construction of an appropriate grid for simulating flow over or through a given geometry is a non-trivial and critical task. This process, known as *mesh generation*, plays a crucial role in CFD analysis, as it divides the geometry of the flow domain into small, finite volumes or elements (J. D. Anderson, 1995).

The selection of grid type, quality, and resolution can have a substantial impact on the accuracy, stability, and efficiency of the numerical solution. Consequently, grid generation has evolved into a specialised and essential area of research and development within the field of CFD. For simple "perfect" objects such as a rectangular, choosing a grid can be a simple process, however, when applying the same principle to an object like an airfoil, it is noteworthy that a proportion of computational grid points may be situated within the its interior, thereby placing them entirely outside the fluid domain as seen in Figure 3.2.

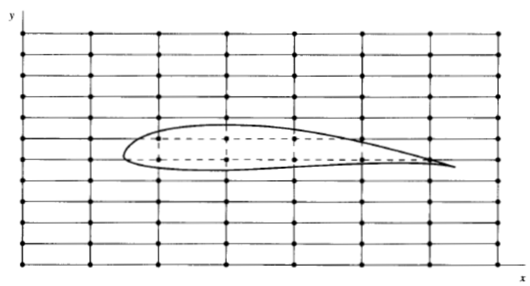

FIGURE 3.2: An airfoil in a purely rectangular grid (J. D. Anderson, 1995).

Moreover, in numerous instances, the resolution of the grid proves inadequate for the precise placement of points on the airfoil surface. This poses a significant issue, as the airfoil surface represents a critical boundary condition that directly influences the computed flow field (J. D. Anderson, 1995). In order to ensure the accuracy of the simulation, it is essential that the surface is adequately resolved and explicitly represented in the numerical scheme. A structured mesh plays a crucial role in CFD analysis and when not achieved, it is possible the code fails to run due to an unstructured and poorly resolved mesh. However, an unstructured mesh can also be applied for complex geometries, allowing for a more refined mesh only in the areas of interest, as seen in figure 3.3a. On the other hand, when possible, a structured mesh should capture all elements of the object in study and make it easier to understand the quality of the results as well as their reliability. Figure 3.3b displays an example of a structured mesh over an airfoil.

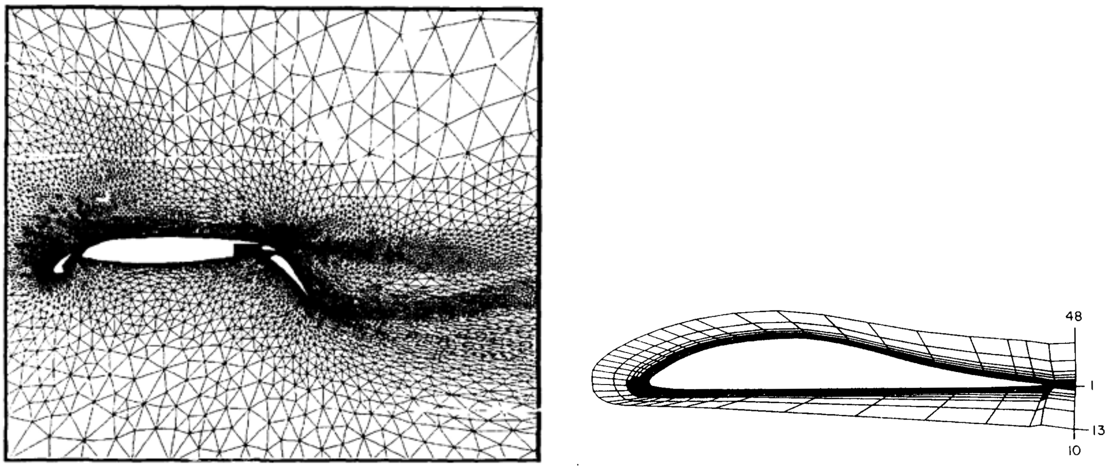

(A) (B)

FIGURE 3.3: Mesh examples where (A) represents a global view of adaptively generated mesh over a Four-Element Airfoil (Venkatakrishnan & Mavriplis, 1993) and (B) a small, detailed section of the boundary-fitted grid of an airfoil (J. D. Anderson, 1995).

3.1.3 Solver

Methods

CFD primarily utilizes three numerical approaches for solving partial differential equations (PDEs): the Finite Difference Method (FDM) that includes a special finite difference formulation called the Finite Volume Method (FVM) (Jeong & Seong, 2013), the Finite Element Method (FEM) and spectral methods (Versteeg & Malalasekera, 2007b).

A specialized finite difference approach lies at the core of several leading commercial CFD software packages, including *CFX/ANSYS*, *FLUENT*, *PHOENICS*, and *STAR-CD*. The numerical algorithm these tools implement generally follows a structured sequence of steps:

- Integration of the governing fluid flow equations over all finite control volumes within the computational domain;
- Discretization, wherein the integral equations are transformed into a corresponding system of algebraic equations;
- Iterative solution of the resulting algebraic system.

The FVM is a numerical approach that has been extensively employed for the solution of PDEs that represent conservation laws in fluid dynamics and related fields. In this method, the computational domain is initially discretised into a finite number of non-overlapping control volumes, otherwise referred to as cells. In contrast to FDM and FEM, which approximate derivatives at discrete points or over element shapes, respectively, the FVM integrates the governing equations over each control volume. This directly enforces the conservation of mass, momentum, and energy within each finite region. This integral formulation naturally converts the continuous PDE into a set of discrete algebraic equations. The resolution of this system provides approximate values of the field variables (e.g. velocity, pressure, and temperature) at specific locations within the domain, typically at the centroid or nodes of each control volume (Moukalled et al., 2016).

To accurately capture these phenomena, CFD codes incorporate discretization schemes that handle each transport mechanism appropriately. Given the complexity and inherent nonlinearity of the underlying physical processes, these systems are typically solved using iterative numerical methods. Among the most widely adopted solution procedures are the *Tri-Diagonal Matrix Algorithm (TDMA)* for line-by-line equation solving and the *SIMPLE algorithm* for maintaining consistency between pressure and velocity fields, the *Gauss–Seidel point iteration*, *multigrid acceleration*, and *conjugate gradient methods*, to enhance convergence and computational efficiency (Jeong & Seong, 2013).

ANSYS Fluent allows for both segregated and coupled solution strategies. In this study, the COUPLED, an implicit solver was employed, wherein the pressure and momentum equations are solved in a fully coupled manner. This method is known for enhancing robustness and convergence in simulations involving strong pressure–velocity coupling or transient flows with moving boundaries (Fluent, 2009).

Turbulence Modeling Methods

Unsteady Flow Physics

Oscillating foils at moderate or high Reynolds numbers exhibit dynamic stall and form reverse von Kármán vortex streets that contribute to thrust generation. A von Kármán vortex street is a repeating pattern of vortices that forms when fluid flows past a bluff body. The vortices are shed alternately from each side, producing a staggered, oscillating wake (Kármán, 1911). Vorticity is shed from the leading and trailing edges each half-cycle, and leading-edge vortex (LEV) may form and burst during rapid pitch cycles. Capturing these features is critical for accurate lift and thrust predictions.

Transition Effects

At $Re \sim 10^4$–10^5, laminar-to-turbulent transition plays a major role. Laminar separation bubbles and intermittent boundary layers are common. Standard Reynolds-Averaged Navier–Stokes (RANS) models, assuming fully turbulent flow, often fail to predict the onset of separation. Transition-aware RANS or scale-resolving methods more accurately capture vortex dynamics induced by laminar separation (Fluent, 2009).

RANS models average turbulence, missing unsteady structures. Large Eddy Simulation (LES) and hybrid RANS-LES, usually Detached Eddy Simulation (DES) resolve large eddies, enabling accurate modelling of vortex shedding and wake structures. However, these methods are computationally more expensive, requiring finer meshes and smaller time steps (Fluent, 2009).

Reynolds-Averaged Models

RANS models are computationally efficient and can predict mean loads reasonably well when calibrated.

Spalart–Allmaras

The Spalart-Allmaras (SA) turbulence model is widely regarded for its computational efficiency and ease of implementation. Due to its single-equation eddy-viscosity formulation, however, the SA model cannot resolve instantaneous vortex structures and often underperforms in cases involving high-amplitude motion or transitional flows. SA-URANS with a transition model can reproduce the 2P+2S vortex pattern similar to those in 3.4. However, plain SA often fails to capture secondary vortices.

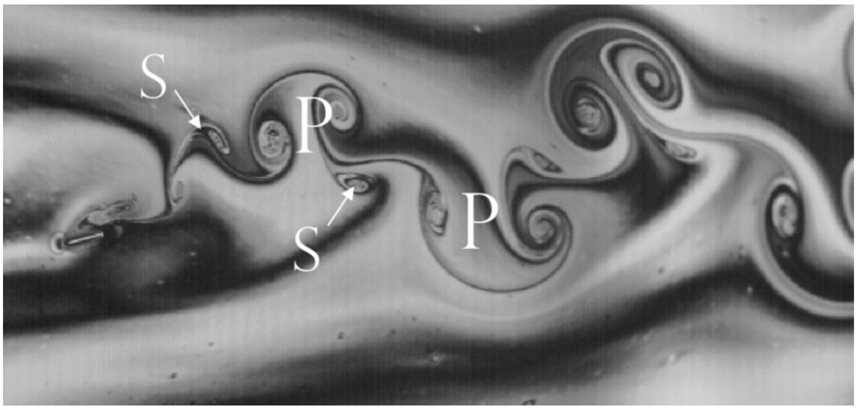

FIGURE 3.4: S and P vortex patterns (Muijres et al., 2005)

k–ω Shear Stress Transport (SST)

A two-equation RANS formulation that blends k–ω near walls with k–ε in the free stream, improves the prediction of flow separation under adverse pressure gradients. In unsteady oscillating foil flows, the SST model captures the onset of dynamic stall more accurately than algebraic or simpler turbulence models, and often predicts mean loads with higher fidelity. Despite this, like SA, the shear stress transport (SST) model remains limited by the Reynolds-averaged formulation and thus cannot resolve detailed vortex shedding structures (Fluent, 2009). This method was chosen for this work because it is computationally efficient yet still maintains a good level of accuracy (Mishra, 2024).

Large Eddy Simulation (LES)

LES resolves all large-scale turbulent eddies while modelling only the smallest subgrid-scale motions. This capability enables LES to directly capture transient phenomena such as vortex shedding, leading-edge vortex formation, and unsteady separation. In applications involving pitching or flapping foils, LES has been shown to accurately reproduce vorticity patterns, stall vortices, and wake instabilities observed in experimental studies. The primary drawback of LES lies in its substantial computational cost (Ghasemnezhad & Roohi, 2024).

Detached Eddy Simulation (DES)

DES provides a hybrid modelling approach that applies RANS in attached boundary layers and transitions to LES in separated or unsteady regions. DES aims to capture the large-scale unsteady structures with less computational demand than full LES. When implemented properly, DES can resolve vortex shedding and wake dynamics in flapping foils with significantly greater fidelity than URANS. A study employed three-dimensional numerical simulations using the Delayed Detached-Eddy Simulation (DDES) approach to evaluate the performance and wake recovery of hydro kinetic flapping-foil turbines (Villeneuve et al., 2021) .

3.1.4 Post-Processor

Once the solver is finished, it is necessary to present the results in a manner that fully displays all the fundamental aspects discovered during the computing part. This is where CFD post-processing enters. The post processing part of CFD consists in a series of some computer graphic "techniques" that are frequently employed in the presentation of data. It was described as a set of tools that allows the visualization of the results in order to actually understand what is happening with the drag and lift forces, velocity distribution and pressure points (Toet, 2019). Previously, it had been divided in these graphic "techniques" in 6 categories (J. D. Anderson, 1995):

- xy Plots

  Frequently employed to illustrate data such as the pressure coefficient in relation to the non-dimensional chord wise distance across various span wise stations.

- Contour Plots

  Graphical representations of lines of constant value for a given property, with the line spacing indicating the rate of spatial change. This approach provides a clear, global view of flow behaviour in a single image.

- Vector and Streamline Plots

  A representation of a vector quantity at specific grid points. Each vector originates at a grid point and thus illustrates both the magnitude and direction of the flow, effective in visualizing flow patterns and directional behaviour across the domain.

- Scatter Plots

  A scatter plot is a graphical representation of data where symbols (e.g. circles or squares) are placed at specific grid points to illustrate scalar quantities such as pressure or temperature

- Mesh Plots

  Mesh plots in CFD visually represent the computational grid used for simulations, showing how the domain is divided into discrete elements like the ones seen in figure 3.3.

- Composite plots

  A combination of different plots all in one to display the results in a single plot.

Different software applications offer a variety of pre-defined post-processing tools that facilitate expeditious analysis of results.

Chapter 4

Methodology

The ultimate output of a CFD simulation is therefore a set of numerical data rather than a closed-form analytical expression. Nonetheless, the objective of the majority of engineering analyses, whether analytical or numerical, is to attain a quantitative description of the physical phenomenon under investigation; that is to say, to obtain a numerical result (J. D. Anderson, 1995).

The simulation is, thus, divided into six distinct steps: the proposed movements, the design of the fin profile; the mesh independence study; the UDF (for specific movements or changing variables); the model solver (especially for turbulence); and the simulation parameters, such as time-steps and specific records. It is evident that certain elements of this project are operating in a concurrent manner with other components, such as the design and the mesh independence study.

4.1 Proposed Movements

Two movements for the fins were applied and studied:

- **Classical Sinusoidal Movement (CSM)** - A perfect sine wave was introduced as the motion for the fins, considered a simplified approximation of common fish;
- **Alternative Turtle Movement (ATM)** - For a motion with higher impact in the descend motion and lower in the ascending, considered initially as a more realistic approximation to the motion of a larger fish, reptile like a turtle or similar sea creatures. This movement was achieved using a Fourier series approximation.

These movements are introduced through a UDF, written in C language, that ANSYS compiles in a library and applies to the designated component. By using this method, it is also possible to vary the frequency and amplitude of the oscillating movement according to time, in order to create a simulation of a speed varying course.

4.2 Fin Profile Design

In order to establish a standardised cut, a comprehensive research study was conducted on the aerodynamics of airfoils and hydrofoils. This research revealed that the NACA 0012 model had a sufficient amount of data and studies to support its use in marine applications. The utilisation of the air foil tools database facilitated the importation of the points necessary to create a geometry representation in ANSYS to the software, having imported a total of 131 points, with the leading edge positioned at the origin point (0, 0, 0).

The creation of a surface for the fin, in conjunction with the generation of an environment that simulates a water tank (Figure 4.1) and provides adequate space for full development of movement, enabled the execution of preliminary simulations.

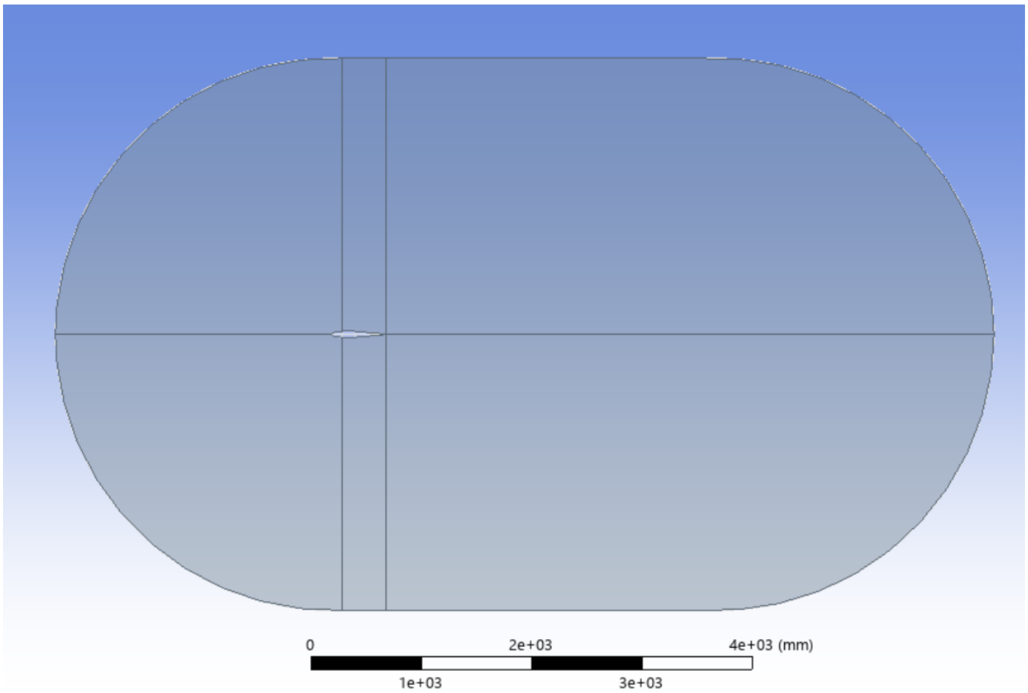

FIGURE 4.1: Water tank domain used for simulations

The parametrisation of this fin was a complex procedure due to being based on imported dots (Tools, 2025).

Consequently, a symmetrical profile of equivalent length and width was created to overcome this problem, exhibiting full symmetry over the $x0z$ plane.Figure 4.2b displays the different profiles. As it is possible to see, both profiles are nearly identical, as they are supposed to be, considering the interest is to parametrize a profile to allow quick changes for different studies.

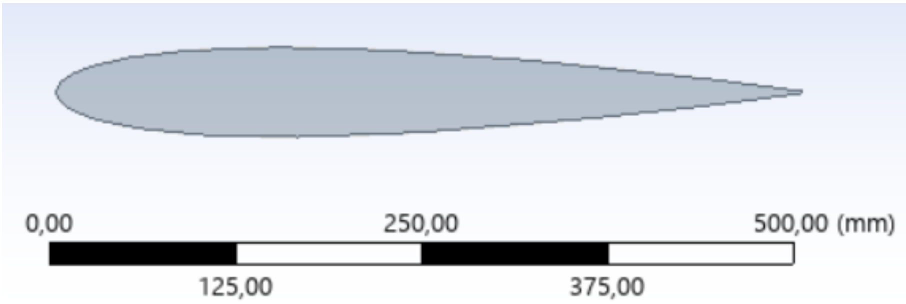

(A) Imported NACA0012 Geometry

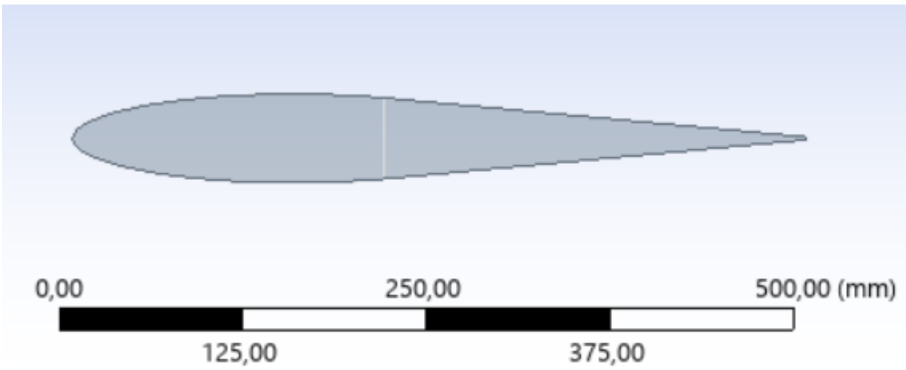

(B) Parametrized Geometry

FIGURE 4.2: Fin geometry preparation for CFD analysis

A new simulation was run using the same movement to compare both profiles and as it is possible to observe in the graphics from Figure 4.3 the velocities obtained by the parametrized profile and the NACA 0012 airfoil are very similar, with an error of 3,17% and 3,22% for the CSM and ATM respectively. From this point on, the parametrized profile was used for all simulations.

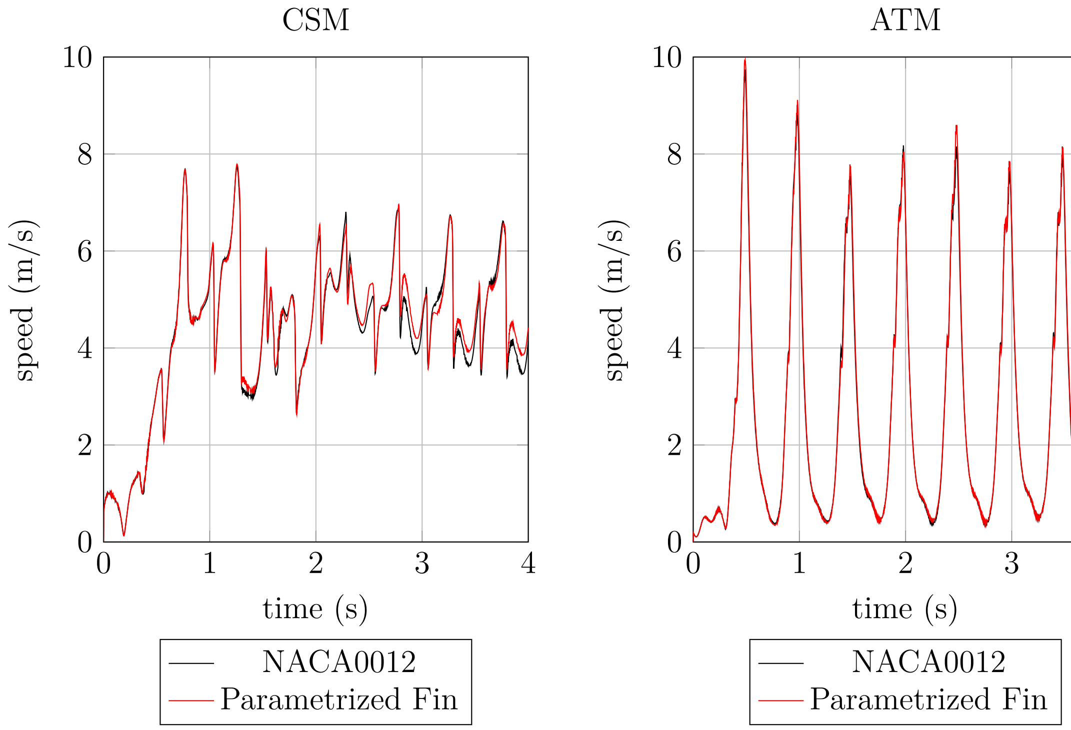

FIGURE 4.3: Comparison between different profiles and movements using the same size and amplitude for the fin

Once the profile was achieved to initiate the mesh process, it was necessary to comprehend the repercussions for the subsequent study. In this section, the work was divided into distinct phases. Following the parametrization of the fin, a preliminary study was conducted on the Reynolds and Froude numbers, as well as the Courant number. To make sure the time step found was sufficient a smaller y^+ of about 2.94 μm was used, as seen in figure 4.4.

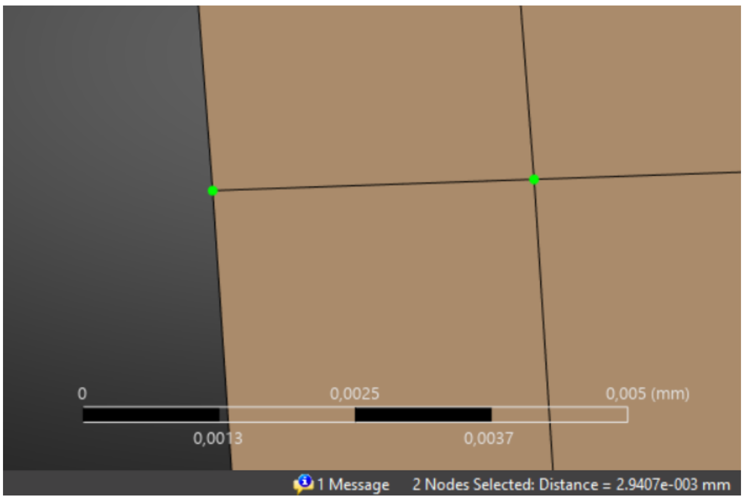

FIGURE 4.4: y+ obtained for profile

4.3 Mesh Independence Study

The mesh independence study is of paramount importance in CFD to ensure simulation accuracy and physical realism. There is a point in which additional mesh refinement does not have a significant impact on results, thereby validating the model and eliminating numerical artifacts. Furthermore, the study facilitates the optimisation of computational resources by determining said point.

The process entails the generation of multiple meshes (ranging from coarse to fine, minimum three levels of mesh), the execution of simulations under consistent settings, and the comparison of key outputs (e.g., lift and drag). Should the results of the simulation converge as the mesh is refined, the simulation is considered mesh-independent. The optimal mesh is one that balances accuracy with computational cost. A similar procedure was accomplished in a study from Prabu et al., 2024 and his results can be seen in Annex II.1.

A NASA grid convergence study also provided benchmark solutions for turbulent flow around the NACA 0012 airfoil, highlighting the significance of grid resolution in achieving accurate results (Slotnick et al., 2015).

Parametrized Fin Profile

With the main focus of this dissertation being the velocities changes between different profiles and movement, a set of profiles was defined in order to run as many simulations as possible, starting with the biggest lenght, movement amplitude and frequency to the smallest possibilities. In the course of the mesh independence study, several meshes were analysed, starting with 544 400 elements as a baseline (seen that it was considered a good starting point based on the look of the mesh in general) and running other simulations with a $\sqrt{2}$ factor to analyse its evolution for both higher and lower number of elements.

The mesh was altered changing only the number of elements surrounding the fin, not the number of elements from the fin to the border of the tank, maintaining the y+ number. This allows the mesh criteria to limit itself only to the fin, not to the fluid around it.

Despite analysing a smaller fin perimeter with each length reduction, the number of elements does not change, meaning the quality of the simulation will increase the smaller the size of the fin.

Figure 4.5 shows the different values for the area-weighted average velocity of the fluid at a 15 cm point after the end of the fin.

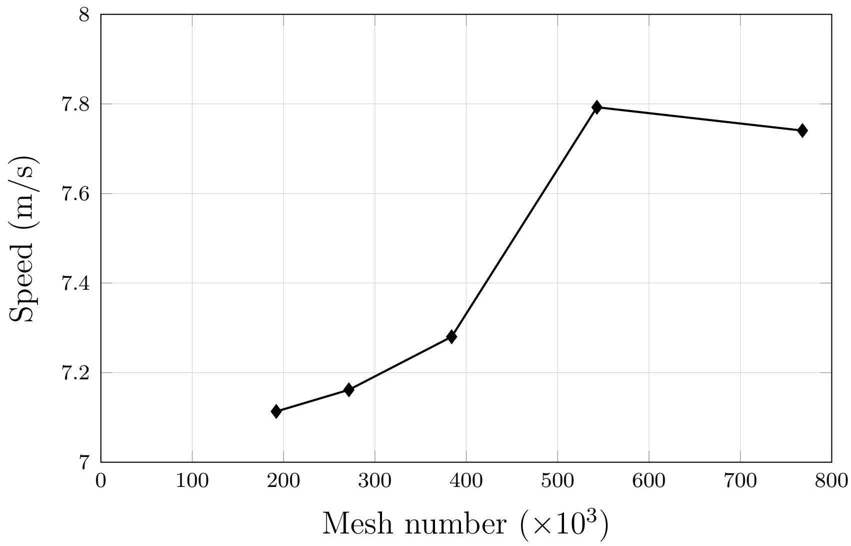

FIGURE 4.5: Mesh Independence Study considering max fluid velocity - Parametrized Fin

After this process, it was considered that a mesh of 544,400 elements was sufficient and a good compromise between the computational cost to run simulations and the accuracy of the results. A close-up from the tail of the fin is seen in Figure 4.6.

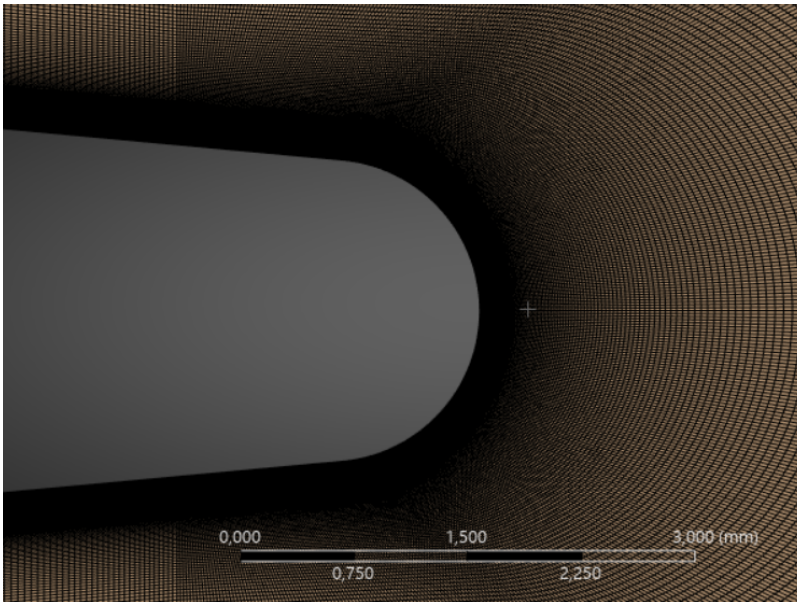

FIGURE 4.6: Detailed mesh of the tail of the fin profile

The fluid domain containing the mesh is seen in Figure 4.7, similar to figure 3.3b.

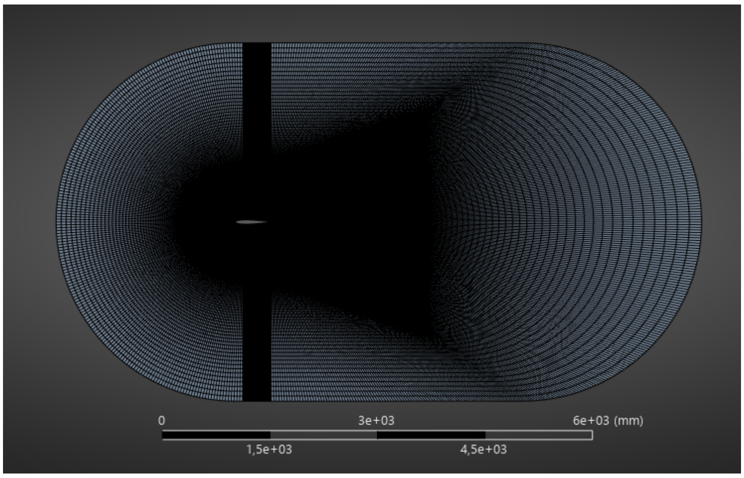

FIGURE 4.7: Geometry domain preparation for CFD analysis

4.4 Computational Domain and Mesh Motion

The computational domain consists of a two-dimensional fluid region with salt water. This is modelled as an incompressible Newtonian fluid with a constant density of 1025 kg/m^3. Dynamic mesh techniques were employed to capture the motion of the deforming boundaries associated with the flapping fin. The dynamic mesh methodology combines three motion strategies for the mesh: smoothing, layering, and remeshing. Smoothing adjusts the interior node positions based on a diffusion-based algorithm to prevent mesh distortion. Layering adds or removes cells adjacent to the moving boundaries to the moving boundaries when necessary, and remeshing regenerates the mesh locally if cell quality deteriorates beyond acceptable thresholds.

To prescribe the motion of the fin and ensure accurate boundary deformation, a UDF, whose codes can be seen in Appendices C and B, was implemented. In this study, the UDF defined the time-dependent angular displacement of the fin and was linked to dynamic mesh zones in order to impose periodic flapping kinematics. This approach provides the flexibility required to simulate complex motion profiles that cannot be handled by standard built-in functions, such as a Fourier approximation for the ATM.

4.5 Solver Methods

In order to achieve an equilibrium between accuracy and computer cost, the solver characteristics were the following:

TABLE 4.1: Solver setup.

Turbulence model	**k-ω SST**
Water density	1024 kg/m^3
Scheme	Implicit
Pressure velocity coupling	COUPLED
Momentum	2nd order upwind
Pressure	2nd order
Turbulent kinetic energy (k)	2nd order upwind
Specific dissipation rate (ω)	2nd order upwind
Gradient	Least Squares Cell Based
Transient formulation	First order implicit

Second-order schemes are generally considered a satisfactory balance between computational cost and accuracy. The utilisation of first-order methods remains a viable approach in the context of simulations characterised by low-resolution meshes, elevated numerical stiffness, or a prioritisation of robustness over fidelity. An explanation on the first and second order schemes can be read in Annex I.

4.6 Calculation

In order to ensure the comparability of results across multiple studies, whilst balancing computational efficiency and solution accuracy, an optimal compromise between time step size and the total number of time steps was determined through iterative experimentation. The temporal resolution of the simulation was set to 2 milliseconds to avoid large mesh deformation and negative mesh in large pitch amplitude (Xiong & Liu, 2020), with a total of 2,000 time steps, thereby yielding a simulation duration of 4 seconds per study. In order to promote numerical convergence within each time step, the number of internal iterations was set to 20.

Chapter 5

Results and Discussion

Given the computational domain and parameter space specified previously, the execution of each transient simulation required approximately 10-12 hours of wall clock time, being a limitation due to time constraints for the realisation oh this work. The hardware configuration was the following:

Table 5.1: Hardware and software specification.

Component	**Specification**
Processor	AMD Ryzen 5 5600H w/ Radeon Graphics
RAM	32 GB
Graphics	NVIDEA GeForce RTX 3050
Storage	1 TB SSD
Operating System	Windows 11 Home
CFD Software	ANSYS (Fluent)
Code Compiler	Visual Studio Code
Coding Language	Phyton and C

The post-processing procedure focused on three flow metrics: (i) the drag coefficient (C_D), (ii) the lift coefficient (C_L), and (iii) the area-weighted average velocity, measured at a probe located 15 cm downstream of the fin tip. The quantities under consideration were selected with a view to quantifying the sensitivity of the wake to variations in the kinematic input variables. This chapter focusses on displaying the results from the simulations considering the Classic Sinusoidal

Movement (CSM) from a symmetrical sinusoidal wave, and the Alternative Turtle Movement (ATM), a movement using a Fourier approximation to simulate a visually more similar movement to the one expected from larger mammals, reptiles (such as the turtle) or fishes.

5.1 Velocity Analysis

5.1.1 Classic Sinusoidal Movement

As illustrated in Figure 5.1, the temporal progression of probe velocity is depicted for a fin oscillating with an amplitude of 30° and a length of 50 cm. As the oscillation frequency is increased across the tested range, the mean probe velocity rises by approximately a factor of 1.8 on average, thereby underscoring the dominant influence of actuation frequency on wake entrainment.

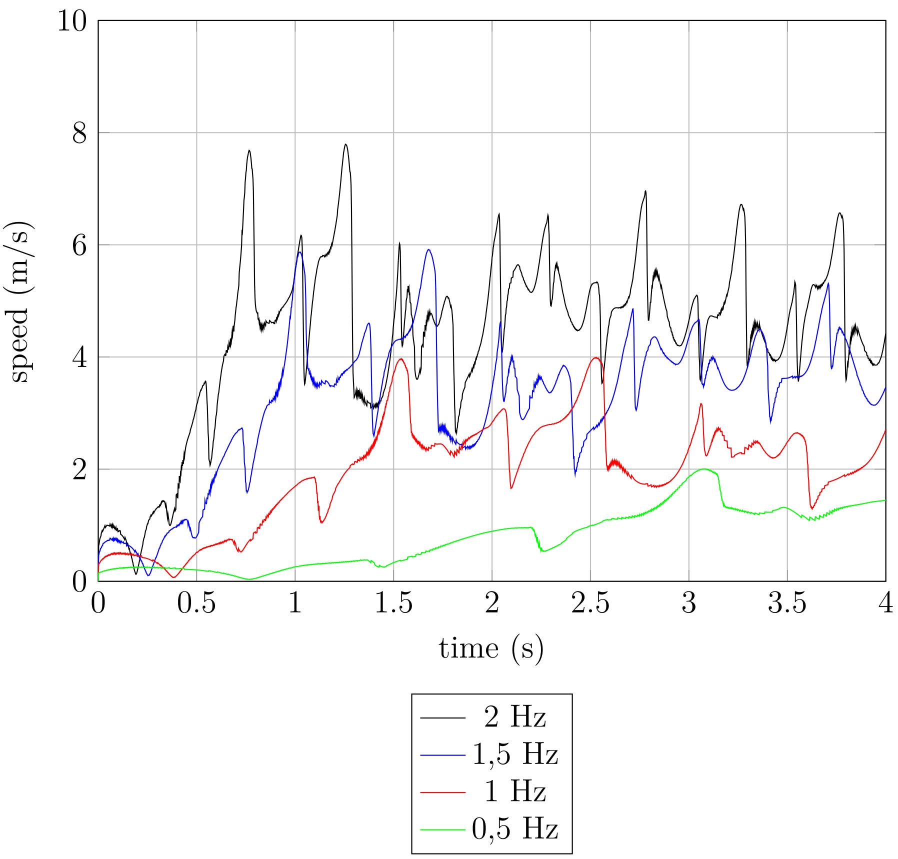

FIGURE 5.1: Fluid flow velocity with 50 cm fin and 30º amplitude

The complementary velocity-magnitude contours in Figure 5.2 reveal the formation and convection of coherent vortical structures generated by the rapid fin motion, with the highest velocity peaks clearly tracking the instantaneous fin position.

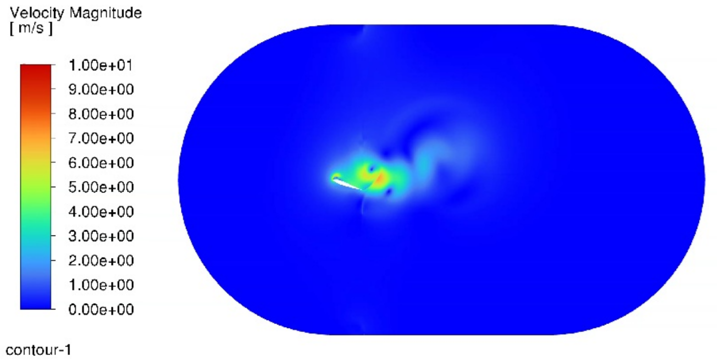

FIGURE 5.2: Instant velocity contour plot of the 50 cm fin, with 30º amplitude at 2 Hz.

To estimate the mean fluid velocity $\bar{U}$, at the outlet section of the flow channel, after the flow field has stabilized, and mitigate transient fluctuations, a 255-order moving average filter — the maximum permitted by Microsoft Excel — was applied to the velocity time series. This smoothing procedure was used to reduce the effect of high-frequency oscillations and vortical structures caused by rapid fin movement, helping to achieve an observable stable mean velocity.

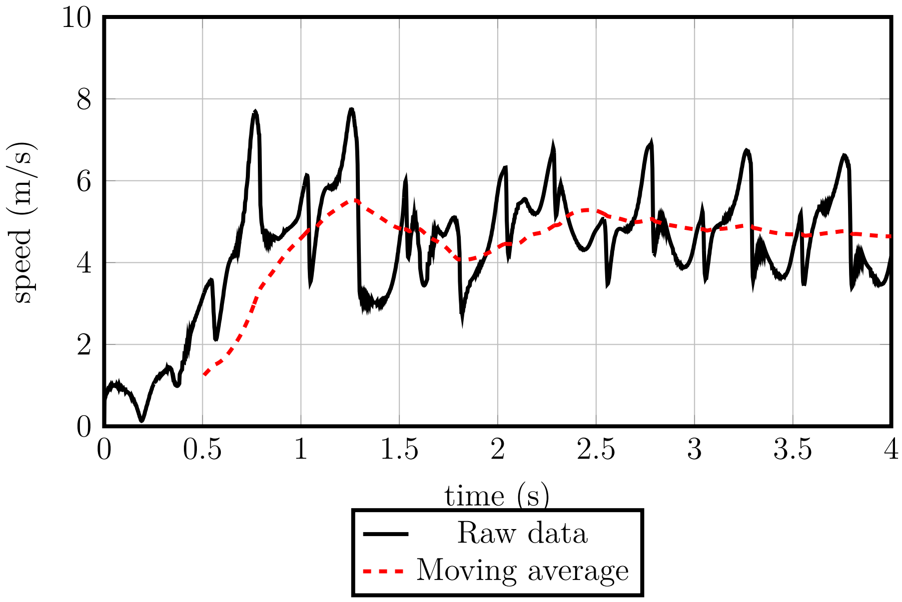

FIGURE 5.3: Fluid flow and a moving average with an order of 255, for 30º amplitude at 2 Hz

The same process was repeated with all other simulations. For the majority of this study the effect of gravity was neglected seen that the the fin was oscillating horizontally and not vertically. However, a simulation considering its effects was run. Contrary to what was expected, the velocity profile is equal to the simulation without gravity along the y axis, however the lift forces increased producing a higher estimated power loss and less thrust power.

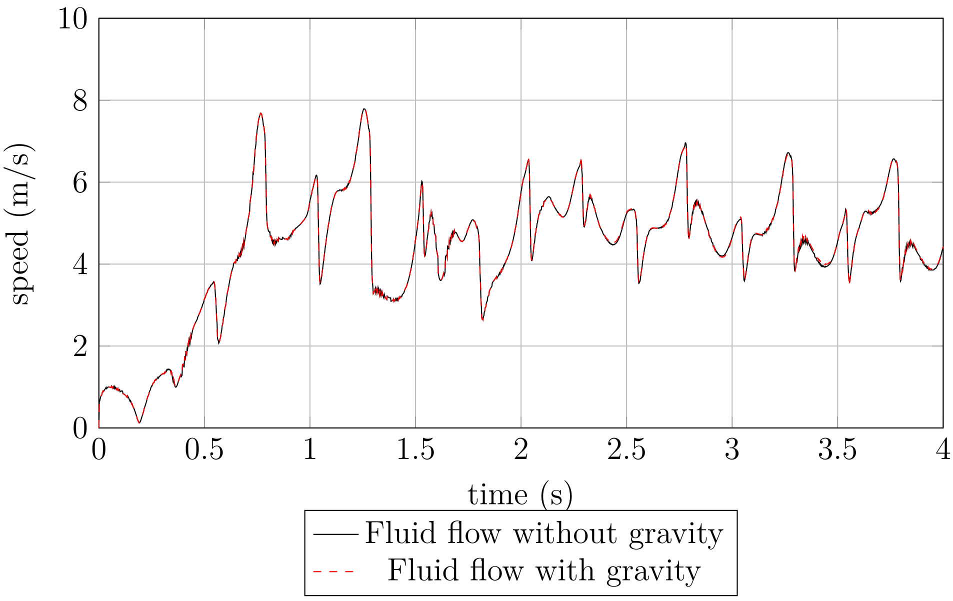

FIGURE 5.4: Fluid flow for 30º amplitude at 2 Hz considering gravity

All simulations with the same lenght ran using a fix valued interval, to maintain a steady visual of the contour plot for comparative purposes. In Figure 5.5, the instant in which the velocity contour plot was taken corresponds to the last descent motion of the fin during the 4 second simulation. At a frequency of 2 Hz, the highest tested, the wake exhibits strong vortical structures and elevated velocity gradients, indicating a highly energetic and unsteady flow characterised by pronounced vortex shedding. When the frequency is reduced to 1.5 Hz, the vortical patterns remain significant, but begin to display a slightly less coherent structure while still promoting substantial fluid mixing. At 1 Hz, the wake intensity decreases further, with weaker vortex formation and reduced disturbance to the surrounding flow. At the lowest frequency of 0.5 Hz, the wake is considerably weaker, with minimal velocity gradients and a flow field approaching laminar behaviour, proving that higher frequencies intensify vortex strength and mixing, but also increase flow unsteadiness. Conversely, lower frequencies diminish vortex activity and reduce hydrodynamic performance.

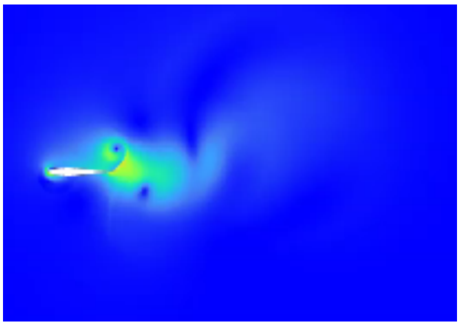

(A) 2 Hz

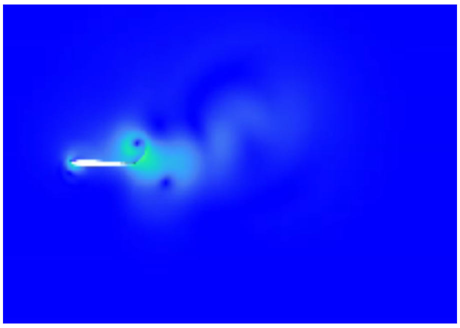

(B) 1.5 Hz

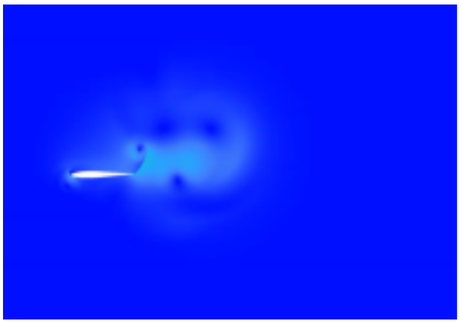

(C) 1 Hz

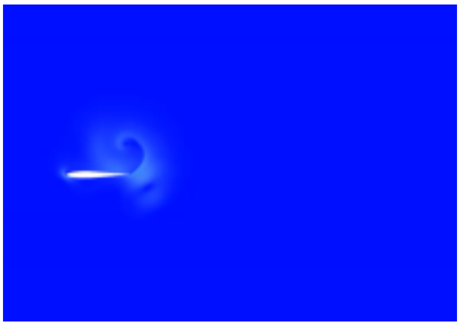

(D) 0.5 Hz

FIGURE 5.5: Instant velocity contour plots from the last descending motion of a fin with 40 cm with 22.5º amplitude

The problem with 4 seconds simulation for all variables becomes evident here, with a fluid flow still in development, as can be seen in Figure 5.5d. The slow movement makes it so that the fluid has not yet stabilized before the end of the simulation. However, due to computational limitations, it is not possible to expand the duration of the simulation for further than 4 seconds, aas this would result in a crash and the loss of most data.

5.1.2 Alternative Turtle Movement

For the ATM, similar to the leatherback sea turtles swim pattern, the UDF written contemplated a 6 order Fourier approximation, see Appendix C. This movement was studied as a comparison of velocity, required power and overall efficiency to determine an alternative to the CSM sinusoidal movement. This movement was studied as an alternative to the sinusoidal classic movement only to present other possibilities for the synthetic data generation, through CFD simulation. Figure 5.6 describes the velocity profile achieved by the proposed ATM movement.

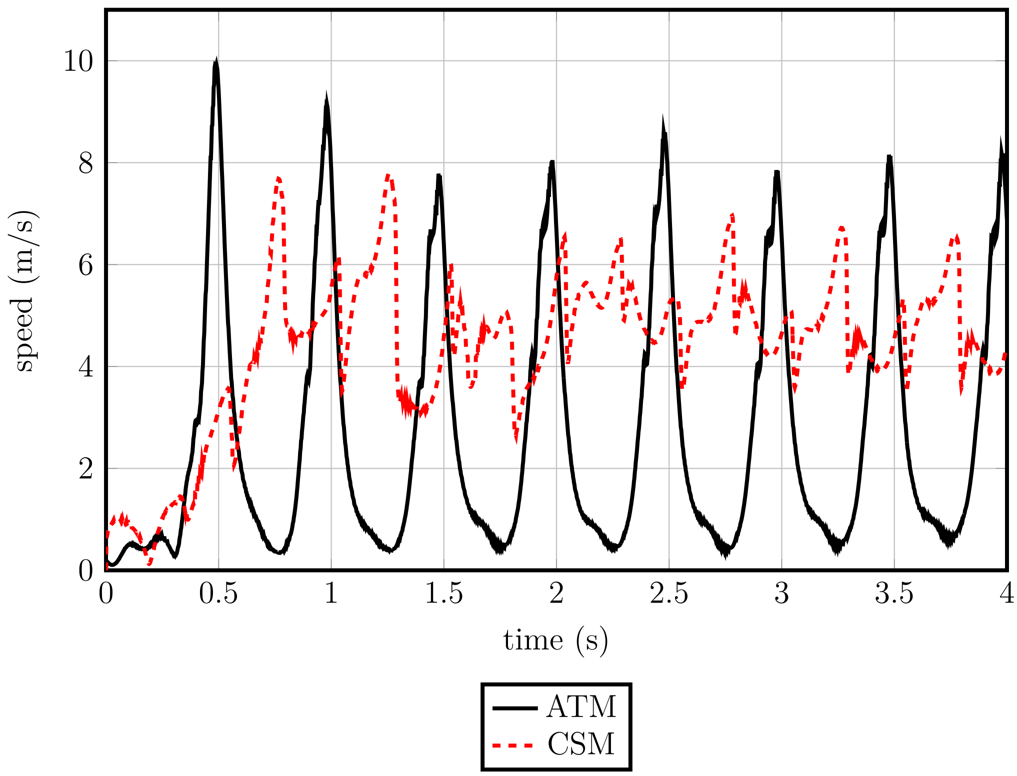

FIGURE 5.6: Comparison between the throbbing and sinusoidal movements

The results reveal clear differences in both amplitude and temporal characteristics of the two motion strategies. The ATM produces sharp velocity peaks that reach values close to 10 m/s, followed by rapid decelerations to near-zero speed, generating a strongly impulse flow pattern. This behaviour reflects the intermittent nature of the motion, with distinct thrust and recovery phases that induce high instantaneous accelerations. In contrast, the CSM exhibits a smoother and more continuous velocity profile, characterized by lower peak speeds, generally between 5 and 7 m/s, and the absence of complete flow stagnation between cycles. The sinusoidal form of the CSM results in reduced velocity fluctuations and a more gradual acceleration–deceleration process, which distributes the energy transfer more evenly over time. Collectively, these observations indicate that the ATM leads to more pronounced unsteady flow conditions with stronger instantaneous thrust production, whereas the CSM produces a steadier but less intense velocity response. This distinction highlights the fundamental differences in hydrodynamic performance and flow control mechanisms between the two locomotion strategies.

The contour plots in Figure 5.7 displays the evolution in one full cycle of the throbbing motion. Contrary to the sinusoidal movement, it is not necessary to wait for a stabilization of the fluid flow since there is an almost complete separation of the fluid from the fin.

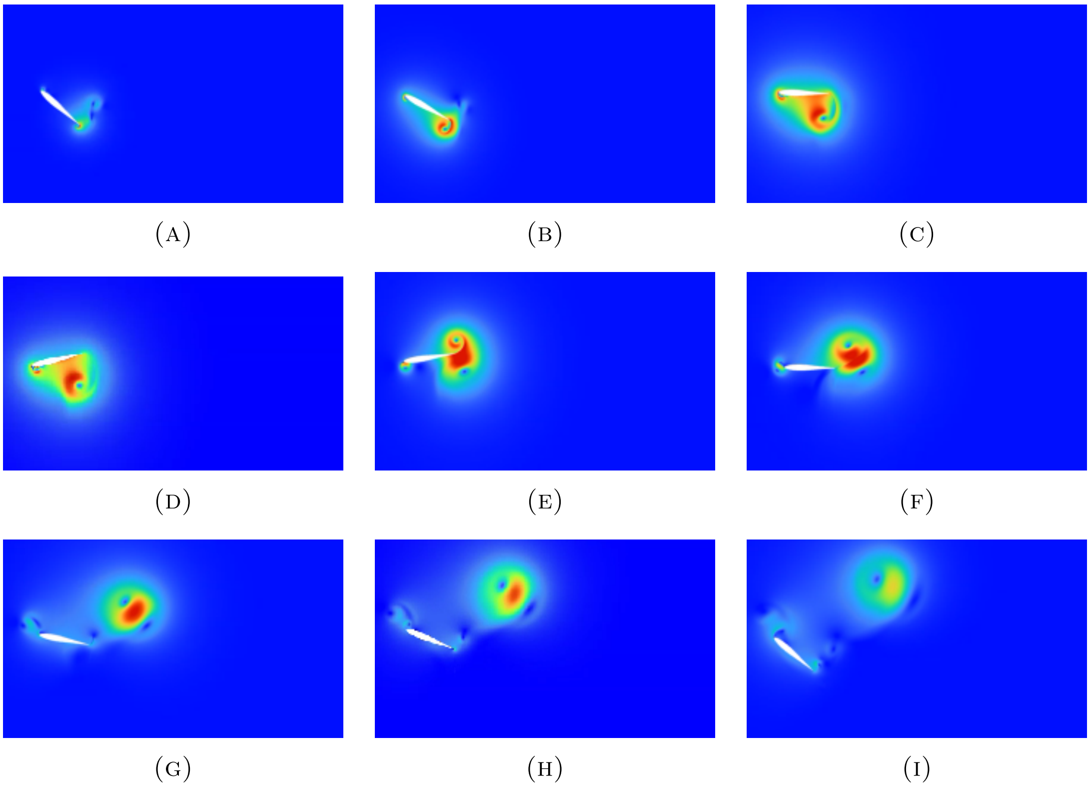

FIGURE 5.7: Instant velocity contour plots from the evolution of the throbbing movement in one cycle, scaled from 0 to 10 m/s

5.2 Forces and Energy

For the expected force and energy, the equations explained in Appendix D. In terms of expected thrust power, in Watts (W), the results are presented in the Table 5.2 and 5.3.

TABLE 5.2: Average thrust per cycle (W) for 50 cm fin

Frequency (Hz)	**Amplitude (θ)**		
	30º	**22.5º**	**15º**
2.0	3758.15	1494.55	359.28
1.5	1419.91	511.16	129.14
1.0	200.37	63.00	12.82
0.5	13.05	4.50	1.01

TABLE 5.3: Average thrust per cycle (W) for 40 cm fin

Frequency (Hz)	Amplitude (θ)		
	30º	**22.5º**	**15º**
2.0	3186.87	494.86	81.04
1.5	399.71	123.67	19.91
1.0	70.58	17.73	3.44
0.5	6.53	2.29	0.18

The simulation regarding the the throbbing movement led to an expected thrust power of 1292.56 W, for the 50 cm fin, and 1002.397 W for the 40 cm. As for the effect of gravity, the expected thrust power was 2033.86 W.

If we take the values from the 50 cm amplitude with 30° amplitude and a 1 Hz oscillation frequency as a basis — as these show fluid flow velocity stability closer to the 1 m/s goal (in this case, a higher value since this study disregards several losses such as power losses and drag due to the body from the vehicle), — it is possible to see that the energy necessity is approximately 7 times higher than for the 1.5 Hz movement and 18.5 times higher than for the 2 Hz movement. This shows that, although a 2 Hz movement allows for much higher expected velocities, achieving the goals of the SABUVIS project requires much lower energy consumption. When comparing the 40 cm fin different frequency values, we see that the 1.5 Hz movement is 5,7 times higher than the standard 1 Hz - also applicable here considering the expected velocities (see Appendix E). With these values, it is expected that the smaller the size of the fin, the smaller the difference between each oscilating frequency.

5.3 Efficiency

The concept of efficiency in fish-like swimming is ambiguous and controversial as discussed by Schultz and Webb, 2002 and Borazjani and Sotiropoulos, 2008. The efficiency of swimming is often measured in terms of Froude efficiency, which is defined as the ratio of the work done by the thrust force to the total power input Tytell, 2004.

$$\eta = \frac{\overline{F_T} U^*}{\overline{F_T} U^* + \overline{P_L}} \tag{5.1}$$

Where U^* is the steady swimming velocity, assumed through the moving average. The method of calculating $\overline{T}$ and P_L has been developed and used successfully by M. S. Triantafyllou et al., 1991. However, the Froude efficiency equation can only be applied under self-propulsion when the mean axial force is zero. If this equilibrium condition is violated, equation 5.1 loses its meaning. Graphs in Figure 5.8 display the estimated efficiency for each simulation, regarding the ATM simulations and a simulation ran accounting for the gravity.

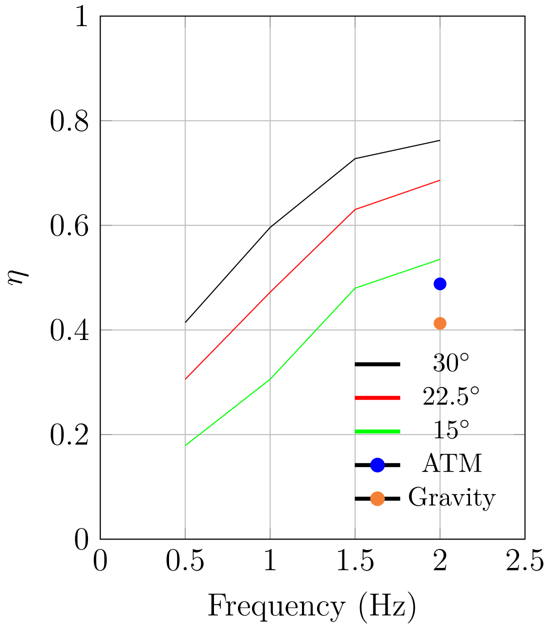

(a) 50 cm

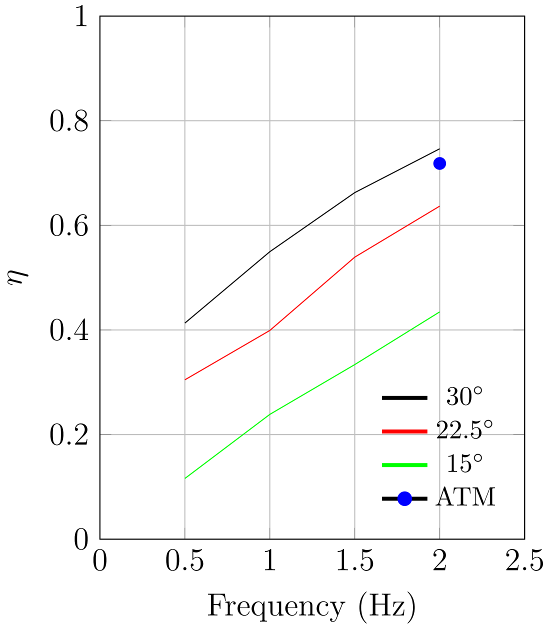

(b) 40 cm

FIGURE 5.8: Efficiency plots from a 50 cm fin (a) and a 40 cm fin (b)

A similar interval of efficiency results can be seen in the study from J. M. Anderson et al., 1997, with particular similarities in cases 3, 5 and 8. The data is presented in Figure 2.31, chapter 2. It is important to take into consideration that the efficiency results are based on variations from the Strouhal number, contrary to the ones presented in this work. When taking into consideration the equations for the efficiency calculation, it becomes evident that these values do not look deep into the actual expect efficiency from the movement of the fin. Being mostly affected by the velocity, it is obvious that the higher the velocity, the higher the efficiency. The values for a real efficiency would require actual physical tests to take place, however, this data can be introduced as a basis for real test prediction. Once real tests take place under identical or very similar conditions, it is possible to relate the data and find a ratio to apply as a correction to the data displayed here.

Chapter 6

Conclusion and Future Works

The present dissertation addressed the study, design, and simulation of biomimetic propulsion systems for the *SABUVIS II* project, focusing on their hydrodynamic performance and potential for synthetic data generation. The research was motivated by the growing operational demands of underwater missions, where noise reduction, manoeuvrability, and energy efficiency are critical design drivers. Within this context, CFD was employed as a primary tool to generate synthetic data in order to explore and optimise propulsion configurations, reducing reliance on costly and logistically complex field trials.

A comprehensive review of the literature established the scientific and technological context, covering biomimetic propulsion principles, synthetic data generation techniques, and the emerging role of Digital Twin technologies in the maritime domain. This review informs on the choice of simulation parameters, including fin geometry, oscillation frequency, amplitude, and motion profile, ensuring a realistic representation of operational constraints. The computational methodology involved the creation of accurate two-dimensional fin geometries, a mesh independence study to guarantee numerical reliability, and the simulation of two distinct movement profiles: a classic sinusoidal motion and an alternative turtle like motion inspired by nature.

The methodological framework that supported the study was detailed to allow a full understanding of the procedure from the definition of the fin profile, mesh independence study, and computational domain setup that constituted essential steps to ensure that the numerical results would be both reliable and reproducible. The mesh independence study, in particular, demonstrated that a sufficiently refined grid could capture the velocity fields and wake dynamics without excessive computational overhead, striking a balance between accuracy and efficiency. Moreover, the implementation of user-defined functions (UDFs) to prescribe the distinct kinematic patterns — the CSM and the ATM — allowed for a systematic exploration of the hydrodynamic consequences of different oscillatory modes. By establishing this computational workflow, the chapter provided not only the foundation for the present results but also a reusable template for future studies within the SABUVIS project.

Building upon this methodology, the results of the parametric simulations are discussed considering their hydrodynamic results. The velocity field analysis revealed clear distinctions between the two proposed movements. The CSM produced smoother and more continuous velocity profiles, with moderate peak magnitudes and a relatively stable wake structure. This consistency is particularly relevant for applications requiring predictable propulsion and reduced turbulence in the surrounding flow. Conversely, the ATM was characterized by highly impulse velocity responses, with sharp peaks reaching abou 1.5 times the magnitude of the CSM and intermittent phases of near-zero flow. These results highlight the capacity of ATM to generate strong, localized bursts of thrust, which could be advantageous for rapid manoeuvrers or escape strategies but may compromise efficiency in steady cruising regimes.

Further analysis of hydrodynamic forces and energy expenditure corroborated this distinction. The CSM showed lower instantaneous loads and more distributed energy consumption over the oscillation cycle, while the ATM concentrated energy into short, intense bursts. As a consequence, efficiency assessments revealed that optimal propulsion performance is strongly dependent on the intended operational profile. For sustained cruising and endurance missions, CSM appears favourable due to its smoother thrust generation and balanced energy demand. For tasks requiring agility or sudden accelerations, ATM provides the potential benefits of stronger instantaneous force, despite the associated cost in energy efficiency and wake stability.

Together, these findings underscore the central role of kinematic definition in propulsion efficiency and energy management in biomimetic underwater vehicles. From a methodological perspective, the study demonstrated the capacity of CFD to replicate complex unsteady fluid–structure interactions with sufficient fidelity to inform engineering design. From a practical perspective, the comparative assessment of CSM and ATM contributes valuable insight into the trade-offs inherent in biomimetic propulsion: stability versus intensity, efficiency versus maneuverability.

Finally, the results of Chapters 4 and 5 strengthen the argument for CFD-driven synthetic data generation as a viable approach for supporting future Digital Twin applications. The datasets produced are not merely isolated simulation outputs; they constitute structured and parametrized information on velocity profiles, hydrodynamic forces, and efficiency trends under varying movement patterns. This knowledge base can serve as the foundation for predictive modelling and optimization, reducing the reliance on costly experimental campaigns while accelerating the development cycle of the SABUVIS II project.

6.1 Future Works

Future research should extend the parametric space to include alternative fin morphologies and movement patterns such as combined heave-pitch, integrate fluid–structure interaction (FSI) models to evaluate the role of flexible materials, and simulate operation in more complex environmental conditions such as turbulence or strong currents. Validation experiments in controlled tank environments will be essential to quantify the simulation-to-reality gap, thereby increasing the reliability of synthetic datasets. In parallel, efforts should focus on embedding the propulsion model within a fully functional Digital Twin framework to enable real-time performance prediction, mission planning, and adaptive control.

Beyond performance evaluation, the digital twin supports three key applications. First, it enables safe development of control strategies by simulating system responses to variations in frequency or amplitude. Second, it provides a predictive framework: synthetic datasets offer an initial basis, which can be progressively calibrated with experimental data to improve accuracy. Third, integration at the vehicle level allows assessment of overall performance, including energy use, hydrodynamic interactions, and manoeuvrability, thereby guiding design and mission planning.

By pursuing these directions, the SABUVIS II project can further bridge the gap between simulation-based design and operational deployment, accelerating the realisation of next-generation stealthy, efficient, and adaptable underwater systems.

Bibliography

Akçakaya, H., Yildiz, H. A., Sağlam, G., & Gürleyen, F. (2009). Sliding mode control of autonomous underwater vehicle. *2009 International Conference on Electrical and Electronics Engineering - ELECO 2009*. https://doi.org/10.1109/ELECO.2009.5355270

Álvarez-Tuñón, O., Kanner, H., Marnet, L. R., Pham, H. X., le Fevre Sejersen, J., Brodskiy, Y., & Kayacan, E. (2023). *Mimir-uw: A multipurpose synthetic dataset for underwater navigation and inspection*. https://doi.org/10.1109/IROS55552.2023.10341436

Amer, A., Álvarez-Tuñón, O., Uğurlu, H. İ., Le Fevre Sejersen, J., Brodskiy, Y., & Kayacan, E. (2023). Unav-sim: A visually realistic underwater robotics simulator and synthetic data-generation framework. *2023 21st International Conference on Advanced Robotics (ICAR)*, 570–576. https://doi.org/10.1109/ICAR58858.2023.10406819

Anderson, J. M., Streitlien, K., Barrett, D. S., & Triantafyllou, M. S. (1997). Oscillating foils of high propulsive efficiency. *Journal of Fluid Mechanics*, *360*, 41–72. https://doi.org/10.1017/S0022112097008392

Anderson, J. D. (1995). *Computational fluid dynamics: The basics with applications*. McGraw-Hill.

Anderson, J. M., & Chhabra, N. K. (2002). Maneuvering and stability performance of a robotic tuna. *Integrative and Comparative Biology*, *42*(1), 118–126. https://doi.org/10.1093/icb/42.1.118

António, T. M. G. (2022). *Projeto sabuvis: Desenvolvimento de um modelo matemático de um veículo não tripulado de subsuperfície biomimético* [Doctoral dissertation, Escola Naval].

Araújo, H. (2020). *Projeto e desenvolvimento de um veículo autónomo biomimético de subsuperfície - projeto e desenvolvimento do hardware e software* [Doctoral dissertation, Escola Naval].

Autiosalo, J. (2018). Platform for industrial internet and digital twin focused education, research, and innovation: Ilmatar the overhead crane. *2018 IEEE 4th World Forum on Internet of Things (WF-IoT)*, 241–244. https://doi.org/10.1109/WF-IoT.2018.8355217

Bauer, A., Trapp, S., Stenger, M., Leppich, R., Kounev, S., Leznik, M., Chard, K., & Foster, I. T. (2024). Comprehensive exploration of synthetic data generation: A survey [Survey of 417 synthetic data generation models over the last decade]. *arXiv preprint*, *abs/2401.02524*. https://doi.org/10.48550/arXiv.2401.02524

Bauer, D. F., Russ, T., Waldkirch, B. I., Tönnes, C., Segars, W. P., Schad, L. R., Zöllner, F. G., & Golla, A.-K. (2021). Generation of annotated multimodal ground truth datasets for abdominal medical image registration [Uses CycleGAN and XCAT phantom to generate synthetic multimodal abdominal image datasets]. *International Journal of Computer Assisted Radiology and Surgery*, *16*(8), 1277–1285. https://doi.org/10.1007/s11548-021-02372-7

Bellingham, J. G., Goudey, C. A., Consi, T. R., Bales, J. W., Atwood, D. K., Leonard, J. J., & Chryssostomidis, C. (1994). A second generation survey auv. *Proceedings of IEEE Symposium on Autonomous Underwater Vehicle Technology (AUV'94)*, 148–155. https://doi.org/10.1109/AUV.1994.518619

Blidberg, D. R. (2001). The development of autonomous underwater vehicles (auv); a brief summary.

Borazjani, I., & Sotiropoulos, F. (2008). Numerical investigation of the hydrodynamics of carangiform swimming in the transitional and inertial flow regimes. *The Journal of Experimental Biology*, *211*(Pt 10), 1541–1558. https://doi.org/10.1242/jeb.015644

Boschert, S., & Rosen, R. (2016). Digital twin—the simulation aspect. In P. Hehenberger & D. Bradley (Eds.), *Mechatronic futures: Challenges and solutions for mechatronic systems and their designers* (pp. 59–74). Springer International Publishing. https://doi.org/10.1007/978-3-319-32156-1_5

Boudis, A., Benzaoui, A., Oualli, H., Guerri, O., Bayeul-Lainé, A. C., & Coutier Delgosha, O. (2018). Energy extraction performance improvement of a flapping foil by the use of combined foil. *Journal of Applied Fluid Mechanics*, *11*(6), 1651–1663. https://doi.org/10.29252/jafm.11.06.29099

Cruz, N. A., & Matos, A. C. (2008). The mares auv, a modular autonomous robot for environment sampling. *OCEANS 2008, Vols 1–4*, 1996–2001. https://doi.org/10.1109/oceans.2008.5152096

Dalaklis, D., Pastra, A., & Johansson, T. (2024). Unmanned and unbound: How drones are redefining the maritime sector and reshaping naval operations. *15th Annual Conference of the NATO Maritime Interdiction Operational Training Centre (NMIOTC)*. https://www.researchgate.net/publication/

382524430_Unmanned_and_Unbound_How_Drones_are_Redefining_the_Maritime_Sector_and_Reshaping_Naval_Operations

de Paiva, G. D. (2020). *Desenvolvimento de um veículo autónomo biomimético* (tech. rep.). Escola Naval.

Eddy, C. W. (2024, May). *Digital twin in military ground vehicles: Design and predictive maintenance* [Master's thesis, Clemson University]. https://tigerprints.clemson.edu/all_theses

Emmert-Streib, F., Tripathi, S., & Dehmer, M. (2023). Analyzing the scholarly literature of digital twin research: Trends, topics and structure. *IEEE Access*, *11*, 69649–69666. https://doi.org/10.1109/ACCESS.2023.3290488

Fluent, A. (2009, January). Ansys fluent [Accessed in: 22 may 2025]. https://www.afs.enea.it/project/neptunius/docs/fluent/html/ug/node785.htm

Fox, R. W., McDonald, A. T., & Pritchard, P. J. (2011). *Introduction to fluid mechanics* (8th ed.). John Wiley & Sons.

Gartner. (2019, March). Top 10 strategic technology trends for 2019: Digital twins. https://www.gartner.com/en/documents/3904569

Ghasemnezhad, M., & Roohi, E. (2024). Large eddy simulation of cavitating flow around a pitching hydrofoil. *Ocean Engineering*, *292*, 116547. https://doi.org/https://doi.org/10.1016/j.oceaneng.2023.116547

Grieves, M., & Vickers, J. (2016, August). *Digital twin: Mitigating unpredictable, undesirable emergent behavior in complex systems (excerpt)*, Digital Twin Institute. https://doi.org/10.13140/RG.2.2.26367.61609

Group, S. M. (1995). Robotuna, prototype underwater robot, 1995 [Accessed: 2025-06-16].

Guo, Z. Z., Wang, K., Qin, J. Y., Li, X. B., Ran, D. C., & Shen, Y. (2021). An intelligent maritime scene frame prediction based on digital twins technology. *Proceedings 2021 IEEE 1st International Conference on Digital Twins and Parallel Intelligence, DTPI 2021*, 25–28. https://doi.org/10.1109/DTPI52967.2021.9540188

Hackaday. (2017, March). Osug: Open-source underwater glider | details | hackaday.io. https://hackaday.io/project/20458-osug-open-source-underwater-glider/details

Hu, S., Liang, Q., Huang, H., & Yang, C. (2023). Construction of a digital twin system for the blended-wing-body underwater glider. *Ocean Engineering*, *270*. https://doi.org/10.1016/j.oceaneng.2022.113610

Hughes, G. R., Luschi, P., Mencacci, R., & Papi, F. (1998). *The 7000-km oceanic journey of a leatherback turtle tracked by satellite* (tech. rep.).

Huntington Ingalls Industries (HII). (2021). Remus uuvs (unmanned underwater vehicles) [Accessed: 2025-05-14].

Instituto Superior Técnico. (2017, June). Medusa deep sea successfully passed its first major test [Accessed 2025-05-15].

Jain, S., Seth, G., Paruthi, A., Soni, U., & Kumar, G. (2022). Synthetic data augmentation for surface defect detection and classification using deep learning [Proposes GAN-based synthetic image generation to augment NEU surface defect dataset for improved CNN-based classification]. *Journal of Intelligent Manufacturing*, *33*(4), 1007–1020. https://doi.org/10.1007/s10845-020-01710-x

Jeong, W., & Seong, J. (2013). Comparison of effects on technical variances of computational fluid dynamics (cfd) software based on finite element and finite volume methods. *Journal of Mechanical Science and Technology*, *27*(12), 3767–3774.

Ji, G., Hao, J. G., Gao, J. L., & Lu, C. Z. (2021). Digital twin modeling method for individual combat quadrotor uav. *Proceedings 2021 IEEE 1st International Conference on Digital Twins and Parallel Intelligence, DTPI 2021*, 1–4. https://doi.org/10.1109/DTPI52967.2021.9540131

Jones, D., Smith, R., & Patel, K. (2022). Advances in computational fluid dynamics for marine applications. *Journal of Marine Science and Engineering*, *10*(4), 512. https://doi.org/10.3390/jmse10040512

Kármán, T. v. (1911). Über den mechanismus des widerstandes, den ein bewegter körper in einer flüssigkeit erfährt. *Nachrichten von der Gesellschaft der Wissenschaften zu Göttingen, Mathematisch-Physikalische Klasse*, 509–517. https://eudml.org/doc/58812

Kim, D., Choi, M., & Um, J. (2024). Digital twin for autonomous collaborative robot by using synthetic data and reinforcement learning. *Robotics and Computer-Integrated Manufacturing*, *85*, 102632. https://doi.org/https://doi.org/10.1016/j.rcim.2023.102632

Koh, C. (2019, September). Véhicules sous-marins biomimétiques [Consulted on 14 March 2025].

Lee, F., Hajisharif, S., & Johnson, E. (2025). The ontological politics of synthetic data: Normalities, outliers, and intersectional hallucinations. *Big Data & Society*, *12*(2), 20539517251318289. https://doi.org/10.1177/20539517251318289

Lee, J., Viswanath, K., Geder, J., Sharma, A., Pruessner, M., & Zhou, B. (2023). Data-driven inverse control of flapping fin uuvs using synthetic thrust sequences. *Proceedings of the AAAI Conference on Artificial Intelligence*, *37*(11), 13113–13121. https://doi.org/10.1609/aaai.v37i11.27527

Lee, J., Viswanath, K., Sharma, A., Geder, J., Ramamurti, R., & Pruessner, M. D. (2024). Data-driven approaches for thrust prediction in underwater flapping fin propulsion systems [Proposes data-efficient ML models for predicting thrust from fin geometry and kinematics]. *arXiv preprint*, *abs/2406.01947*. https://doi.org/10.48550/arXiv.2406.01947

Liu, J., & Hu, H. (2004). Building a simulation environment for optimising control parameters of an autonomous robotic fish.

Lubis, M. B., Kimiaei, M., & Efthymiou, M. (2021). Alternative configurations to optimize tension in the umbilical of a work class rov performing ultra-deep-water operation. *Ocean Engineering*, *225*. https://doi.org/10.1016/j.oceaneng.2021.108786

Masmitja, I., Gonzalez, J., Galarza, C., Gomariz, S., Aguzzi, J., & del Rio, J. (2018). New vectorial propulsion system and trajectory control designs for improved auv mission autonomy. *Sensors (Switzerland)*, *18*. https://doi.org/10.3390/s18041241

Mazlan, A., & Naddi, A. (2015, January). *A fully actuated tail propulsion system for a biomimetic autonomous underwater vehicle* [Doctoral dissertation, Aerospace].

Mishra, R. (2024, December). *Wind inflow customisation at wind turbine blade scale using wind tunnel experiments and cfd simulations* (Publication No. 2024ECDN0040) [Doctoral dissertation, École centrale de Nantes] [Thesis available at https://theses.hal.science/tel-04908316v2/file/R_MISHRA.pdf]. https://theses.hal.science/tel-04908316

Moore, S. (2019). *Acoustic signature control on maritime platforms* (tech. rep.). Maritime Division, Defence Science and Technology Group.

Moukalled, F., Mangani, L., & Darwish, M. (2016). *The finite volume method in computational fluid dynamics: An advanced introduction with openfoam® and matlab®*. Springer. https://doi.org/10.1007/978-3-319-16874-6

Muijres, F., Lentink, D., Oudheusden, B., & Van Leeuwen, J. L. (2005). Visualization of vortex wake interactions of a flapping foil. *Journal of Experimental Biology - J EXP BIOL*.

Navy, U. (2004, November). *The navy unmanned undersea vehicle (uuv) master plan* (tech. rep.). United States Navy.

Negri, E., Fumagalli, L., & Macchi, M. (2017). A review of the roles of digital twin in cps-based production systems. *Procedia Manufacturing*, *11*, 939–948. https://doi.org/10.1016/j.promfg.2017.07.198

Prabu, T., et al. (2024). Hydrodynamic analysis of a flopping naca0012 hydrofoil and its application. *Journal of Applied Fluid Mechanics*, *17*(4), 889–899.

Prezentacja finalna pojazdów SABUVIS. (2018, October 16). Kierunek Automatyka i Robotyka, Politechnika Krakowska. Retrieved August 14, 2025, from https://air.pk.edu.pl/index.php/prezentacja-finalna-pojazdow-sabuvis/

Raghunathan, T. E. (2021). Synthetic data. *Annual Review of Statistics and Its Application*, *8*(Volume 8, 2021), 129–140. https://doi.org/https://doi.org/10.1146/annurev-statistics-040720-031848

Schultz, W. W., & Webb, P. W. (2002). Power requirements of swimming: Do new methods resolve old questions? *Integrative and Comparative Biology*, *42*(5), 1018–1025. https://doi.org/10.1093/icb/42.5.1018

Scipanov, L. V., & Totir, V. C. (2023). The need to adapt naval tactics to technological evolution – drones and drone-carrying platforms. *Scientific Bulletin of Naval Academy*, *26*(2), 123–130. https://doi.org/10.21279/1454-864X-23-I2-123

Sfakiotakis, M., Lane, D. M., Bruce, J., & Davies, C. (1999). *Review of fish swimming modes for aquatic locomotion* (tech. rep.).

Slotnick, J. P., et al. (2015). *Grid convergence for turbulent flows* (tech. rep.). NASA Technical Reports Server. https://ntrs.nasa.gov/api/citations/20150005716/downloads/20150005716.pdf

Stevens, W. O., & Westcott, A. F. (1920). *A history of sea power* [Includes maps, diagrams, and illustrations]. George H. Doran Company.

Sun, Q., Hua, E., Sun, L., Qiu, L., Song, Y., & Xiang, M. (2024). Study on the hydrodynamic performance of swing-type flapping hydrofoil bionic pumps affected by foil camber. *Water*, *16*(4), 595. https://doi.org/10.3390/w16040595

Szymak, P. (2016). Mathematical model of underwater vehicle with undulating propulsion. *Proceedings - 2016 3rd International Conference on Mathematics and Computers in Sciences and in Industry, MCSI 2016*, 269–274. https://doi.org/10.1109/MCSI.2016.16

Szymak, P., & Przybylski, M. (2018). Thrust measurement of biomimetic underwater vehicle with undulating propulsion. *Zeszyty Naukowe Akademii Marynarki Wojennej*, *213*, 81–127. https://doi.org/10.2478/sjpna-2018-0014

Tao, F., Cheng, J., Qi, Q., Zhang, M., Zhang, H., & Sui, F. (2017). Digital twin-driven product design, manufacturing and service with big data. *International*

Journal of Advanced Manufacturing Technology, *94*, 3563–3576. https://doi.org/10.1007/s00170-017-0233-1

Tao, F., Zhang, H., Liu, A., & Nee, A. Y. C. (2019). Digital twin in industry: State-of-the-art. *IEEE Transactions on Industrial Informatics*, *15*. https://ieeexplore.ieee.org/stamp/stamp.jsp?tp=&arnumber=8477101

Techet, A. H., Hover, F. S., & Triantafyllou, M. S. (2003, October). *Separation and turbulence control in biomimetic flows* (tech. rep.). Turbulence and Combustion Flow.

Toet, W. (2019, February). Willem toet explains. . . cfd post processing. https://www.racetechmag.com/2019/02/willem-toet-explains-cfd-post-processing/

Tools, A. (2025). Naca 4 digit airfoils [Accessed: 2025-03-26]. http://airfoiltools.com/airfoil/naca4digit

Triantafyllou, M. S., Triantafyllou, G. S., & Yue, D. K. (2000). Hydrodynamics of fishlike swimming. *Annual Review of Fluid Mechanics*, *32*, 33–53. https://doi.org/10.1146/annurev.fluid.32.1.33

Triantafyllou, M. S., & Triantafyllou, G. S. (1995). An efficient swimming machine. *Scientific American*, 64–71. http://weblinks3.epnet.com/DeliveryPrintSave.asp?tb=1&_ua=bo+...

Triantafyllou, M. S., Triantafyllou, G. S., & Gopalkrishnan, R. (1991). Wake mechanics for thrust generation in oscillating foils. *Physics of Fluids A*, *3*(12), 2835–2837. https://doi.org/10.1063/1.858173

Tukasiewicz. (2025). The 'sabuvis' project: Shoal of biomimetic underwater vehicles for underwater reconnaissance [Consulted on 14 March 2025]. *Sieć Badawcza ŁUKASIEWICZ – PIAP (Industrial Research Institute for AutomationMeasurements)*. https://piap.lukasiewicz.gov.pl/en/research-projects/the-sabuvis-project/

Tytell, E. D. (2004). The hydrodynamics of eel swimming: I. wake structure. *Journal of Experimental Biology*, *207*(11), 1825–1841. https://doi.org/10.1242/jeb.00968

Uddin, J., Wadud, M. F., Ashrafi, R., Alam, M. G. R., & Rhaman, M. K. (2023). Landing with confidence: The role of digital twin in uav precision landing. *Proceedings of 10th International Conference on Recent Advances in Air and Space Technologies, RAST 2023*. https://doi.org/10.1109/RAST57548.2023.10197983

Uri, J. (2020, April). 50 years ago: "houston, we've had a problem" - nasa. https://www.nasa.gov/history/50-years-ago-houston-weve-had-a-problem/

Venkatakrishnan, V., & Mavriplis, D. J. (1993). Implicit solvers for unstructured meshes. *Journal of Computational Physics*, *105*(1), 83–91. https://doi.org/https://doi.org/10.1006/jcph.1993.1055

Versteeg, H. K., & Malalasekera, W. (2007a). *An introduction to computational fluid dynamics: The finite volume method* (2nd ed.). Pearson Education.

Versteeg, H. K., & Malalasekera, W. (2007b). *An introduction to computational fluid dynamics: The finite volume method* (2nd). Pearson Education Ltd.

Villeneuve, T., Boudreau, M., & Dumas, G. (2021). Assessing the performance and the wake recovery rate of flapping-foil turbines with end-plates and detached end-plates. *Renewable Energy*, *179*, 206–222. https://doi.org/10.1016/j.renene.2021.07.004

Wang, W. H., Chen, X. Q., Marburg, A., Chase, J. G., & Hann, C. E. (2008). A low-cost unmanned underwater vehicle prototype for shallow water tasks. *2008 IEEE/ASME International Conference on Mechatronic and Embedded Systems and Applications*, 204–209. https://doi.org/10.1109/MESA.2008.4735649

Watts, C. M. (2009). *A comparison study of biologically inspired propulsion systems for an autonomous underwater vehicle.* [Doctoral dissertation, University of Glasgow]. http://theses.gla.ac.uk/1672/

Xiong, Z., & Liu, X. (2020). Very large-eddy simulations of the flow past an oscillating cylinder at a subcritical reynolds number. *Applied Sciences*, *10*(5), 1870.

Zhao, Z., & Dou, L. (2019). Effects of the structural relationships between the fish body and caudal fin on the propulsive performance of fish. *Ocean Engineering*, *186*, 106117. https://doi.org/10.1016/j.oceaneng.2019.106117

Zhou, B., Viswanath, K., Geder, J., Sharma, A., & Lee, J. (2024). Insights into flexible bioinspired fins for unmanned underwater vehicle systems through deep learning. *Biomimetics*, *9*(7), 434. https://doi.org/10.3390/biomimetics9070434

Zhu, D., & Sun, B. (2013). The bio-inspired model based hybrid sliding-mode tracking control for unmanned underwater vehicles. *Engineering Applications of Artificial Intelligence*, *26*(10), 2260–2269. https://doi.org/10.1016/j.engappai.2013.08.017

Appendix A - y^+ Calculations

Estimating the first cell height for desired y^+ given:

1. Desired $y^+ = 1$
2. Dynamic viscosity: $\mu = 1.08 \times 10^{-3}\,\mathrm{Pa \cdot s}$
3. Density: $\rho = 1025\,\mathrm{kg/m^3}$
4. Freestream velocity: $U_\infty = 2\,\mathrm{m/s}$
5. Characteristic length: $L = 0.5\,\mathrm{m}$
6. Reynolds number (previously calculated): $Re_x \approx 9.59 \times 10^5$
7. Friction coefficient (empirical for turbulent flow):

$$C_f = \frac{0.026}{Re_x^{1/7}} \approx \frac{0.026}{(9.59 \times 10^5)^{1/7}} \approx 3.634 \times 10^{-3}$$

8. Wall shear stress:

$$\tau_{\mathrm{wall}} = \frac{C_f \cdot \rho V_\infty^2}{2} = \frac{3.634 \cdot 10^{-3} \cdot 1025 \cdot 4}{2} \approx 7.45\,\mathrm{Pa}$$

9. Friction velocity:

$$U_{\mathrm{fric}} = \sqrt{\frac{7.45}{1025}} \approx 0.08526\,\mathrm{m/s}$$

10. Kinematic viscosity:

$$\nu = \frac{\mu}{\rho} = \frac{1.08 \times 10^{-3}}{1025} \approx 1.05 \times 10^{-6}\,\mathrm{m^2/s}$$

11. First cell height:

$$\Delta s = \frac{y^+ \cdot \nu}{U_{\mathrm{fric}}} = \frac{1 \cdot 1.05 \times 10^{-6}}{0.08526} \approx 12.316 \times 10^{-6}\,\mathrm{m} = 12.32\,\mu\mathrm{m}$$

Appendix B - Sinusoidal Movement - UDF

In order to achieve a smooth and easy movement, a sinusoidal movement was created using *C* language to implement on the CFD software. This code created a base for all movements as it allowed quick changes and adaptation for different amplitudes (changing the #define AMP to a different value in radians - $\pi/6$ for 30°, $\pi/8$ for 22.5° and $\pi/12$ for 15°) and frequency (changing the #define FREQ to either 2, 1.5, 1, or 0.5 Hz). The code used is the following.

```

#include "udf.h"
#include "math.h"

#define AMP (M_PI/6.0)                    /* 30 degrees in radians */
#define FREQ 2.0                          /* Frequency in Hz */
#define ANG_VEL (2.0 * M_PI * FREQ)   /* Angular frequency (rad/s) */

DEFINE_CG_MOTION(shm, dt, cg_vel, cg_omega, time, dtime)
{
    real omega;

    omega = AMP * ANG_VEL * cos(ANG_VEL * time);

    cg_vel[0] = 0.0;
    cg_vel[1] = 0.0;
    cg_vel[2] = 0.0;

    cg_omega[0] = 0.0;
    cg_omega[1] = 0.0;
    cg_omega[2] = omega;
}
```

Source Code B.1: UDF code for sinusoidal movement

Appendix C - Alternative Turtle Movement - Fourier Approximation - UDF

In order to achieve a movement with a fast ascending movement and a slow descending, a line was plotted by hand on a Cartesian graph in order to capture the approximate desired value. This values where introduced on a python program to get the Fourier approximation values (see C.1).

```python
from scipy.optimize import leastsq
import numpy as np
import matplotlib.pyplot as plt

# Check new data spacing
x_new = np.array([0.6, 0.7, 0.8, 0.9, 1, 1.1 , 1.2 , 1.3, 1.4, 1.5, 1.6, 1.7, 1.8, 1.9, 2, 2.1 , 2.2 , 2.3, 2.4, 2.5, 2.6])
y_new = np.array([-0.5, 0, 0.5, 0.42, 0.25, 0.1, 0, -0.1, -0.25, -0.42, -0.5, 0, 0.5, 0.42, 0.25, 0.1, 0, -0.1, -0.25, -0.42, -0.5])

dx_new = np.diff(x_new)
dx_unique_new = np.unique(np.round(dx_new, decimals=5))

dx_unique_new


#Set Fourier basis until specifi N order
def fourier_series(x, a0, an, bn, T):
    result = a0 / 2
    for n in range(1, len(an) + 1):
        result += an[n-1] * np.cos(2 * np.pi * n * x / T)
        result += bn[n-1] * np.sin(2 * np.pi * n * x / T)
    return result

#Function that builds Fourier Series with N order
def fit_fourier(x, y, N):
    T = x[-1] - x[0]

    def model(p, x):
        a0 = p[0]
        an = p[1:N+1]
        bn = p[N+1:]
        return fourier_series(x, a0, an, bn, T)

    def error(p, x, y):
        return y - model(p, x)
```

```

    p0 = np.zeros(2 * N + 1)  #Initial starting point
    params, _ = leastsq(error, p0, args=(x, y))

    return lambda x_val: model(params, x_val), params

#Test different orders
orders = [5,6]
x_fit = np.linspace(x_new[0], x_new[-1], 1000)

plt.figure(figsize=(12, 6))
plt.scatter(x_new, y_new, color='black', label='Dados originais')

for N in orders:
    fitted_func, _ = fit_fourier(x_new, y_new, N)
    y_fit = fitted_func(x_fit)
```

Source Code C.1: Python code for Fourier approximation

These were introduced in a UDF to be implemented in the Dynamic Mesh.

```
#include "udf.h"
#include "math.h"

#define FREQ 1.0                    /* Frequency (Hz) */
#define M_PI 3.14159265358979323846
#define ANG_VEL (2.0 * M_PI * FREQ)     /* Base angular frequency (rad/s
    ) */

// Fourier coefficients
#define A0     -1.44684085e-03
#define A1      4.47098433e-04
#define A2      3.67051892e-01
#define A3     -1.17051891e-03
#define A4     -1.01574223e-01
#define A5      1.44684094e-03
#define A6     -5.38284712e-02
#define B1     -1.37602750e-03
#define B2     -1.18031633e-01
#define B3      8.50431769e-04
#define B4     -1.40565573e-01
#define B5      2.71488347e-13
#define B6      7.48491840e-02

DEFINE_CG_MOTION(shm, dt, cg_vel, cg_omega, time, dtime)
{
```

```
    real omega;

    omega = A0
        -A1 * ANG_VEL * sin(1.0 * ANG_VEL * time) + B1 * ANG_VEL * cos
    (1.0 * ANG_VEL * time)
        -A2 * 2.0 * ANG_VEL * sin(2.0 * ANG_VEL * time) + B2 * 2.0 *
    ANG_VEL * cos(2.0 * ANG_VEL * time)
        -A3 * 3.0 * ANG_VEL * sin(3.0 * ANG_VEL * time) + B3 * 3.0 *
    ANG_VEL * cos(3.0 * ANG_VEL * time)
        -A4 * 4.0 * ANG_VEL * sin(4.0 * ANG_VEL * time) + B4 * 4.0 *
    ANG_VEL * cos(4.0 * ANG_VEL * time)
        -A5 * 5.0 * ANG_VEL * sin(5.0 * ANG_VEL * time) + B5 * 5.0 *
    ANG_VEL * cos(5.0 * ANG_VEL * time)
        -A6 * 6.0 * ANG_VEL * sin(6.0 * ANG_VEL * time) + B6 * 6.0 *
    ANG_VEL * cos(6.0 * ANG_VEL * time);


    cg_vel[0] = cg_vel[1] = cg_vel[2] = 0.0;
    cg_omega[0] = cg_omega[1] = 0.0;
    cg_omega[2] = omega;
}
```

Source Code C.2: UDF code for throbbing movement

Appendix D - Forces and Energy Equations

To calculate an estimate of the efficiency, an interpretation of the equations from different studies among which J. M. Anderson et al. (1997), Borazjani and Sotiropoulos (2008), Boudis et al. (2018), Sun et al. (2024), M. S. Triantafyllou and Triantafyllou (1995), and Xiong and Liu (2020) was used, considering the lift and drag coefficients and decomposing them into forces acting on the fin. Figure D.1 decomposes the forces produced by the movement of the fin. The F_x and F_Y forces are usually considered the drag and lift forces considering Newton's second law.

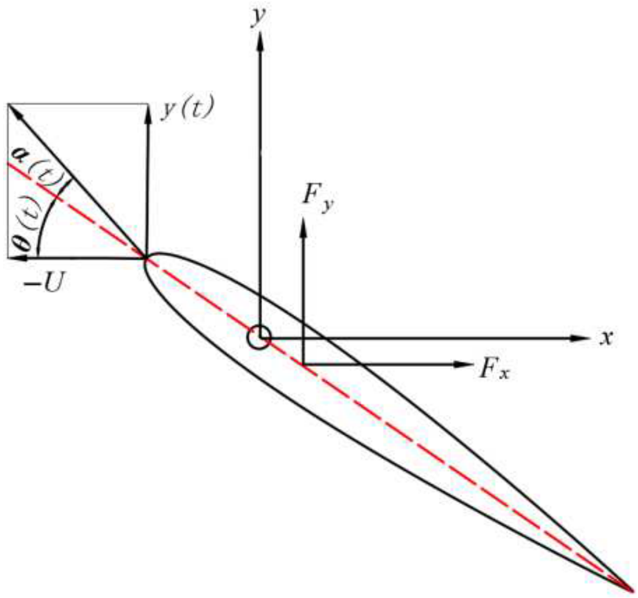

FIGURE D.1: Schematic diagram of two-dimensional rigid biomimetic flapping hydrofoil mechanic. Source: Sun et al., 2024

Furthermore, through Equation D.1, it is possible to decompose the displacement of the fin, with θ as the angle between the chord line and the x axis and α as the angle of attack, disregarded in this study due to the symmetrical fin.

$$\theta(t) = \theta_{\max} \sin(2\pi f t) \tag{D.1}$$

This is consequently derived to get the velocity arriving at Equation D.2.

$$v(t) = \dot{\theta}(t) = 2\pi f \theta_{\max} \cos(2\pi f t) \tag{D.2}$$

From the drag and lift coefficients, it is possible to estimate the instant forces acting on the fin.

$$\begin{cases} C_x = \dfrac{2F_x(t)}{\rho \overline{U}^2 cs} & \Leftrightarrow \quad F_x(t) = \dfrac{\rho \overline{U}^2 cs}{2} C_x \\ C_y = \dfrac{2F_y(t)}{\rho \overline{U}^2 cs} & \Leftrightarrow \quad F_y(t) = \dfrac{\rho \overline{U}^2 cs}{2} C_y \end{cases} \tag{D.3}$$

In the equations, D.3, s represents the span of the flapping foil, c representes the cord of the fin, $F_x(t)$ represents the instantaneous drag and $F_y(t)$ represents the instantaneous lift. For this study, in coherence with the study from Sun et al., 2024, a span of 30 cm was used for the calculations. Considering that this study aims to discover the thrust values, an analysis of the drag forces concluded that certain periods of the the movement accounted for positive drag forces, responsible for the unwanted slowing down motion. Therefore, all positive values were turned to 0 (zero), creating the thrust force variable F_T. To determine the average thrust in one or more cycles, Equation D.4 was used.

$$\overline{F_T} = \frac{1}{kT} \left[\int_{(n-k)T}^{nT} F_T(t)\, dt \right] \tag{D.4}$$

For the average power loss in one or more cycles, equation D.5 was used with $v(t)$ from equation D.2. To resolve the integrals in the equations, the trapezium rule was used, considering the 2 millisecond interval between extracted points.

$$\overline{P_L} = \frac{1}{kT} \left[\int_{(n-k)T}^{nT} F_y(t) v(t) dt \right] \tag{D.5}$$

Appendix E - Velocity Profiles

In order to understand the variations in fluid flow between different oscillating patterns, the velocity profiles obtained from the simulations are displayed here. All velocity profiles were subject to the analyses of a moving average, with an order of 255, to achieve an estimate of the expected fluid velocity, however, this appendix displays only the 50 cm fin with a 30º movement amplitude with the average. Other profiles are displayed only with the data directly from the CFD analyses.

50 cm fin with a 30º movement amplitude - with moving average displayed

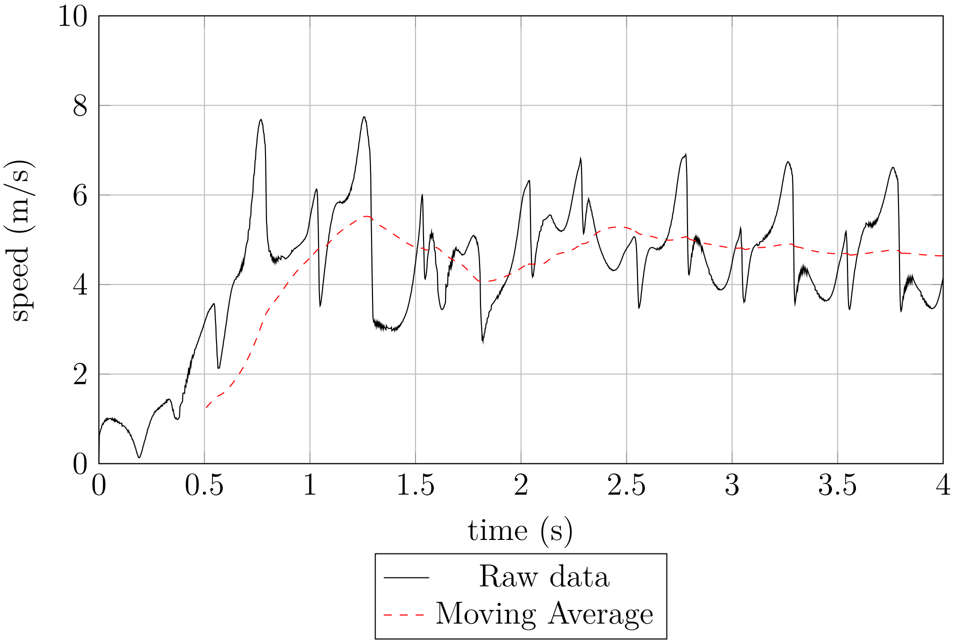

FIGURE E.1: Fluid flow and a moving average with an order of 255, for 30º amplitude at 2 Hz

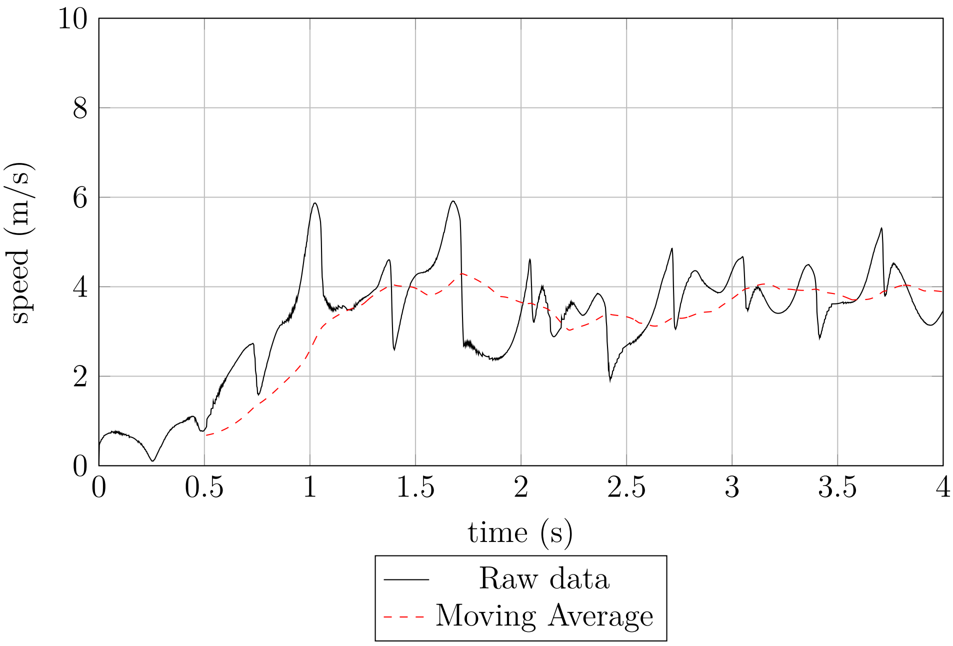

Figure E.2: Fluid flow and a moving average with an order of 255, for 30º amplitude at 1,5 Hz

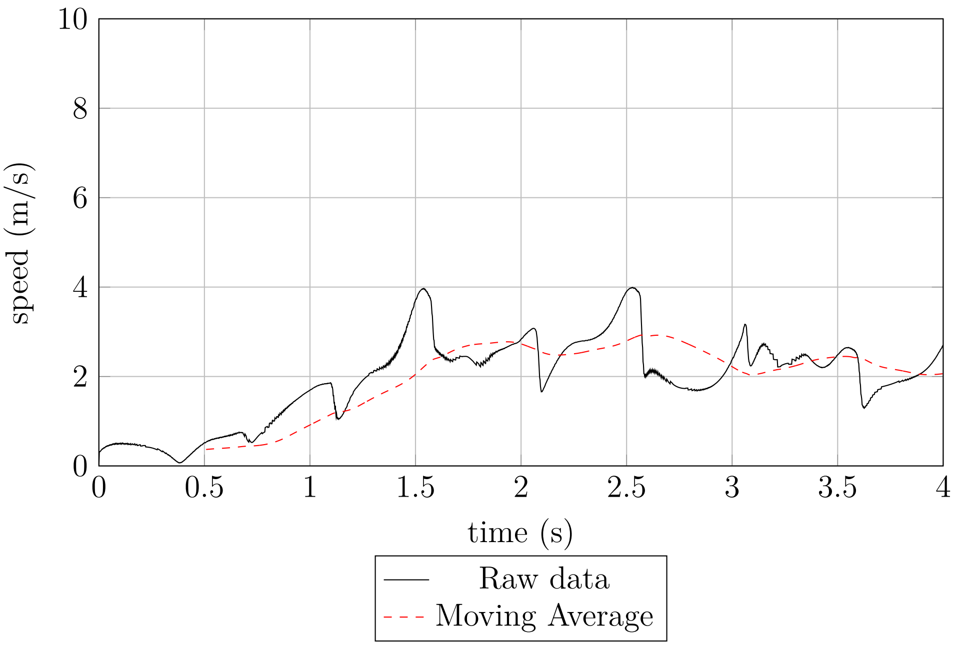

Figure E.3: Fluid flow and a moving average with an order of 255, for 30º amplitude at 1 Hz

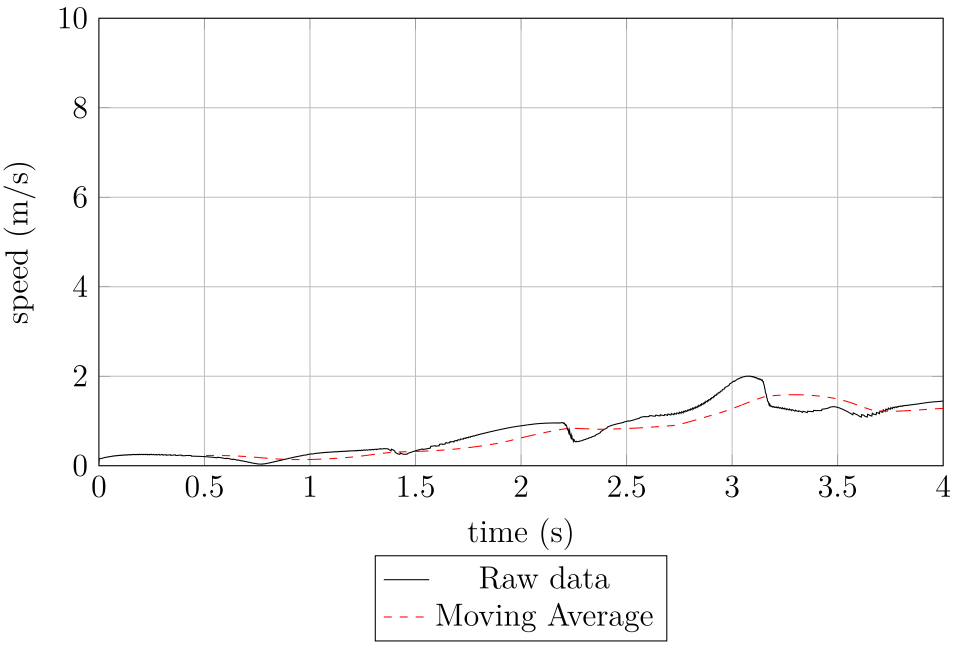

FIGURE E.4: Fluid flow and a moving average with an order of 255, for 30º amplitude at 0,5 Hz

50 cm fin with a 22,5º movement amplitude - without moving average displayed

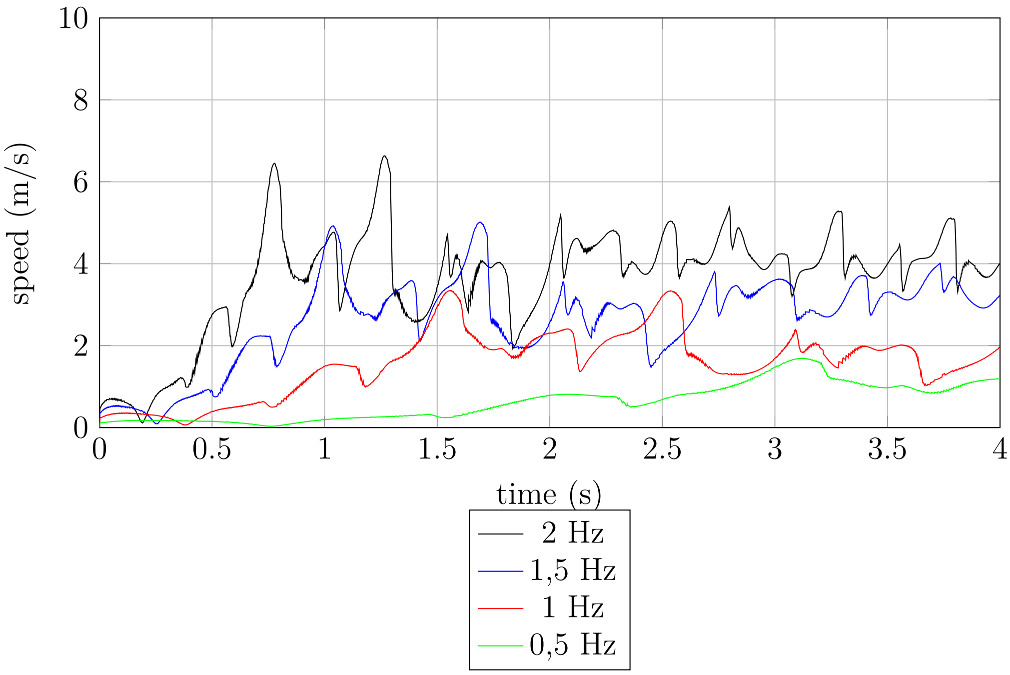

FIGURE E.5: Fluid flow velocity with 50 cm fin and 22,5º amplitude

50 cm fin with a 15º movement amplitude - without moving average displayed

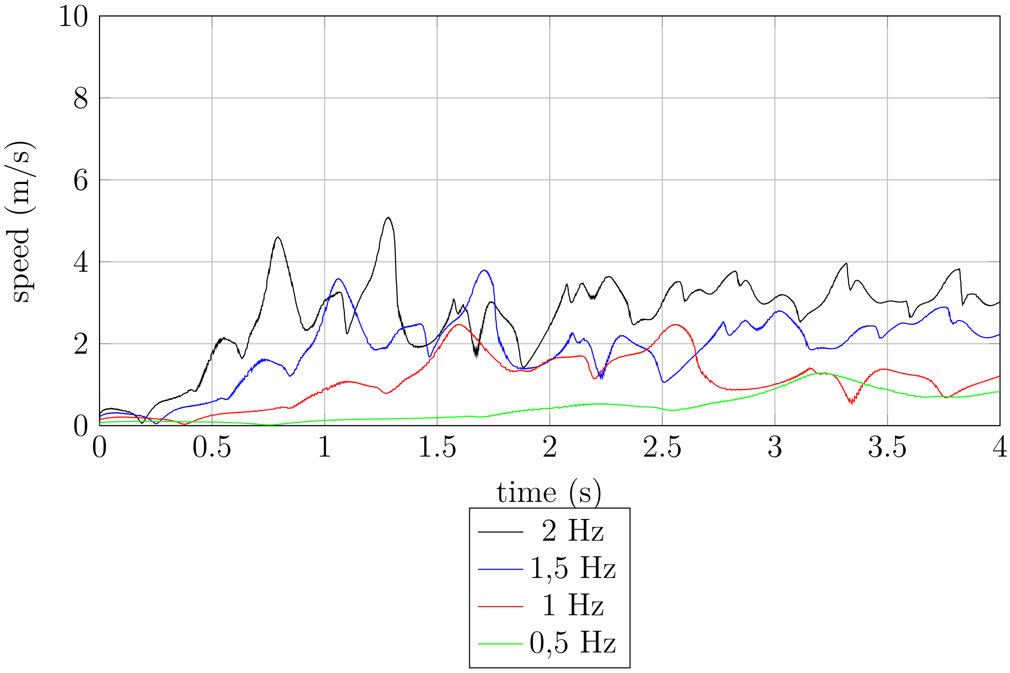

Figure E.6: Fluid flow velocity with 50 cm fin and 15º amplitude

40 cm fin with a 30º movement amplitude - without moving average displayed

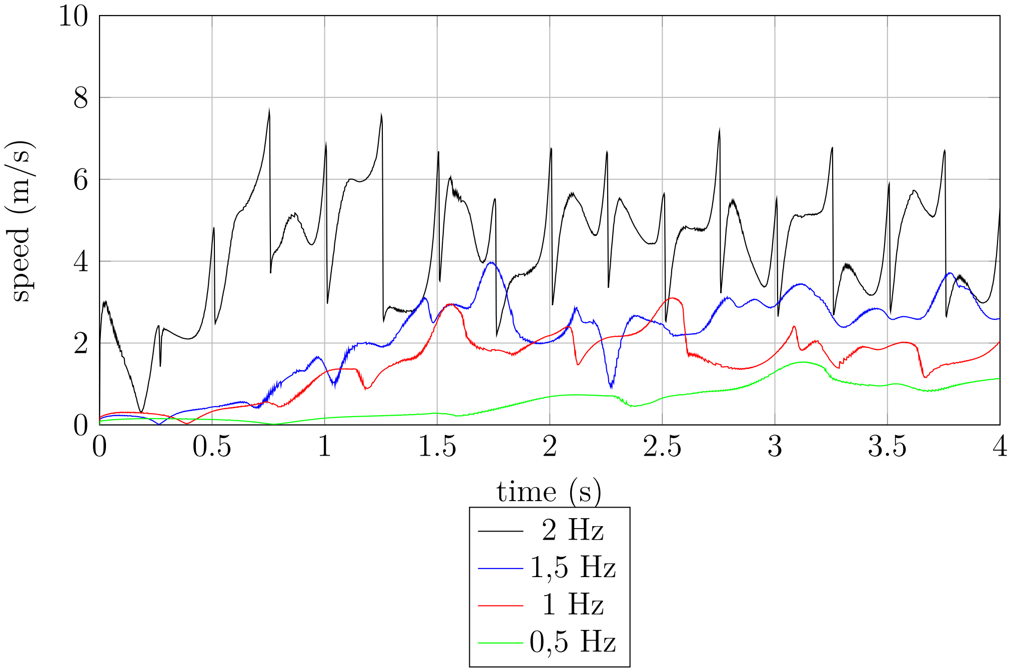

Figure E.7: Fluid flow velocity with 40 cm fin and 30º amplitude

40 cm fin with a 22,5º movement amplitude - without moving average displayed

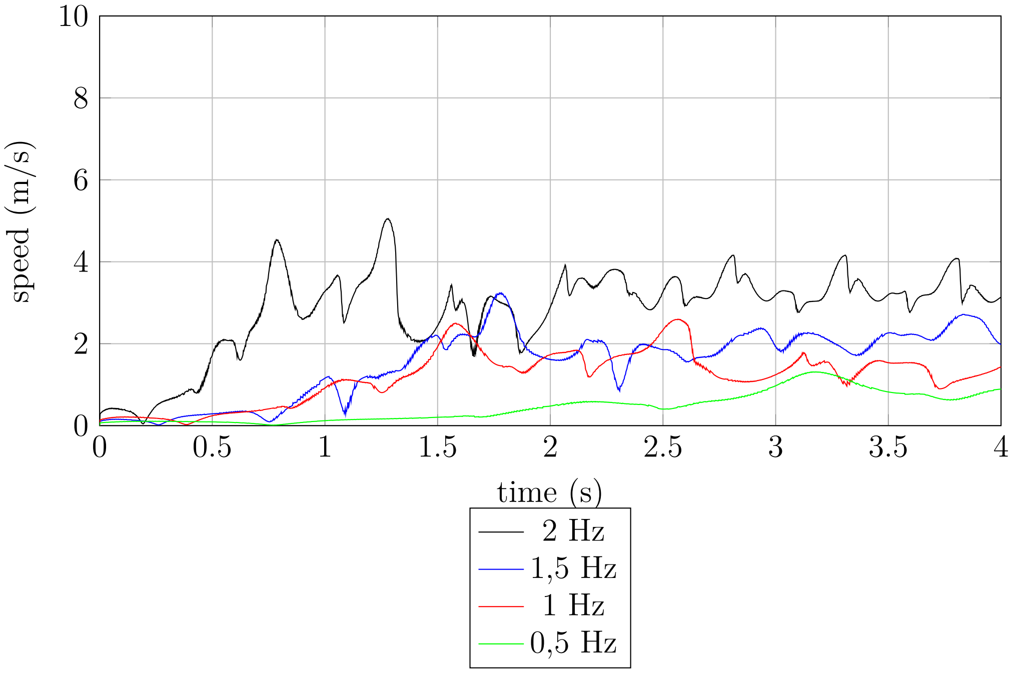

FIGURE E.8: Fluid flow velocity with 40 cm fin and 22,5º amplitude

40 cm fin with a 15º movement amplitude - without moving average displayed

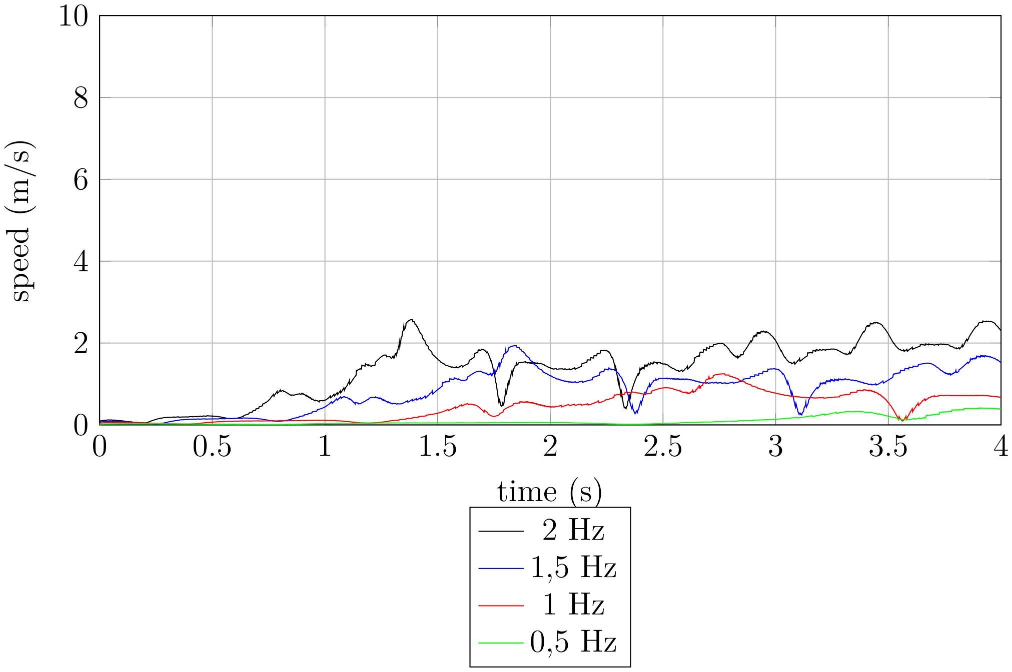

FIGURE E.9: Fluid flow velocity with 40 cm fin and 15º amplitude

ATM - 50 cm and 40 cm fin - without moving average displayed

The following graph displays the different fluid velocity for the ATM movement, for a 30º amplitude and 2Hz frequency.

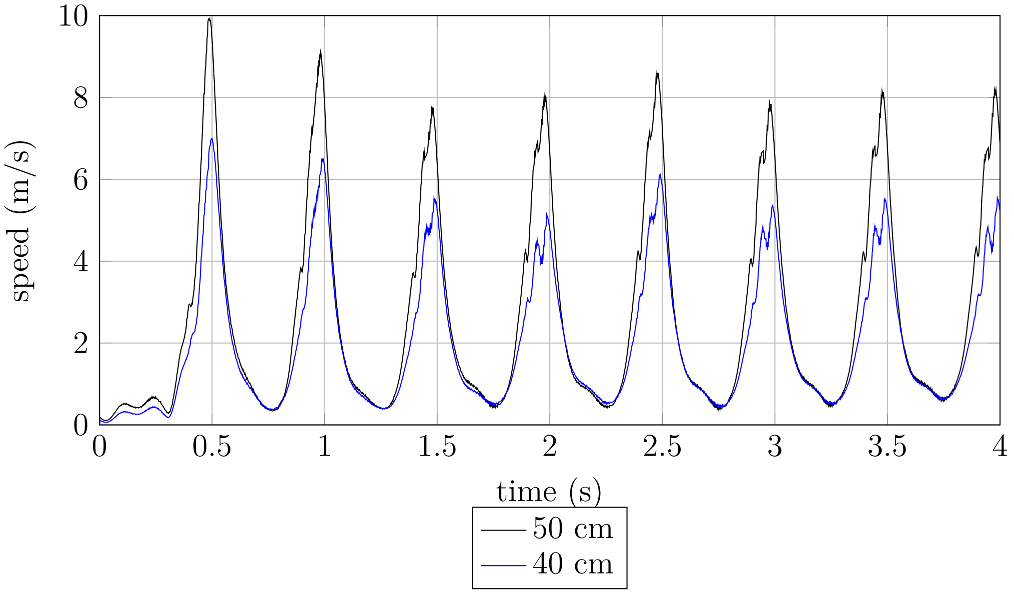

FIGURE E.10: Fluid flow velocity with 50 cm and 40 cm fin with 30º amplitude and 2Hz

Annex I - Spacial Discretization

Spatial discretization is a critical step in the numerical solution of partial differential equations (PDEs), where continuous spatial derivatives are approximated using algebraic expressions on a computational mesh. This process enables the transformation of governing equations, such as the Navier–Stokes equations, into a discrete form suitable for numerical integration.

Let $u(x)$ be a smooth function. A first-order accurate forward difference approximation of the first derivative at a grid point x_i is expressed as:

$$\left.\frac{du}{dx}\right|_{x_i} \approx \frac{u(x_{i+1}) - u(x_i)}{\Delta x} + \mathcal{O}(\Delta x) \tag{I.1}$$

This introduces a truncation error of order $\mathcal{O}(\Delta x)$, implying linear convergence under mesh refinement. Although first-order schemes are more robust and stable, they introduce significant numerical diffusion, which can smear sharp gradients and flow features.

In contrast, a second-order central difference scheme is given by:

$$\left.\frac{du}{dx}\right|_{x_i} \approx \frac{u(x_{i+1}) - u(x_{i-1})}{2\Delta x} + \mathcal{O}(\Delta x^2) \tag{I.2}$$

This approach yields a truncation error of $\mathcal{O}(\Delta x^2)$, providing enhanced accuracy, particularly for smoothly varying fields. Second-order schemes are commonly employed in CFD to reduce numerical dissipation and to resolve flow structures more accurately.

Annex II - Mesh Independence Study

In the context of the study pertaining to the NACA 0012 airfoil, a symmetric profile that is frequently employed in aerodynamic studies, simulations were conducted utilising meshes that ranged from coarse to fine. It was observed that beyond a certain mesh density, the lift and drag coefficients stabilised, indicating mesh independence (Prabu et al., 2024). The present study was dedicated to the use of the NACA 0012 as a fin, and therefore with an undergoing flapping motion. With regard to the integration of components, the study established that a total of 664,807 elements were adequate to attain convergence, as seen in II.1.

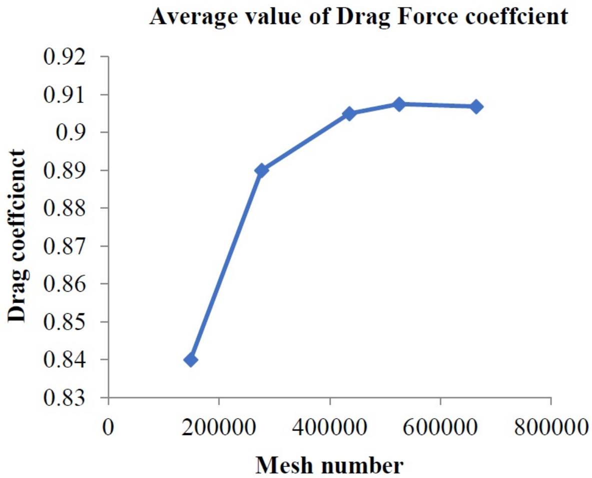

FIGURE II.1: Mesh Independence Study - Drag Force (Prabu et al., 2024)